

# MODELS OF LOW MASS STARS AS PHYSICAL LABRATORIES

A Thesis  
Submitted to the Faculty  
in partial fulfillment of the requirements for the  
degree of

Doctor of Philosophy

in  
Physics and Astronomy  
by Emily M. Boudreaux

Guarini School of Graduate and Advances Studies  
Dartmouth College  
Hanover, New Hampshire

April 24th 2024

Examining Committee:

---

(chair) ***Brian C. Chaboyer***

---

***Elisabeth R. Newton***

---

***Aaron Dotter***

---

***Jamie Tayar***

---

F. Jon Kull, Ph.D.  
Dean of the Guarini School of Graduate and Advanced Studies

### **Copyright Notice**

This work is licensed under the Creative Commons  
Attribution-NonCommercial-ShareAlike 4.0 International License.

To view a copy of this license, visit

<http://creativecommons.org/licenses/by-nc-sa/4.0/>

or send a letter to

Creative Commons, PO Box 1866, Mountain View, CA 94042, USA.

*For Poppy, who taught me to build and supported as I did.*

## Abstract

Low mass stars account for approximately 70 percent of the stellar populations; yet, due to their small sizes and cool temperatures they account for only **NUMBER** percent of the galaxies luminosity function. Consequently, across multiple domains there has been a dearth of interest in these key astronomical objects. In this thesis I present two projects which have further revealed properties of low mass stars. Firstly, I present chemically self consistent models of the globular clusters NGC 2808 and NGC 6752. Due to the ages of both clusters, these models are dominated by low mass stars. We find that chemical consistency between a stars structural and atmospheric models makes only a trivial difference in model predictions. Secondly, I present a detailed investigation into the Gaia M Dwarf Gap (the Jao Gap) looking at how the Jao Gap's theoretical location is effected by high temperature radiative opacity source and how the physics which drives the Jao Gap's formation may also drive perturbations to stellar magnetic field strength.

## Preface

When I was in pre-school I told my father that I would be a professor of astronomy. I remember the day, walking out of the Boyd school, having just looked through a large picture book of the — then — nine planets in our solar system. At the time I did not have a concept of what it meant to be an astronomer. I did not understand what it meant to study space in any way other than looking at images in a large cardboard book. In a very real way that day was the most important in my life and it undoubtedly set a trajectory for me which I have obsessively held onto for the past 22 years. I have held onto that goal; however, my ability to, in some small part with this thesis, achieve the goal that that 4 year old told their father has not primarily been a function of my ability. Rather, many many people in my life have supported me, helped me, loved me, let me lean on them, and been there for me when I need them. I would not have been able to write this thesis without each and every one of them and I am immeasurably grateful for the people in my life.

First of all I would like to speak to my mother and father, Karol and Don. You are the most wonderful parents I could ever imagine. From the time when your young child made the wild statement that they wanted to be an astronomer, through many detentions and late nights at Westminster, through far too many hours at Encore and comically long commutes in high school you have both been the most supportive parents anyone ever could be. You have relentlessly supported and loved me in ways that, I hope, have made me a better person, a better researcher, and a better child. I love you so much and I am so grateful. Thank you.

Secondly, I would like to thank the educators, teachers, and professors who I have interacted with in my life. I have been blessed and privileged to have such a consistently good set of educational role models in my life. From Mr. David Majewski in seventh and eighth grade science, to Ms. Leslie Zeigler in high school biology. My childhood teachers shaped my love of science and helped me develop that goal that four year old me had into a firm sense of what astronomy is. I want to thank Ms. Zeigler in particular for helping me grow my love of science and supporting that during

a time in life when so many people get disillusioned with it. I truly believe that if not for her I would not have remained interested in astronomy through high-school.

When I left high school for college I was worried that I would not be able to build the same kind of relationships with educators there than I had had until that point. I could not have been more wrong. I first met Dr. Brad Barlow the day before his wedding, in October 2014, and from the moment we met he went above and beyond any possible expectation to try to help me become an astronomer. Brad brought me observing at SOAR when I was still a senior in High School, he took me to AAS my first year in college, he co authored 3 papers with me and took me around the world to various conferences. The friendship I developed with Brad was the most important, by far, of my time in college and I immensely grateful for that. More than the professional development opportunities which Brad provided to me I want to thank him for his consistent willingness to engage with me on random thoughts I had. I think chatting outside the Slane center over lunch about various research ideas or topics I had just learned about in class is what began, in earnest, to develop my ability to think about science analytically and critically. That is the greatest gift that a professor could ever give to their student. Thank you Brad.

Outside of education I have also been exceptionally privileged in the friends whom I have met. I spent much of my childhood quite isolated, by choice. However, working at Encore with Sarah, Annika, Kara, and Paddy was one of the most important experiences of my life. Whereas Leslie and Brad helped shape who I am as a scientist, my friends served to shape who I am as a person. There can never be words strong enough to thank you all for that. I love you all very deeply.

Much as I was worried about my ability to form mentor-mentee connections in college I was worried about my ability to make friends in grad school. This concern could not have been more misplaced. I think there is likely no one in grad school with a better set of friends and colleagues. My joint cohort mates and house mates Aylin and Weishi are wonderful. We have lived together for 5 years now and I cannot imagine better people to live with. They are funny, fun, engaging, and wonderful. I am so glad we will be able to keep living together and I am so glad that we have.

Aside from those I live with Steph and Rayna have been incredible friends. Steph is always there for support or laughs, or cooking and Rayna is always there for a good laugh or a sandwich. Thank you all so much for being such wonderful friends and I cannot wait to see what you accomplish with your careers.

Keighley Rockcliffe is one of the most amazing people I have ever met. I remember being so scared of her when I first starting attending group meetings my first year. She is a brilliant scientist, an incredibly empathetic and kind person, and one of my best friends in the world. I could not have finished grad school without her and I want to thank her from the bottom of my heart for always being there for me. During grad school I went through a lot of change in my life, I transitioned, I adopted a dog, I lost a dog, I struggled with depression, and I struggled with anxiety. For every single struggle Keighley has been there to provide a shoulder to cry on, a ear to listen, and an arm to support. Thank you Keighley, you are a wonderful person, I love you so much and I cannot wait to see the impact you make on the world.

Towards the end of my time in graduate school I was lucky enough to meet another one of the most amazing people. I met Isabel in August of 2023 and even though we have only known each other for 8 months, they have been some of the most wonderful 8 months of my life. You have made the stress of the end of grad school so much more bearable and you have made the stress of transitioning so much more bearable. Shortly after we met I lost Jordy unexpectedly and suddenly. That was likely the hardest day of my life and Isabel was there for me in a way that is so much more than could ever have been expected. I could not have continued in grad school after that without Isabel. I love you Isabel and I am so excited for the coming years together.

I adopted Jordy in February of 2021 and she was the best Beagle, the best dog, and the best companion someone could hope for. Jordy was the littlest beagle and the stinkiest girl. She brought so much love and happiness to everyone life. I had planned to walk at graduation with her but unfortunately in October of 2023 Jordy passed away from cancer. I miss you Jordy and I love you little girl.

Finally, this work was conducted under the supervision of Brian Chaboyer and I would not have been able to complete this thesis without his continued support. I

would like to thank Brian immensely for his continued support and for being a wonderful teacher. I have not always been the fastest worker, spending far too long getting distracted with small side projects. However, Brian has always been both supportive and provided a guiding hand to get those projects back on track and turned into publishable material. Thank you Brian.



# Contents

<b>Preliminaries</b>	<b>1</b>
A. Abstract . . . . .	i
B. Preface . . . . .	ii
C. Table Of Contents . . . . .	vii
E. List of Tables . . . . .	xi
F. List of Figures . . . . .	xiii
<b>I Introduction</b>	<b>1</b>
<b>1 A Breif History of Humans &amp; Stars</b>	<b>3</b>
1.1 A post prelude prelude . . . . .	3
1.2 Pre-Modern Astronomy . . . . .	4
1.2.1 Stars In Ancient Times . . . . .	4
1.2.2 Astronomy Becomes a Science . . . . .	4
1.2.3 The Birth of Modern Astronomy . . . . .	5
1.3 Stars in the Modern World . . . . .	5
<b>2 Stellar Structure Evolution</b>	<b>9</b>
<b>3 Stars as Stellar Laboratories</b>	<b>11</b>
<b>II Stellar Populations as Laboratories</b>	<b>13</b>
<b>4 Why Study Globular Clusters</b>	<b>15</b>

<b>5 Modeling Globular Clusters</b>	<b>19</b>
5.1 Problems Modeling Globular Clusters . . . . .	20
<b>6 Multiple Populations in NGC 2808</b>	<b>21</b>
6.1 Introduction . . . . .	21
6.2 Stellar Models . . . . .	21
6.3 Chemical Consistency . . . . .	22
6.3.1 Atmospheric Boundary Conditions . . . . .	24
6.3.2 Opacities . . . . .	25
6.4 fidanka . . . . .	25
6.4.1 Fiducial Line Measurement . . . . .	26
6.4.2 Stellar Population Synthesis . . . . .	31
6.4.3 Isochrone Optimization . . . . .	32
6.4.4 Fidanka Testing . . . . .	32
6.5 Isochrone Fitting . . . . .	33
6.5.1 The Number of Populartions in NGC 2808 . . . . .	35
6.5.2 ACS-HUGS Photometric Zero Point Offset . . . . .	36
6.6 Results . . . . .	37
6.6.1 The Number of Populartions in NGC 2808 . . . . .	39
6.7 Conclusion . . . . .	39
<b>7 Modeling NGC 6752</b>	<b>41</b>
<b>8 Gap Sensitivity to Opacity Source</b>	<b>43</b>
8.1 INTRODUCTION . . . . .	43
8.2 Jao Gap . . . . .	45
8.2.1 Efforts to Model the Gap . . . . .	47
8.3 Updated Opacities . . . . .	48
8.3.1 Table Querying and Conversion . . . . .	49
8.3.2 Solar Calibrated Stellar Models . . . . .	51
8.4 pyTOPSScrape . . . . .	53
8.5 Interpolating $\rho \rightarrow R$ . . . . .	53

<b>CONTENTS</b>	<b>ix</b>
8.6 Modeling . . . . .	55
8.6.1 Population Synthesis . . . . .	56
8.6.2 Mixing Length Dependence . . . . .	60
8.7 Results . . . . .	62
<b>9 Jao Gap connection to Magnetism</b>	<b>69</b>
9.1 INTRODUCTION . . . . .	69
9.2 Correlation . . . . .	71
9.2.1 Conicidence with the Jao Gap Magnitude . . . . .	76
9.2.2 Rotation . . . . .	77
9.2.3 Limitations . . . . .	84
9.3 Modeling . . . . .	87
9.3.1 Limitations . . . . .	90
9.4 Conclusion . . . . .	92
<b>III Individual Stars as Laboratories</b>	<b>93</b>
<b>10 Magnetic Fields In M Dwarfs</b>	<b>95</b>
10.1 Magnetic Activity in M dwarfs . . . . .	95
10.2 Observations & Data Reduction . . . . .	98
10.3 Analysis . . . . .	99
10.3.1 Rotation and Rossby Number . . . . .	102
10.4 Rotation–Activity Relation . . . . .	103
10.5 Magnetic Activities in M dwarfs Closing Thoughts . . . . .	109
<b>11 The Red Giant Branch Bump</b>	<b>111</b>
11.1 The Red Giant Branch Bunch in NGC 2808 . . . . .	112
11.1.1 Population E and the Case of the Missing Bump . . . . .	113
11.2 Effects of Opacities on the Red Giant Branch Bump . . . . .	114
11.3 Going forward . . . . .	114



# List of Tables

6.1	Relative Metal composition used where $a(H) = 12$ . Where the relative composition is the same for both populations A and E it is only listed in the population A column for the sake of visual clarity. . . . .	23
6.2	Best fit parameters derived from fitting isochrones to the fiducial lines derived from the NCG 2808 photometry. . . . .	35
6.3	Best fit parameters derived from fitting isochrones to the fiducial lines derived from the NCG 2808 photometry. . . . .	38
8.1	Optimized parameters for SCSMs evolved using OPAL and OPLIB high temperature opacity tables. . . . .	53
8.2	Locations identified as potential Gaps. . . . .	63
9.1	All data used from P2021 and B2022. . . . .	79
10.1	Calculated Rossby Numbers and $R'_{HK}$ values. All circular data points in Figures 10.2 & 10.3 are present in this table. Masses are taken from the MEarth database. A machine readable version of this table is <b>available</b> . . . . .	110



# List of Figures

6.1	Comparison of the MARCS model atmospheres generated for the two extreme populations of NGC 2808. These lines shows population A and E with the same Helium abundance; though, we fit a grid of models over various helumn abundances. Dashed lines show the temperature of the boundary condition while sold lines show the pressure. . . . .	25
6.2	Density map demo showing density estimate over different parts of the evolutionary sequence. The left panel shows the density map over the entire evolutionary sequence, while the middle panel shows the density map over the main sequence and the right most panel shows the density map over the RGB. Figures in the top row are the raw CMD, while figures in the bottom row are colored by the density map. . . . .	27
6.3	CMD where points are colored by density. Lines show the density-color profile in each magnitude bin. In this figure adaptive binning targeted 1000 stars per bin . . . . .	28
6.4	Example of BGMM fit to a magnitude bin. The grey line shows the underlying color-density profile, while the black dashed-line shows the joint distribution of each BGMM component. The solid black lines show the two selected components. . . . .	29
6.5	CMD where points are colored by density. Line trace the infered fiducial line(s) in each magnitude bin. . . . .	30

6.6 Synthetic population generated by fidanka at 10000pc with E(B-V) = 0, and an age of 12 Gyr along with the best fitting isochrone. The best fit paremeters are derived to be $mu = 15.13$ , E(B-V)=0.001, and an age of 12.33 Gyr. . . . .	33
6.7 Percent Error distribution for each of the three deriver parameters. Note that these values will be sensitive to the magnitude uncertainties of the photometry. Here we made use of the ACS artificial star tests to estimate the uncertainties. <a href="#">Note that currently this is built with 100 runs, these take a long time so currently re running with 1000 runs.</a> . . . . .	34
6.8 Best fit isochrone results for NGC 2808. . . . .	35
6.9 Silhouette analysis for NGC 2808 F275W-F814W photometry. The Silhouette scores are an average of score for each magnitude bin. Positive scores incidate that the clustering algorithm produced well distinguished clusters while negative scores indicate clusters which are not well distinguished. . . . .	36
6.10 (left) CMD showing the photometric offset between the ACS and HUGS data for NGC 2808. CMDs have been randomly subsampled and colored by point density for clarity. (right) Mean difference between the color of the HUGS and ACS fiducial lines at the same magnitude. Note that the ACS data is systematically bluer than the HUGS data. . . . .	37
6.11 Main sequence turn off magnitude offset from a guage helium mass fraction (Y=0.30 chosen). All main sequence turn off locations are measured at 12.3 Gyr <a href="#">Should I make these contour surfaces for various ages?</a> . . . . .	38
6.12 Best fit isochrone results for NGC 2808. . . . .	39
8.1 The Jao Gap (circled) seen in the Gaia Catalogue of Nearby Stars ( <a href="#">Gaia Collaboration et al., 2021</a> ). . . . .	46

8.2 Diagram for a characteristic stellar model of $0.35625 M_{\odot}$ which is within the Jao Gap’s mass range. The black shaded regions denote whether, at a particular model age, a radial shell within the model is radiative (with white meaning convective). The lines trace the models core temperature, core ${}^3\text{He}$ mass fraction, fractional luminosity wrt. the zero age main sequence and fractional radius wrt. the zero age main sequence. . . . .	47
8.3 Rosseland mean opacity with the GS98 solar composition for both OPAL opacities and OPLIB opacities (top). Residuals between OPLIB opacities and OPAL opacities (bottom). These opacities are plotted at $\log_{10}(R) = -0.5$ , $X = 0.7$ , and $Z = 0.02$ . $\log_{10}(R) = -0.5$ approximates much of the interior a $0.35 M_{\odot}$ model. Note how the OPLIB opacities are systematically lower than the OPAL opacities for temperatures above $10^{5.2}$ K. . . . .	50
8.4 HR Diagram for the two SCSMs, OPAL and OPLIB. OPLIB is shown as a red dashed line. . . . .	52
8.5 Log Fractional Difference between opacities in $\kappa_R(\rho, T_{\text{eff}})$ space directly queried from the OPLIB web-form and those which have been interpolated into $\log(R)$ space and back. Note that, due to the temperature grid of type 1 OPAL tables not aligning perfectly with the temperature grid OPLIB uses there may be edge effects where the interpolation is poorly constrained. The red line corresponds to $\log(R) = -0.79$ where much of a stellar model’s radius exists. . . . .	55
8.6 Mass-luminosity relation at 7 Gyrs for models evolved using OPAL opacity tables (top) and those evolved using OPLIB opacity tables (bottom). Note the lower mass range of the OPLIB Gap. . . . .	57
8.7 Probability distribution sampled when assigning true parallaxes to synthetic stars. This distribution is built from the GCNS and includes all stars with BP-RP colors between 2.3 and 2.9, the same color range of the Jao Gap. . . . .	59

8.8	Population synthesis results for models evolved with OPAL (left) and models evolved with OPLIB (right). A Gaussian kernel-density estimate has been overlaid to better highlight the density variations. . . . .	60
8.9	CMD showing OPLIB populations (from left to right) A, B, and C. . . . .	61
8.10	Location of the two identified paucities of stars in OPLIB synthetic populations as a function of the mixing length used. . . . . . . . . . .	62
8.11	(right panels) OPAL (left) and OPLIB (right) synthetic populations. (left panels) Normalized linear number density along the magnitude axis. A dashed line has been extended from the peak through both panels to make clear where the identified Jao Gap location is wrt. to the population. . . . . . . . . . .	66
8.12	Portions of $0.3526 M_{\odot}$ OPAL and OPLIB stellar models showing the interior shells which are radiative (black region). Note that for clarity only one convective mixing event from each model is shown. Note how the radiative zone in the OPLIB model is larger. . . . . . . . . . .	67
8.13	Core $^3\text{He}$ mass fraction for $0.3526 M_{\odot}$ models evolved with OPAL and OPLIB (within the Jao Gap's mass range for both). Note how the OPLIB model's core $^3\text{He}$ mass fraction grows at approximately the same rate as the OPAL model's but continues uninterrupted for longer. . . . . . . . . . .	68
9.1	Merged Dataset from Perdelwitz et al. (2021); Boudreux et al. (2022). Note the increase in the spread of $R'_{HK}$ around the Jao Gap Magnitude (top). Standard deviation of Calcium emission data within each bin. Note the discontinuity near the Jao Gap Magnitude (bottom). The location of the Gap as identified in literature is shown by the hatched region ( $\sim 10\text{-}10.5 M_G$ ). Potential explanations for the disagreement in magnitude are discussed in detail in Section 9.2.1. . . . . . . . . . .	73
9.2	Probability distribution of the false alarm probability for the discontinuity seen in Figure 9.1. The mean of this distribution is $0.341\% \pm^{0.08}_{0.08}$ . . . . . . . . . . .	74

9.3 Spread in the magnetic activity metric for the merged sample with any stars $\log(R'_{HK}) > -4.436$ filtered out. <b>The location of the Gap as identified in literature is shown by the hatched region (<math>\sim 10\text{-}10.5 M_G</math>)</b> . . . . .	75
9.4 Probability density distribution of discontinuity location as identified in the merged dataset. The dashed line represents the mean of the distribution while the shaded region runs from the 16th percentile to the 84th percentile of the distribution. This distribution was built from 10,000 independent samples where the discontinuity was identified as the highest value in the gradient of the standard deviation. <b>The location of the Gap as identified in literature is shown by the hatched region (<math>\sim 10\text{-}10.5 M_G</math>)</b> . . . . .	77
9.5 Rotational Periods against G magnitude for all stars with rotational periods (top). Standard deviation of rotational period within magnitude bin (bottom). <b>The location of the Gap as identified in literature is shown by the hatched region (<math>\sim 10\text{-}10.5 M_G</math>)</b> . . . . .	85
9.6 Rossby number vs. G magnitude for all stars with rotational periods and V-K colors on Simbad. Dashed lines represent the hypothesized region of decreased rotation. <b>The location of the Gap as identified in literature is shown by the hatched region (<math>\sim 10\text{-}10.5 M_G</math>)</b> . . . . .	86
9.7 Kippenhan-Iben diagram for a 0.345 solar mass star. Note the periodic mixing events (where the plotted curves peak). . . . .	89
9.8 Example of the toy model presented here resulting in increased divergence between stars magnetic fields. The shaded region represents the maximum spread in the two point correlation function at each age. . . . .	90
9.9 Toy model results showing a qualitatively similar discontinuity in the star-to-star magnetic activity variability. . . . .	91

10.1 Spectrum of 2MASS J06105288-4324178 overplotted with the S index bandpasses. (top) V band and Ca II K emission line. (bottom) Ca II H emission line and R band. Note that the rectangular and triangular regions denote both the wavelength range of the band and the relative weight assigned to each wavelength in the band while integrating. . . . .	100
10.2 Rotation activity relation from this work. The color axis gives each stars mass. The dashed line is the best fit to our data set. . . . .	104
10.3 Rotation activity relation for both our work and <a href="#">Astudillo-Defru et al. (2017)</a> . The dotted line is the best fit to the re-derived rotation-activity relation from <a href="#">Astudillo-Defru et al. (2017)</a> . Note that targets from <a href="#">Astudillo-Defru et al. (2017)</a> are systematically higher than targets presented here as a consequence of the range in mass probed by the samples. . . . .	105
10.4 Derived rotation-activity curves from this work, <a href="#">Astudillo-Defru et al. (2017)</a> and <a href="#">Mamajek &amp; Hillenbrand (2008)</a> . Note both that <a href="#">Mamajek &amp; Hillenbrand (2008)</a> focuses their work on earlier spectral classes and fits the rotation activity relation in linear space. . . . .	105
10.5 Distribution of masses between our sample and the sample presented in <a href="#">Astudillo-Defru et al. (2017)</a> . Note how the two studies have approximately the same sample sizes; however, our sample is more tightly concentrated at lower masses \later spectral classes. . . . .	109
11.1 Luminosity function for a population A and E model. Note how there is a bump at approximatly $M_V = 16.5$ for population A but not for E. The dashed line represents the literature value for the observed RGBB in NGC 2808. . . . .	113
11.2 Fractional mass of the convective envelope of a popualation A and E model vs. model age. Note how the population A model's convective envelope reaches approximatly 60 percent of the star by mass while the population E convective envelope only reaches 40 percent of the star by mass. . . . .	114

## **Part I**

# **Introduction**



# Chapter 1

## A Breif History of Humans & Stars

*That's the wonderful thing about crayons. They can take you to more places than a starship.*

– Guinan, Star Trek the Next Generation, Season 6, Episode 7.

### 1.1 A post prelude prelude

I will start by saying that I am not trained in history and perhaps it is self-indulgent to begin with such an amateur overview of another academic field. However, all of the abstraction which we surround ourselves with in so many of the physical sciences may sometimes sever us from underlying motivations as to why we are interested. It is true that we often speak to the public and to funding agencies about grand ambition and infinite possibility; however, our day-to-day lives are not defined by these things. We spend so much of our time either immersed in the fine details or postulating about greater purpose that I find that I often feel disconnected from the real reason I am interested in astronomy. I study astronomy because I am interested in space, there is no greater reason, nothing more substantial than a five year old sitting with their father outside their preschool asking about why the stars and moon are the way that they are. With that being said, please bear with me as I walk us through a brief history of some of the places stars have had in human civilization and the evolution of our understanding of them.

## 1.2 Pre-Modern Astronomy

### 1.2.1 Stars In Ancient Times

The ansestors of humans have no doubt been looking at the sky since before they were humans; however, there are limited ways to study these prehistoric astronomers. Some reminatnts of ealy human (pre-history,  $\gtrapprox$  5000 yrs ago) stargazing to remain, largely in the form of earthn works [CITATION HERE]. The earliest records we have show stars playing an imporant role in religius practices, navigation, and time keeping [CITATION HERE]. These early understandings recognized differences between the fixed stars and the wandering stars though it would be many more centuries and millenia before the full extent of those differences became clear [CITATION HERE].

As far back as the 1300s B.C.E there were accurate star charts being produced by ancient Egyptian, Babylonian, and Chinese astronomers. Fourth century B.C.E Greeks develope star catalougs and many of the moden day English names of stars still derive from these early catalougs.

The understanding of fixed stars at this time was not one of objects similar to our sun; rather, they were thought to be seperate things altogether. Various cosmologies supposed that stars were points on a celestial sphere which surrounded the earth, such as the Babylonian cosmology with posited that the stars existed in a heaven of their own which was interlocked with 2 other heavens.

### 1.2.2 Astronomy Becomes a Science

The ancient Greeks, Babylonians, and Chinese contributed greatly to our understanding of the universe; however, it was later work, largely by Islamic and Indian scholars which form the basis of what we think of as modern astronomy. These astronomers were not yet conceptualizing the universe the way that we model it today; however, they began systamatzized observations of the universe in ways which would be recognizable. One of the main driving forces of astronomy during this period was nagivation and to that end new instrumentation was developed and early observato-ries were built. In 934 C.E. *The Book of Fixed Stars* was written by Abd al-Rahman

al-Sufi. A expansion of the kinds of catalougs which began over a millenia earlier and allowed for more precise navigation of ships.

By the 10th Century C.E. Islamic scholars had found evidence that the Earth was not, contrary to Ptolomeic ideas, stationary. In the following centuries multiple critisicms of Ptolemeic theories were published, though none going quite as far as doubting the geocentric model of the universe. One primary change to these ancient theories was the regognition that the Earth rotates about its axis as opposed to the heavens rotaing around earth [CITATION HERE].

### 1.2.3 The Birth of Modern Astronomy

Modern Astronomy does not have a single birth, and different cultures at different points in time have contributed in various ways to our modern understanding. Often, in western culture we think of 15th and 16th century astronomers, such as Johannas Kepler and Tycho Brahe as the first astronomers. No doubt that Brahe infulence pushed the field to systamatize certain observations more and Kepler's theoretical work was some of the earliest which presented a reasonable model of orbital motion. However, outside of Europe astronomers such as Uluga Beg (1394 → 1449) and Wang Zhenyi (1768 → 1797) we building early observatories, improving star catalougs, and devloping models for both lunar and solar eclipses.

Despite Astronomy's extrenley long history peoples perceptions of what stars were had remained relativly fixed over time. There had been some early astronomers (notably from Aristotle) who proposed that stars might be far away suns; however, this did not translate to mainstream of global acceptance. This began to change during the early modern period and it became more common to view stars as far away stars potentially with their own planetary systems. Even during this period though, what a star is, what the sun is, physically, was not understood.

## 1.3 Stars in the Modern World

With the advent of spectroscopy and more formalized and globalized astronomy during the 18th and 19th centuries a physically driven picture of stars emerged. Spec-

troscopy revealed similar trends between our sun and other stars and new physics and chemistry allowed astronomers to start pieceing together that stars were made, primarily, of extremley hot hydrogen and helium [CITATION HERE].

By the early 20th century astronomers were close to figuring out what energy powered stars. The most prominant theory being heat generated from gravitational collapse (which had innitally been propsed as a theory of star formation, but not energy generation by Kant and Laplace [CITATION HERE]). Lord Kelvin and Hermann von Helmholtz proposed that a stars energy could originate from gravitational collapse. They derived that the sun could power itself for 19 million years [CITATION HERE](Aside 1). However, as geological records settled on an age in the billions of years for earth it became clear that some other mechanism must provide energy to a star.

Arthur Eddington, often considered one of the founders of stellar astrophysics, concerned with discrepancy between geological records of Earths age an the suns maximum life span, as predicted by the Kelvin-Helmholtz mechanism, proposed in the 1920s that a stars energy might primarily originate from the fusion of hydrogen into helium [CITATION HERE]. Early estimates of the maxium lifespan of the sun if it were powered by hydrogen fusion prooved to be sufficient for the Earths lifespan to make sense. In the following decades the sun and other stars

#### Aside 1: Kelvin-Helmholtz Lifespan

The total binding energy of a star may be approximated as

$$U = -\frac{3}{5} \frac{GM^2}{R} \approx -2.3 \times 10^{41} \text{J}$$

From the flux of the sun and its radius we can find that its approximate energy output is  $4 \times 10^{26}$  Watts. Then assuming all of that energy is being produced by gravaitational collapse the total time the sun could burn would be given by the ratio of the total energy to the luminosity.

$$t = \frac{|U|}{L} \approx 19 \times 10^6 \text{yr}$$

would become important test beds for physics too extreme to be studied in laboratory conditions on earth, a theme similar to one we will return to multiple times during this thesis.

While the mechanism which powers the sun was still being debated mathematical models which would evolve into those still used today were being developed. Over the last half of the 19th and first decade of the 20th centuries Lane, Ritter, and Emden codified the earliest mathematical model of stellar structure, the polytrope (Equation 1.1), in *Gaskugeln* (Gas Balls) ([Emden, 1907](#)).

$$\frac{d}{d\xi} \left( \xi^2 \frac{d\theta}{d\xi} \right) = -\xi^2 \theta^n \quad (1.1)$$

Where  $\xi$  and  $\theta$  are dimensionless parameterizations of radius and temperature respectively, and  $n$  is known as the polytropic index. Despite this early work, it wasn't until the late 1930s and early 1940s that the full set of equations needed to describe the structure of a steady state, radially-symmetric, star (known as the equations of stellar structure) began to take shape as the specific fusion chains (primarily the proton-proton chains and the Carbon-Nitrogen-Oxygen cycle) were, seriously considered as energy generation mechanisms ([Cowling, 1966](#)). Since then, and especially with the proliferation of computers in astronomy, the equations of stellar structure have proven themselves an incredibly predictive set of models.

Today stars and stellar physics form the basis of much of astronomy [[CITATION HERE](#)]. Despite being some of the smallest objects studied by astronomers stars provide the majority of the luminsosity of the universe [[CITATION HERE](#)]. They make up key rungs on the distance ladder [[CITATION HERE](#)], and they provide key constraints on topics as varied as fundamental nuclear physics [[CITATION HERE](#)] and the search for habital planets and life [[CITATION HERE](#)]. Stars then represent not just an interesting object of study in their own right but also, in the right conditions, laboratories where we can study astronomical objects in a controlled manner.

Astronomy is somewhat of an outlier in the nautral sciences in so far as we do not have access to labratory conditions — at least most of the time, notable exceptions

include experiments such as those run with the Z-machine, computational simulations, and certain cosmochemistry work. Throughout this thesis we will discuss five projects which use low mass,  $< 2 M_{\odot}$ , as laboratories to test various physics in a controlled manner. First we will show how features present in statistical samples of stars may be used to measure population ages

## Chapter 2

# Stellar Structure Evolution

There are currently many stellar structure codes (e.g. [Dotter et al., 2008](#); [Kovetz et al., 2009](#); [Paxton et al., 2011](#)) which integrate the equations of stellar structure — in addition to equations of state and lattices of nuclear reaction rates — over time to track the evolution of an individual star. The Dartmouth Stellar Evolution Program (DSEP) ([Chaboyer et al., 2001](#); [Bjork & Chaboyer, 2006](#); [Dotter et al., 2008](#)) is one such, well tested, stellar evolution program.

DSEP solves the equations of stellar structure using the Henyey method ([Henyey et al., 1964](#)). This is a relaxation technique making use of a Newton–Raphson root finder and therefore requires some initial guess to relax towards a solution. This guess will be either some initial, polytropic, model or the solution from the previous timestep. In order to evolve a model through time DSEP alternates between solving for reaction rates and the structure equations. At some temperature and pressure from the solution to the structure equations DSEP finds the energy generation rate due to proton-proton chains, the CNO cycle, and the triple-alpha process from known nuclear cross sections. These reaction rates yield both photon and neutrino luminosities as well as chemical changes over some small time step. Thermodynamic variables are calculated using an equation of state routine which is dependent on the initial model mass. All the updated physical quantities (pressure, luminosity, mean molecular mass, temperature) are then used to solve the structure equations again. This process of using a solution to the structure equations to calculate reaction rates which then

inform the next structure solution continues until DSEP can no longer find a solution. This can happen as the stellar structure equations are extremely stiff. In addition, for finite radial mesh sizes, discontinuities can occur.

While other stellar evolution programs, such as the widely used Modules for Experimentation in Stellar Astrophysics (MESA) ([Paxton et al., 2011](#)), consider a more complex handling of nuclear reaction rate calculations, and are consequently more applicable to a wider range of spectral classes than DSEP, DSEP has certain advantages over these other programs that make it well suited for certain tasks, such as low-mass modeling. For one, DSEP generally can evolve models much more rapidly than MESA and has a smaller memory footprint while doing it. This execution time difference is largely due to the fact that DSEP makes some simplifying assumptions due to its focus only on models with initial masses between  $0.1$  and  $5$   $M_{\odot}$  compared to MESA's more general approach. Moreover, MESA elects to take a very careful handling of numeric uncertainty, going so far as to guarantee byte-to-byte similarity of the same model run on different architectures ([Paxton et al., 2011](#)). DSEP on the other hand makes no such guarantee. Rather, models evolved using DSEP will be accurate down to some arbitrary, user controllable, tolerance but beyond that point may vary from one computer to another. Despite this trade off in generality and precision, the current grid of isochrones generated by DSEP ([Dotter et al., 2008](#)), has been heavily cited since its initial release in 2008, proving that there is a place for a code as specific as DSEP.

## Chapter 3

# Stars as Stellar Laboratories

- Overview of what makes stars so important to human history
- Overview of what makes stars so important to the history of the universe
- General overview of the history of stellar structure
  - History of thought on stars
  - First attempts to describe what stars were
  - Early modern attempts to describe stars (i.e. gravity collapse)
  - Start of modern stellar astrophysics
  - history of stellar structure equations
  - history of computer models
  - history and provenance of DSEP
- Why is it important to understand stellar physics going forward
- Switch gears to talk about GC because of how they are
  - The role GC play in understanding the universe
  - labs to test stellar physics!
- Talk about Jao Gap
  - Talk about the Jao Gap as a stellar laboratory (interiors of low mass stars)

- Talk about the RGBB, again a lab for stellar physics
- brief overview of what will be presented in the thesis

## **Part II**

# **Stellar Populations as Laboratories**



## Chapter 4

# Why Study Globular Clusters

Globular clusters (GCs) are among the oldest observable objects in the universe (Peng et al., 2011). They are characterized by high densities with typical half-light radii of  $\leq 10$  pc (van den Bergh, 2010), and typical masses ranging from  $10^4$ – $10^5$  M<sub>⊙</sub> (Brodie & Strader, 2006) — though some GCs are significantly larger than these typical values (e.g. ωCen, Richer et al., 1991). GCs provide a unique way to probe stellar evolution (Baumgardt & Makino, 2003), galaxy formation models (Boylan-Kolchin, 2018; Kravtsov & Gnedin, 2005), and dark matter halo structure (Hudson & Robison, 2018).

The traditional view of Globular Clusters was, for a long time, that they consisted of a single stellar population (SSP, in some publications this is referred to as a Simple Stellar Population). This view was supported by spectroscopically uniform heavy element abundances (Carretta et al., 2010; Bastian & Lardo, 2018) accross most clusters (M54 and ωCen are notable exceptions, see Marino et al. (2015) for further details), and the lack of evidence for multiple stellar populations (MPs) in past color-magnitude diagrams of GCs (i.e. Sandage, 1953; Alcaino, 1975). However, over the last 40 years non-trivial star-to-star light-element abundance variations have been observed (i.e. Smith, 1987) and, in the last two decades, it has been definitively shown that most if not all Milky Way GCs have MPs (Gratton et al., 2004, 2012; Piotto et al., 2015). The lack of photometric evidence for MPs can be attributed to the short color throw available to ground based photometric surveys (Milone et al.,

2017); specifically, lacking UV filters. While MPs are chemically distinct from one another, that distinction is most prominent when observing with  $U$  and  $B$  filters (Sbordone et al., 2011).

The prevalence of multiple populations in GCs is so distinct that the proposed definitions for what constitutes a globular cluster now often center the existence of MPs. Whereas, people have often tried to categorized objects as GCs through relations between half-light radius, density, and surface brightness profile, in fact many objects which are generally thought of as GCs don't cleanly fit into these cuts (Peebles & Dicke, 1968; Brown et al., 1991, 1995; Bekki & Chiba, 2002). Consequently, Carretta et al. (2010) proposed a definition of GC based on observed chemical inhomogeneities in their stellar populations. The modern understanding of GCs then is not simply one of a dense cluster of stars which may have chemical inhomogeneities and multiple populations; rather, it is one where those chemical inhomogeneities and multiple populations themselves are the defining element of a GC.

All Milky Way globular clusters older than 2 Gyr studied in detail show populations enriched in He, N, and Na while also being deplete in O and C (Piotto et al., 2015; Bastian & Lardo, 2018). These light element abundance patterns also are not strongly correlated with variations in heavy element abundance, resulting in spectroscopically uniform Fe abundances between populations. Further, high-resolution spectral studies reveal anti-correlations between N-C abundances, Na-O abundances, and potentially Al-Mg (Sneden et al., 1992; Gratton et al., 2012). Typical stellar fusion reactions can deplete core oxygen; however, the observed abundances of Na, Al, and Mg cannot be explained by the likes of the CNO cycle (Prantzos et al., 2007).

Formation channels for these multiple populations remain a point of debate among astronomers. Most proposed formation channels consist of some older, more massive, population of stars polluting the pristine cluster media before a second population forms, now enriched in heavier elements which they themselves could not have generated (for a detailed review see Gratton et al., 2012). The four primary candidates for these polluters are asymptotic giant branch stars (AGBs, Ventura et al., 2001; D'Ercole et al., 2010), fast rotating massive stars (FRMSs, Decressin et al., 2007),

super massive stars (SMSs, Denissenkov & Hartwick, 2014), and massive interacting binaries (MIBs, de Mink et al., 2009; Bastian & Lardo, 2018).

Hot hydrogen burning (proton capture), material transport to the surface, and material ejection into the intra-cluster media are features of each of these models and consequently they can all be made to *qualitatively* agree with the observed elemental abundances. However, none of the standard models can currently account for all specific abundances (Gratton et al., 2012). AGB and FRMS models are the most promising; however, both models have difficulty reproducing severe O depletion (Ventura & D’Antona, 2009; Decressin et al., 2007). Moreover, AGB and FRMS models require significant mass loss ( $\sim 90\%$ ) between cluster formation and the current epoch — implying that a significant fraction of halo stars formed in GCs (Renzini, 2008; D’Ercole et al., 2008; Bastian & Lardo, 2015).

In addition to the light-element anti-correlations observed it is also known that younger populations are significantly enhanced in Helium (Piotto et al., 2007, 2015; Latour et al., 2019). Depending on the cluster, Helium mass fractions as high as  $Y = 0.4$  have been inferred (e.g Milone et al., 2015a). However, due to the relatively high and tight temperature range of partial ionization for He it cannot be observed in globular clusters; consequently, the evidence for enhanced He in GCs originates from comparison of theoretical stellar isochrones to the observed color-magnitude-diagrams of globular clusters. Therefore, a careful handling of chemistry is essential when modeling with the aim of discriminating between MPs; yet, only a very limited number of GCs have yet been studied with chemically self-consistent (structure and atmosphere) isochrones (e.g. Dotter et al., 2015, NGC 6752).



## Chapter 5

# Modeling Globular Clusters

Due to the importance of globular clusters across domains of astronomy there are multiple ways to model them. Some of these approaches, for work which is primarily focused on the dynamics of clusters and galaxies, treat globular clusters as dynamical systems and study aspects such as evaporation rates and dynamical cooling timescales.

An analytic framework for understanding cluster evaporation was proposed by both [?](#) and [?](#), who suggested an expression for a dimensionless evaporation rate  $\xi$ .

$$\xi \equiv -\frac{t_{rh}}{M} \frac{dM}{dt} \quad (5.1)$$

where  $M$  is the total cluster mass and the relaxation time  $t_{rh}$  is defined as:

$$t_{rh} = \frac{0.14N}{\ln \Lambda} \sqrt{\frac{r_{hm}^3}{GM}} \quad (5.2)$$

Where  $r_{hm}$  is the half mass radius of the cluster. Additionally,  $\Lambda \equiv 0.4N$  and  $N$  is the total number of stars in the cluster. Due to the complexity of cluster mass evaporation, the initial attempts to analytically constrain the value of  $\xi$  have been superseded by numerical calculations. As a result, it has since been shown that both external tidal fields ([?Baumgardt & Makino, 2003](#)) and stellar evolution ([Baumgardt & Makino, 2003](#)) play important roles in determining a cluster's mass loss rate.

Understanding the evaporation and expansion history of GCs can shed light on both the galactic potentials in which the cluster lives, and where the cluster formed

in the galactic potential (?). ? and ? presented early evidence via numeric studies that the primordial binary fraction of a cluster may influence a cluster's core radius expansion rate. Their results show that a direct proportionality between the binary fraction and core radius expansion rates may exist. Further, ? provided empirical evidence, through a study of blue straggler stars (BSS) in M5, that collisional binaries may increase evaporation rates. However, there has yet to be established a firm quantitative relationship between the primordial binary fraction of a cluster and its evolutionary rates

## 5.1 Problems Modeling Globular Clusters

There are some outstanding problems in models of Globular Clusters, primarily these fall into two categories. One, formation channels do not currently capture the observed abundance variations between multiple populations in clusters. This is especially pronounced when considering the timescale involved between early and later population formation.

## Chapter 6

# Multiple Populations in NGC 2808

### 6.1 Introduction

NGC 2808 is the prototype globular cluster to host Multiple Populations. Various studies since 2007 have identified that it may host anywhere from 2-5 stellar populations. These populations have been identified both spectroscopically (i.e. ) and photometrically (i.e. ). Note that recent work ([Valle et al., 2022](#)) calls into question the statistical significance of the detections of more than 2 populations in the spectroscopic data. Here we present new, chemically self-consistent modeling of the photometry of the two extreme populations of NGC 2808 identified by [Milone et al. \(2015a\)](#), populations A and E. We use archival photometry from the Hubble UV Globular Cluster Survey (HUGS) ([Piotto et al., 2015](#); [Milone et al., 2017](#)) in the F275W and F814W passbands to characterize multiple populations in NGC 2808 ([Milone et al., 2015a,b](#)). Additionally, we present a likelihood analysis of the photometric data of NGC 2808 to determine the number of populations present in the cluster.

### 6.2 Stellar Models

We use the Dartmouth Stellar Evolution Program (DSEP, [Dotter et al., 2008](#)) to generate stellar models. DSEP is a well-tested, one-dimensional stellar evolution code which includes a mixing length model of convection, gravitational settling, and diffusion. Using the solar composition presented in ([Grevesse et al., 2007](#)) (GAS07),

MARCS model atmospheres, OPLIB high temperature opacities, and AESOPUS 2.0 low temperature opacities we find a solar calibrated mixing length parameter,  $\alpha_{MLT}$ , of  $\alpha_{MLT} = 1.901$ .

We use DSEP to evolve stellar models ranging in mass from 0.3 to 2.0 solar masses from the zero-age main sequence (ZAMS) to the tip of the red giant branch. Below  $0.7 M_\odot$  we evolve a model every  $0.03 M_\odot$  and above  $0.7 M_\odot$  we evolve a model every  $0.5 M_\odot$ . Additionally, we evolve models over a grid of mixing length parameters from  $\alpha_{MLT} = 1.0$  to  $\alpha_{MLT} = 2.0$  in steps of 0.1. In addition to the mixing length grid the evolved grid of models also has dimensions population (A or E) (Table 6.1) and helium abundance ( $Y = 0.24, 0.27, 0.3, 0.33, 0.36, 0.39$ ). Each model is evolved in DSEP with typical numeric tolerances of one part in  $10^7$ . Each model is allowed a maximum time step of 50 Myr.

For each combination of population,  $Y$ , and  $\alpha_{MLT}$  we use the isochrone generation code first presented in [Dotter \(2016\)](#) to generate a grid of isochrones. The isochrone generation code identified equivalent evolutionary points (EEPs) over a series of masses and interpolates between them. The grid of isochrones generated for this work is available as a digital supplement to this paper. Given the complexity of the parameter space when fitting multiple populations along with the recent warnings in the literature regarding overfitting datasets (e.g. [Valle et al., 2022](#)) we want to develop a more objective way of fitting isochrones to photometry than if we were to mark median ridge line positions by hand.

### 6.3 Chemical Consistency

There are three primary areas in which the stellar models must be made chemically consistent: the atmospheric boundary conditions, the opacities, and interior abundances. The interior abundances are relatively easily handled by adjusting parameters within our stellar evolutionary code. However, the other two areas are more complicated to bring into consistency. Atmospheric boundary conditions and opacities must both be calculated with a consistent set of chemical abundances outside of the stellar evolution code. For evolution we use the Dartmouth Stellar Evolution

Element	$a(X)_A$	$a(X)_E$	Element	$a(X)_A$	$a(X)_E$
Li	-0.08	—	In	-1.46	—
Be	0.25	—	Sn	-0.22	—
B	1.57	—	Sb	-1.25	—
C	6.87	5.91	Te	-0.08	—
N	6.42	6.69	I	-0.71	—
O	7.87	6.91	Xe	-0.02	—
F	3.43	—	Cs	-1.18	—
Ne	7.12	6.7	Ba	1.05	—
Na	5.11	5.7	La	-0.03	—
Mg	6.86	6.42	Ce	0.45	—
Al	5.21	6.61	Pr	-1.54	—
Si	6.65	6.77	Nd	0.29	—
P	4.28	—	Pm	-99.0	—
S	6.31	5.89	Sm	-1.3	—
Cl	-1.13	4.37	Eu	-0.61	—
Ar	5.59	5.17	Gd	-1.19	—
K	3.9	—	Tb	-1.96	—
Ca	5.21	—	Dy	-1.16	—
Sc	2.02	—	Ho	-1.78	—
Ti	3.82	—	Er	-1.34	—
V	2.8	—	Tm	-2.16	—
Cr	4.51	—	Yb	-1.42	—
Mn	4.3	—	Lu	-2.16	—
Fe	6.37	—	Hf	-1.41	—
Co	3.86	—	Ta	-2.38	—
Ni	5.09	—	W	-1.41	—
Cu	3.06	—	Re	-2.0	—
Zn	2.3	—	Os	-0.86	—
Ga	0.78	—	Ir	-0.88	—
Ge	1.39	—	Pt	-0.64	—
As	0.04	—	Au	-1.34	—
Se	1.08	—	Hg	-1.09	—
Br	0.28	—	Tl	-1.36	—
Kr	0.99	—	Pb	-0.51	—
Rb	0.26	—	Bi	-1.61	—
Sr	0.61	—	Po	-99.0	—
Y	1.08	—	At	-99.0	—
Zr	1.45	—	Rn	-99.0	—
Nb	-0.8	—	Fr	-99.0	—
Mo	-0.38	—	Ra	-99.0	—
Tc	-99.0	—	Ac	-99.0	—
Ru	-0.51	—	Th	-2.2	—
Rh	-1.35	—	Pa	-99.0	—
Pd	-0.69	—	U	-2.8	—

Table 6.1: Relative Metal composition used where  $a(H) = 12$ . Where the relative composition is the same for both populations A and E it is only listed in the population A column for the sake of visual clarity.

Program (DSEP) ([Dotter et al., 2008](#)), a well tested 1D stellar evolution code which has a particular focus on modelling low mass stars ( $\leq 2 M_{\odot}$ )

### 6.3.1 Atmospheric Boundary Conditions

Certain assumptions, primarily that the radiation field is at equilibrium and radiative transport is diffusive ([Salaris & Cassisi, 2005](#)), made in stellar structure codes, such as DSEP, are valid when the optical depth of a star is small. However, in the atmospheres of stars, the number density of particles drops low enough and the optical depth consequently becomes large enough that these assumptions break down, and separate, more physically motivated, plasma modeling code is required. Generally structure code will use tabulated atmospheric boundary conditions generated by these specialized codes ATLAS9 ([Kurucz, 1993](#)), PHEONIX ([Husser et al., 2013](#)), MARCS ([Gustafsson et al., 2008](#)), and MPS-ATLAS ([Kostogryz et al., 2023](#)). Often, as the boundary conditions are both expensive to compute and not the speciality of stellar structure researchers, the boundary conditions are not updated as as light-element interior abundance varies.

One key element when chemically consistently modeling NGC 2808 modeling is the incorporation of new atmospheric models with the same elemental abundances as the structure code. We use atmospheres generated from the MARCS grid of model atmospheres ([Plez, 2008](#)). MARCS provides one-dimensional, hydrostatic, plane-parallel and spherical LTE atmospheric models ([Gustafsson et al., 2008](#)). Model atmospheres are made to match the spectroscopically measured elemental abundances of populations A and E. Moreover, for each populations, atmospheres with various helium mass fractions are generated. These range from  $Y=0.24$  to  $Y=0.36$  in steps of 0.02. All atmospehric models are computed to an optical depth of  $\tau = 100$  where their temperature and pressures serves as boundary conditions for the strudcure code. A comparison of the pressure and temperature throughout the atmospheres of the two populations with helium abundances representative of literature values is shown in Figure ??.

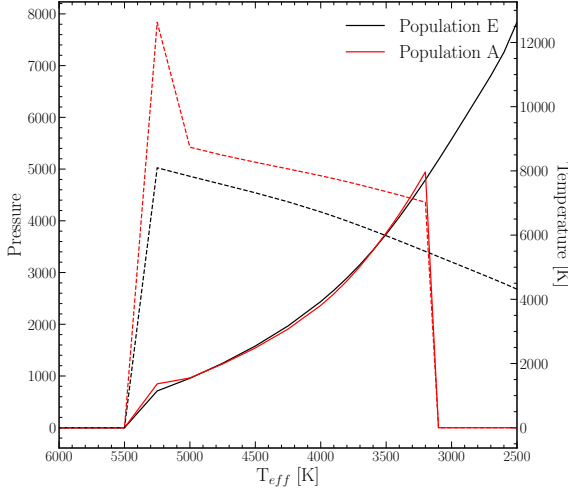


Figure 6.1: Comparison of the MARCS model atmospheres generated for the two extreme populations of NGC 2808. These lines shows population A and E with the same Helium abundance; though, we fit a grid of models over various helium abundances. Dashed lines show the temperature of the boundary condition while solid lines show the pressure.

### 6.3.2 Opacities

In addition to the atmospheric boundary conditions, both the high and low temperature opacities used by DSEP must be made chemically consistent. Here we use OPLIB high temperature opacity tables (Colgan et al., 2016) retrieved using the TOPS web-interface. Low temperature opacity tables are retrieved from the Aesopus 2.0 web-interface (Marigo & Aringer, 2009; Marigo et al., 2022). Ideally, these opacities would be the same used in the atmospheric models. However, the opacities used in the MARCS models are not publicly available. As such, we use the opacities provided by the TOPS and Aesopus 2.0 web-interfaces.

## 6.4 fidanka

When fitting isochrones to the data we have four main criteria for any method

- The method must be robust enough to work along the entire main sequence, turn off, and much of the subgiant and red giant branches.
- Any method should consider photometric uncertainty in the fitting process.

- The method should be model independent, weighting any n number of populations equally.
- The method should be automated and require minimal intervention from the user.

We do not believe that any currently available software is a match for our use case. Therefore, we elect to develop our own software suite, **Fidanka**. **Fidanka** is a python package designed to automate much of the process of measuring fiducial lines in CMDs, adhering to the four criteria we lay out above. Primary features of **Fidanka** may be separated into three categories: fiducial line measurement, stellar population synthesise, and isochrone optimization/fitting. Additionally, there are utility functions which are detailed in the **Fidanka** documentation.

#### 6.4.1 Fiducial Line Measurement

**Fidanka** takes a iterative approach to measuring fiducial lines, the first step of which is to make a “guess” as to the fiducial line. . This initial guess is calculated by splitting the CMD into magnitude bins, with uniform numbers of stars per bin (so that bins are cover a small magnitude range over densely populated regions of the CMD while covering a much larger magnitude range in sparsely populated regions of the CMD, such as the RGB). A unimodal Gaussian distribution is then fit to the color distribution of each bin, and the resulting mean color is used as the initial fiducial line guess. This rough fiducial line will approximately trace the area of highest density. The initial guess will be used to verticalize the CMD so that further algorithms can work in 1-D magnitude bins without worrying about weighting issues caused by varying projections of the evolutionary sequence onto the magnitude axis. Verticalization is preformed taking the difference between the guess fiducial line and the color of each star in the CMD.

If **Fidanka** were to simply apply the same algorithm to the verticalized CMD then the resulting fiducial line would likely be a re-extraction of the initial fiducial line guess. To avoid this, we take a more robust, number density based approach, which considers the distribution of stars in both color and magnitude space simultaneously.

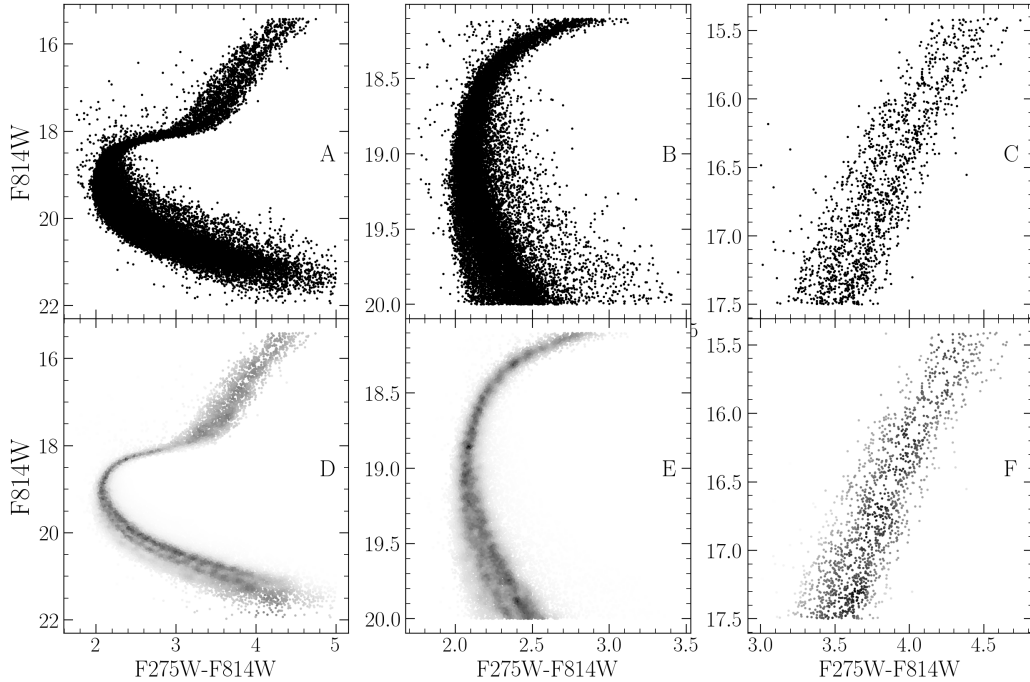


Figure 6.2: Density map demo showing density estimate over different parts of the evolutionary sequence. The left panel shows the density map over the entire evolutionary sequence, while the middle panel shows the density map over the main sequence and the right most panel shows the density map over the RGB. Figures in the top row are the raw CMD, while figures in the bottom row are colored by the density map.

For each star in the CMD we first use a `introselect` partitioning algorithm to select the 50 nearest stars in F814W vs. F275W-F814W space. To account for the case where the star is at an extreme edge of the CMD, those 50 stars include the star itself (such that we really select 49 stars + 1). We use `qhull`<sup>1</sup>(Barber et al., 1996; ?) to calculate the convex hull of those 50 points. The number density at each star then is defined as  $50/A_{hull}$ , where  $A_{hull}$  is the area of the convex hull. Because we use a fixed number of points per star, and a partitioning algorithm as opposed to a sorting algorithm, this method scales like  $\mathcal{O}(n)$ , where  $n$  is the number of stars in the CMD. This method also intrinsically weights the density of each star equally as the counting statistics per bin are uniform. We are left with a CMD where each star has a defined number density (Figure ??).

**Fidanka** can now exploit this density map to fit a better fiducial line to the data, as

---

<sup>1</sup><https://www.qhull.com>

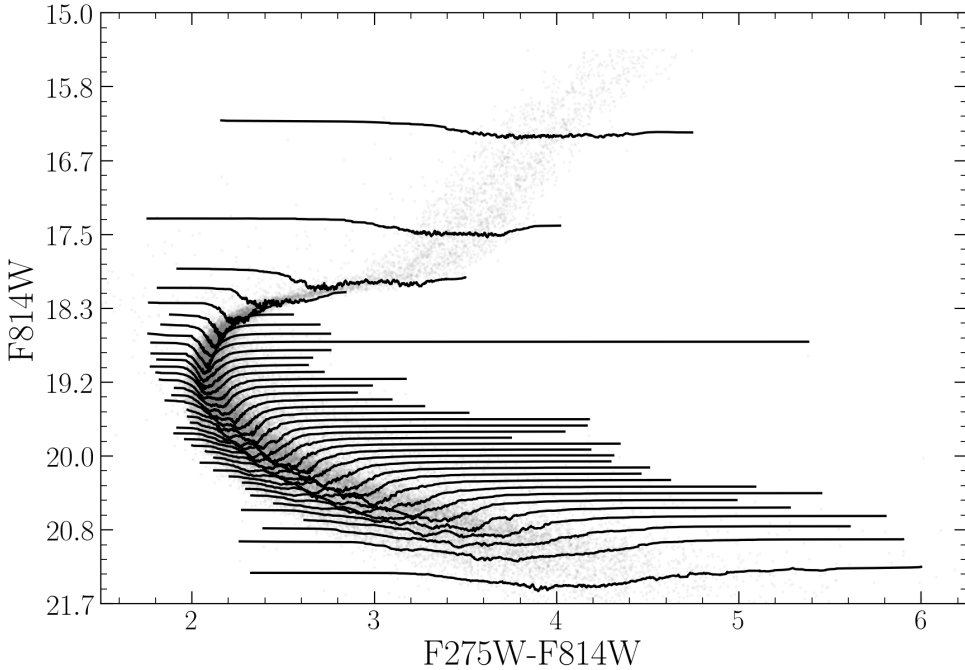


Figure 6.3: CMD where points are colored by density. Lines show the density-color profile in each magnitude bin. In this figure adaptive binning targeted 1000 stars per bin

the density map is far more robust to outliers. There are multiple algorithms we implement to fit the fiducial line to the color-density profile in each magnitude bin (Figure ??); they are explained in more detail in the `Fidanka` documentation. However, of most relevance here is the Bayesian Gaussian Mixture Modeling (BGMM) method. BGMM is a clustering algorithm which, for some fixed number of n-dimensional Gaussian distributions,  $K$ , determines the mean, covariance, and mixing probability (somewhat analogous to amplitude) of each  $k^{th}$  distribution, such that the local lower bound of the evidence of each star belonging strongly to a single distribution is maximized.

Maximization is preformed using the Dirichlet process, which is a non-parametric Bayesian method of determining the number of Gaussian distributions,  $K$ , which best fit the data (Ferguson, 1973; Pedregosa et al., 2011). Use of the Dirichlet process allows for dynamic variation in the number of inferred populations from magnitude bin to magnitude bin. Specifically, populations are clearly visually separated from the lower main sequence through the turn off; however, at the turn off and throughout

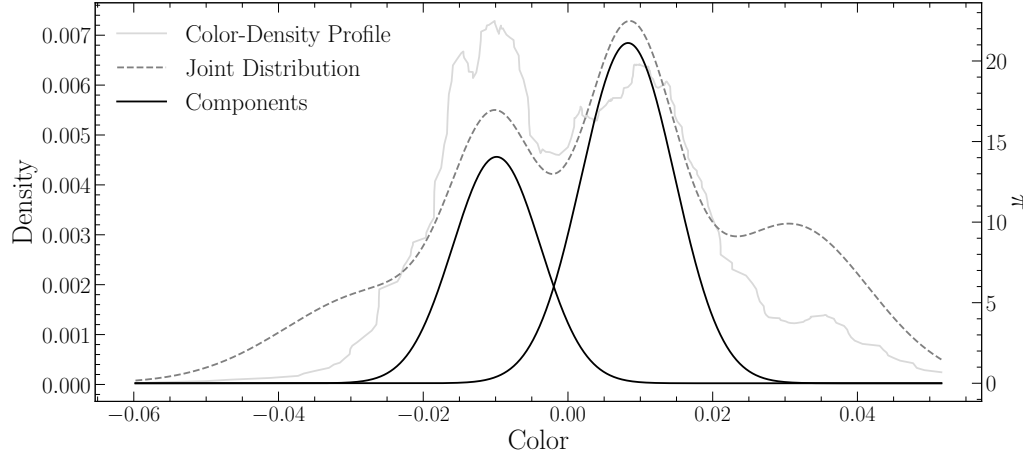


Figure 6.4: Example of BGMM fit to a magnitude bin. The grey line shows the underlying color-density profile, while the black dashed-line shows the joint distribution of each BGMM component. The solid black lines show the two selected components.

much of the subgiant branch, the two visible populations overlap due to their extremely similar ages (i.e. Jordán et al., 2002). The Dirichlet process allows for the BGMM method to infer a single population in these regions, while inferring two populations in regions where they are clearly separated. More generally, the use of the Dirichlet process removes the need for a prior on the exact number of populations to fit. Rather, the user specifies a upper bound on the number of populations within the cluster. An example bin ( $F814W = 20.6$ ) is shown in Figure 6.4.

Fidanka's BGMM method first breaks down the verticalized CMD into magnitude bins with uniform numbers of stars per bin (here we adopt 250). Any stars left over are placed into the final bin. For each bin a BGMM model with a maximum of 5 populations is fit to the color density profile. The number of populations is then inferred from the weighting parameter (the mixing probability) of each population. If the weighting parameter of any  $k^{th}$  components less than 0.05, then that component is considered to be spurious and removed. Additionally, if the number of populations in the bin above and the bin below are the same, then the number of populations in the current bin is forced to be the same as the number of populations in the bin above. Finally, the initial guess fiducial line is added back to the BGMM inferred line. Figure 6.5 shows the resulting fiducial line(s) in each magnitude bin for both a verticalized CMD and a non verticalized CMD.

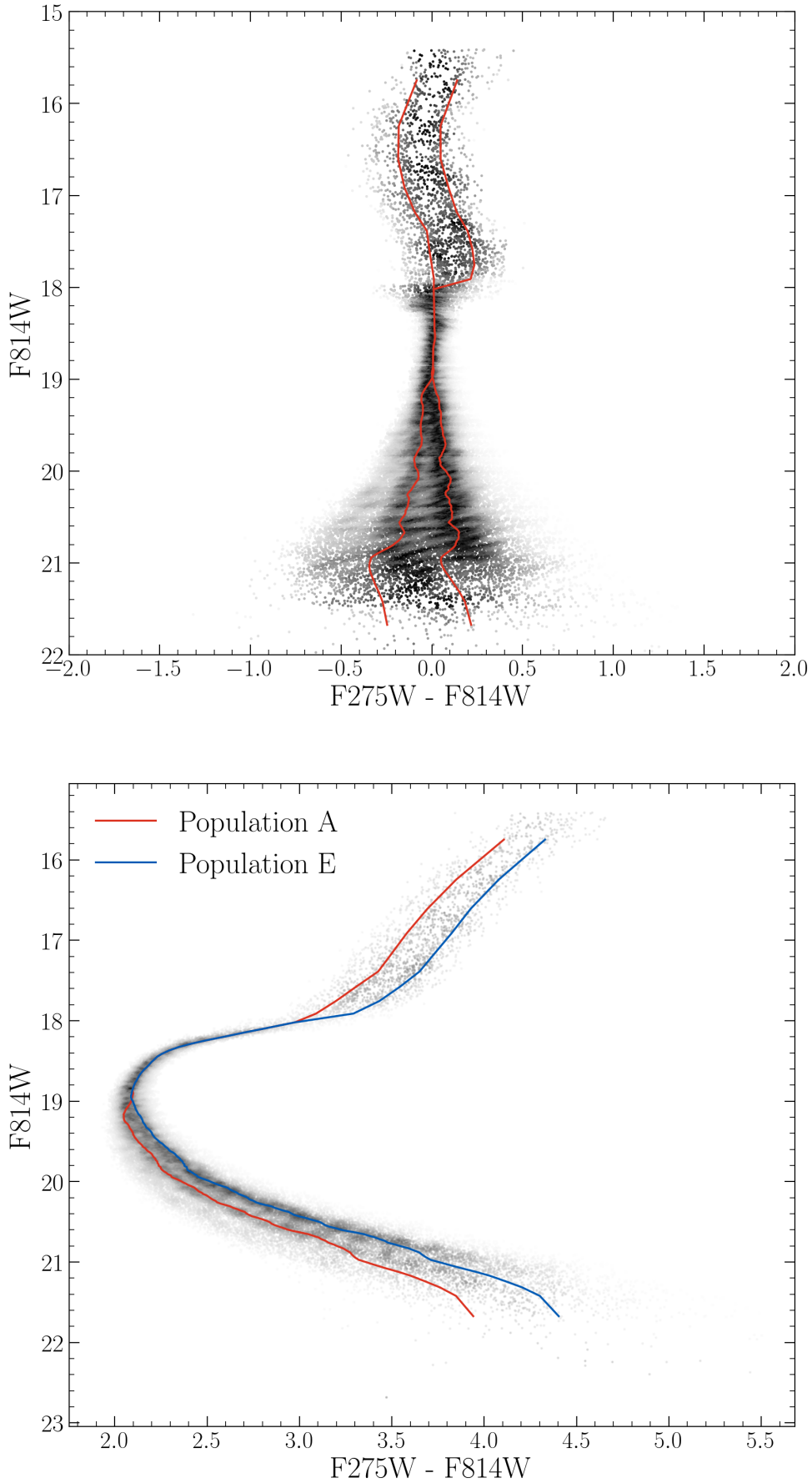


Figure 6.5: CMD where points are colored by density. Line trace the inferred fiducial line(s) in each magnitude bin.

This method of fiducial line extraction effectively discriminated between multiple populations long the main sequence and RGB of a cluster, while simultaneously allowing for the presence of a single population along the MSTO and subgiant branch.

We can adapt this density map based BGMM method to consider photometric uncertainties by adopting a simple Monte Carlo approach. Instead of measuring the fiducial line(s) a single time, **Fidanka** can measure the fiducial line(s) many times, resampling the data with replacement each time. For each resampling **Fidanka** adds a random offset to each filter based on the photometric uncertainties of each star. From these  $n$  measurements the mean fiducial line for each sequence can be identified along with upper and lower bound confidence intervals in each magnitude bin.

#### 6.4.2 Stellar Population Synthesis

In addition to measuring fiducial lines, **Fidanka** also includes a stellar population synthesise module. This module is used to generate synthetic CMDs from a given set of isochrones. This is of primary importance for binary population modelling. The module is also used to generate synthetic CMDs for the purpose of testing the fiducial line extraction algorithms against priors.

**Fidanka** uses MIST formatted isochrones (Dotter, 2016) as input along with distance modulus, B-V color excess, binary mass fraction, and bolometric corrections. An arbitrarily large number of isochrones may be used to define an arbitrary number of populations. Synthetic stars are samples from each isochrone based on a definable probability (for example it is believed that  $\sim 90\%$  of stars in globular clusters are younger population (e.g. Suntzeff & Kraft, 1996; Carretta, 2013)). Based on the metallicity,  $\mu$ , and E(B-V) of each isochrone, bolometric corrections are taken from bolometric correction tables. Where bolometric correction tables do not include exact metallicities or extinctions a linear interpolation is performed between the two bounding values.

### 6.4.3 Isochrone Optimization

The optimization routines in **Fidanka** will find the best fit distance modulus, B-V color excess, and binary number fraction for a given set of isochrones. If a single isochrone is provided then the optimization is done by minimizing the  $\chi^2$  of the perpendicular distances between an isochrone and a fiducial line. If multiple isochrones are provided then those isochrones are first used to run stellar population synthesis and generate a synthetic CMD. The optimization is then done by minimizing the  $\chi^2$  of both the perpendicular distances between and widths of the observed fiducial line and the fiducial line of the synthetic CMD.

### 6.4.4 Fidanka Testing

In order to validate **fidanka** we have run a series of injection recovery tests using **Fidanka**'s population synthesis routines to build various synthetic populations and **Fidanka**'s fiducial measurement routines to recover these populations. Each population was generated using the initial mass function given in (Milone et al., 2012) for the redmost population ( $\alpha = -1.2$ ). Further, every population was given a binary population fraction of 10%, distance uniformly sampled between 5000pc and 15000pc, and a B-V color excess uniformly sampled between 0 and 0.1. Finally, each synthetic population was generated using a fixed age uniformly sampled between 7 Gyr and 14 Gyr. An example synthetic population along with its associated best fit isochrone are shown in Figure 6.6.

For each trial we use **Fidanka** to measure the fiducial line and then optimize that fiducial line against the originating isochrone to estimate distance modulus, age, and color B-V excess. Figure 6.7 is built from 1000 runs of these trials and show the mean and width of the percent error distributions for  $\mu$ ,  $E(B - V)$ , and age. In general **Fidanka** is able to recover distance moduli effectively with age and E(B-V) recovery falling in line with other literature that does not consider the CMD outside of the main sequence, main sequence turn off, sub giant, and red giant branches; specifically, it should be noted that **Fidanka** is not setup to model the horizontal branch.

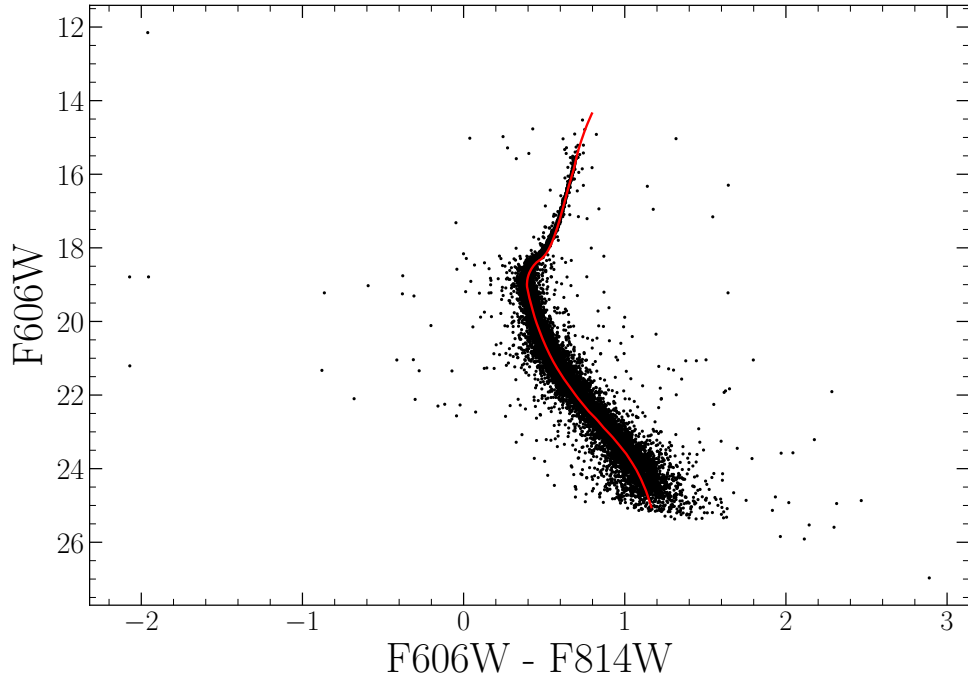


Figure 6.6: Synthetic population generated by fidanka at 10000pc with  $E(B-V) = 0$ , and an age of 12 Gyr along with the best fitting isochrone. The best fit paremeters are derived to be  $\mu = 15.13$ ,  $E(B-V)=0.001$ , and an age of 12.33 Gyr.

## 6.5 Isochrone Fitting

We fit pairs of isochrones to the HUGS data for NGC 2808 using `Fidanka` , as descrbed in §6.4. Two isochrones, one for Population A and one for Population E are fit simultaneously. These isochrones are constrained to have distance modulus,  $\mu$ , and color excess,  $E(B-V)$  which agree to within 1%. Moreover, we constrain the mixing length,  $\alpha_{ML}$ , for any two isochrones in a set to be within 0.5 of one and other. For every isochrone in the set of combination of which fulfilling these constraints  $\mu$ ,  $E(B-V)$ ,  $Age_A$ , and  $Age_B$  are optimized to reduce the  $\chi^2$  distance between the fiducial lines and the isochrones. Because we fit fiducial lines directly, we do not need to consider the binary population fraction,  $f_{bin}$ , as a free parameter.

The best fit isochrones are shown in Figure ?? and optimized parameters for these are presented in Table ?? . We find helium mas fractions which are consistent with those identified in past literature (e.g. Milone et al., 2015a). Note that our helium mass fraction grid has a spacing of 0.03 between grid points and we are therefore

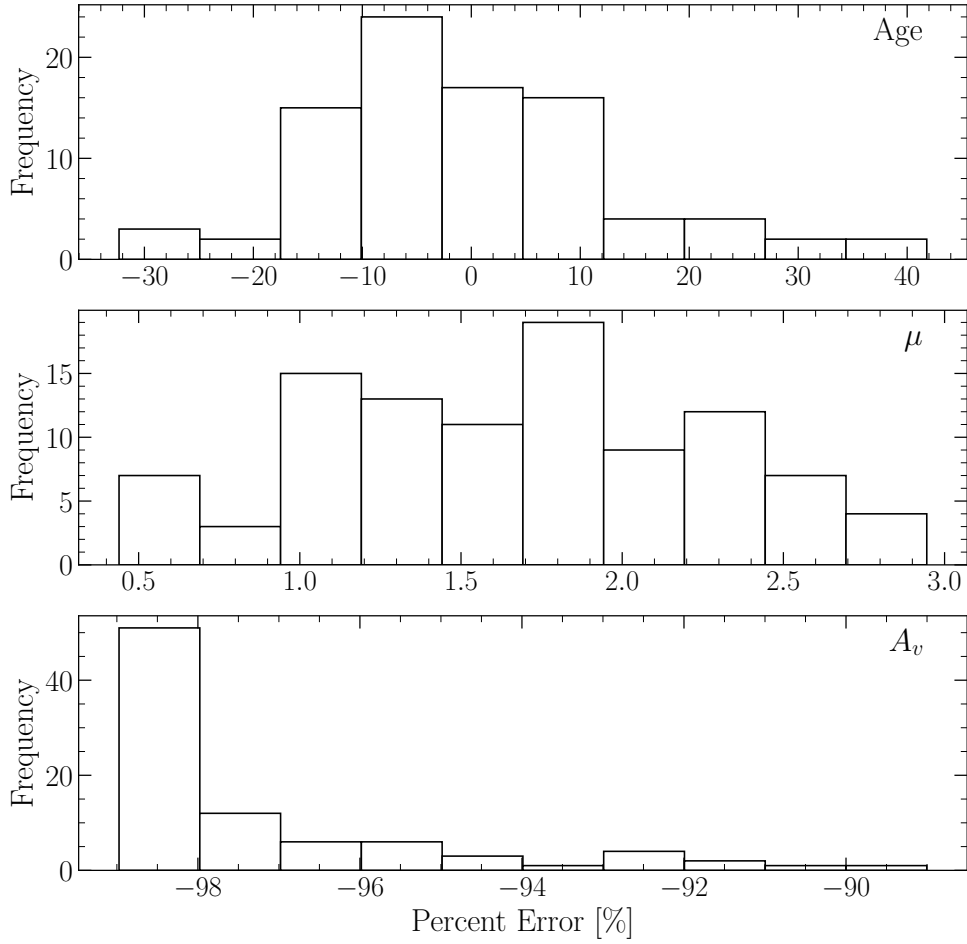


Figure 6.7: Percent Error distribution for each of the three deriver parameters. Note that these values will be sensitive to the magnitude uncertainties of the photometry. Here we made use of the ACS artificial star tests to estimate the uncertainties. **Note** that currently this is built with 100 runs, these take a long time so currently re running with 1000 runs.

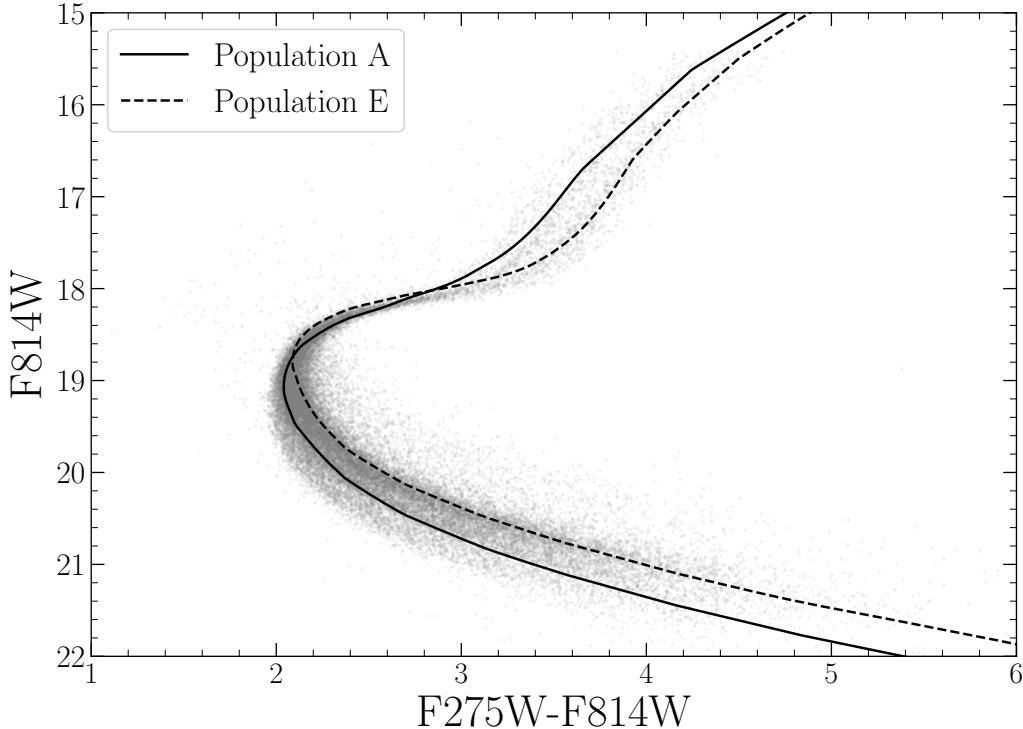


Figure 6.8: Best fit isochrone results for NGC 2808.

population	age [Gyr]	distance modulus	extinction [mag]	Y	$\alpha_{ML}$	$\chi^2_\nu$
A	12.3	14.91	0.54	0.24	1.901	0.014
E	14.3	14.96	0.54	0.39	1.750	0.017

Table 6.2: Best fit parameters derived from fitting isochrones to the fiducial lines derived from the NCG 2808 photometry.

unable to resolve between certain proposed helium mass fractions for the younger sequence (for example between 0.37 and 0.39).

Past literature (e.g. Milone et al., 2015a, 2018) have found helium mass fraction variation from the low redmost to bluest populations of  $\sim 0.12$ . Here we find a helium mass fraction variation of 0.15 which, given the spacing of the helium grid we use **is consistent with these past results**.

### 6.5.1 The Number of Populations in NGC 2808

In order to estimate the number of populations which ideally fit the NGC 2808 F275W-F814W photometry without overfitting the data we make use of silhouette

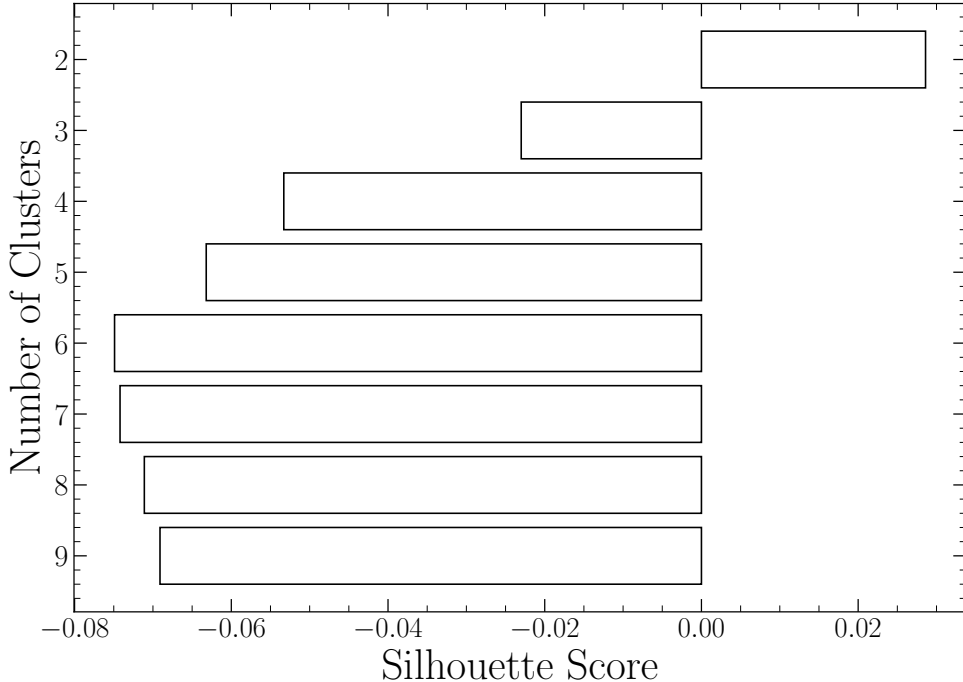


Figure 6.9: Silhouette analysis for NGC 2808 F275W-F814W photometry. The Silhouette scores are an average of score for each magnitude bin. Positive scores indicate that the clustering algorithm produced well distinguished clusters while negative scores indicate clusters which are not well distinguished.

analysis (Rousseeuw, 1987, and in a similar manner to how Valle et al. (2022) perform their analysis of spectroscopic data). We find the average silhouette score for all tagged clusters identified using BGMM in all magnitude bins over the CMD using the standard python module `sklearn`. Figure 6.9 shows the silhouette analysis results and that 2 populations fit the photometry most ideally. This is in line with what our BGMM model predicts for the majority of the the CMD.

### 6.5.2 ACS-HUGS Photometric Zero Point Offset

The Hubble legacy archive photometry used in this work is calibrated to the Vega magnitude system. However, we have found that the photometry has a systematic offset of  $\sim 0.026$  magnitudes in the F814W band when compared to the same stars in the ACS survey (Figure ??). The exact cause of this offset is unknown, but it is likely due to a difference in the photometric zero point between the two surveys. A full correction of this offset would require a careful re-reduction of the HUGS

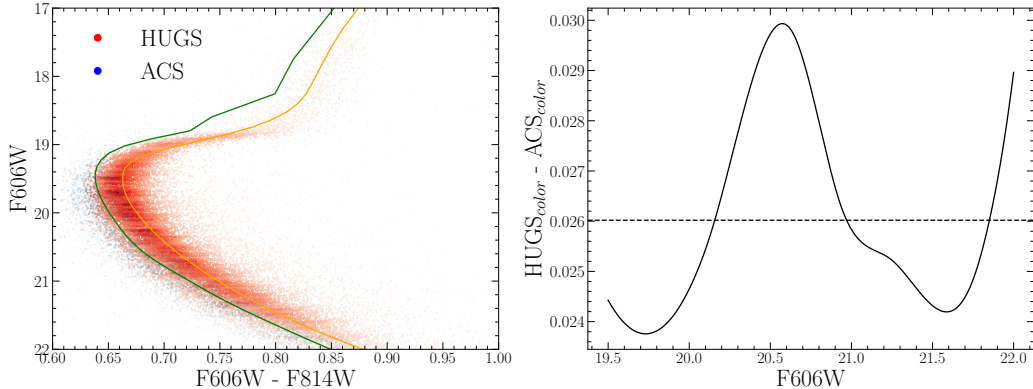


Figure 6.10: (left) CMD showing the photometric offset between the ACS and HUGS data for NGC 2808. CMDs have been randomly subsampled and colored by point density for clarity. (right) Mean difference between the color of the HUGS and ACS fiducial lines at the same magnitude. Note that the ACS data is systematically bluer than the HUGS data.

photometry, which is beyond the scope of this work. We instead recognize a 0.02 inherent uncertainty in the inferred magnitude of any fit when comparing to the ACS survey. This uncertainty is small when compared to the uncertainty in the distance modulus and should not affect the conclusion of this paper.

The observed photometric offset between ACS and HUGS reductions introduces a systematic uncertainty when comparing parameters derived from isochrone fits to ACS data vs those fit to HUGS data. Specifically, this offset introduces a  $\sim$ AGE Gyr uncertainty. Moreover, for two isochrone of the same age, only separated by helium mass fraction, a shift of the main sequence turn off is also expected. Figure 6.11 shows this shift. Note a change in the helium mass fraction of a model by 0.03 results in an approximate 0.08 magnitude shift to the main sequence turn off location. This means that the mean 0.026 magnitude offset we find in between ACS and HUGS data corresponds to an additional approximate 0.01 uncertainty in the derived helium mass fraction when comparing between these two datasets.

## 6.6 Results

Using `Fidanka` we fit pairs of Population A + E isochrones to the HUGS data for NGC 2808. Each pair of isochrones is allowed to vary in distance modulus, reddening,

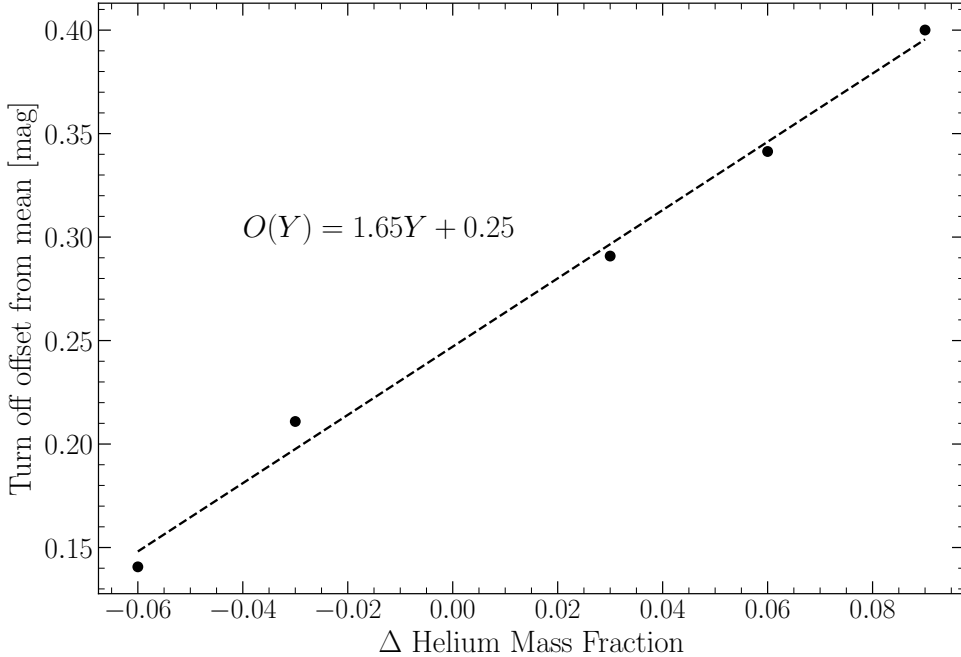


Figure 6.11: Main sequence turn off magnitude offset from a guage helium mass fraction ( $Y=0.30$  chosen). All main sequence turn off locations are measured at 12.3 Gyr [Should I make these contour surfaces for various ages?](#)

population	age [Gyr]	distance modulus	extinction mag	$Y$	$\alpha_{ML}$	$\chi^2_\nu$
A	12.3	14.91	0.54	0.24	1.901	0.014
E	14.3	14.96	0.54	0.39	1.750	0.017

Table 6.3: Best fit parameters derived from fitting isochrones to the fiducial lines derived from the NCG 2808 photometry.

relative helium mass fraction (A/E), and age. Any population pairs which vary by more than 1% in distance modulus or B-V color excess are rejected. The  $\chi^2$  distribution for the isochrone pairs is shown in Figure [FIGURE]. The best fit isochrones are shown in Figure ?? and optimized parameters for these are presented in Table [TABLE].

Need to make the chi2 dist plot still. Have all these values but need to figure out best way to visualize it

Currently are still seeing a discontinuity in the isochrone below the MSTO. This must be addressed before submission.

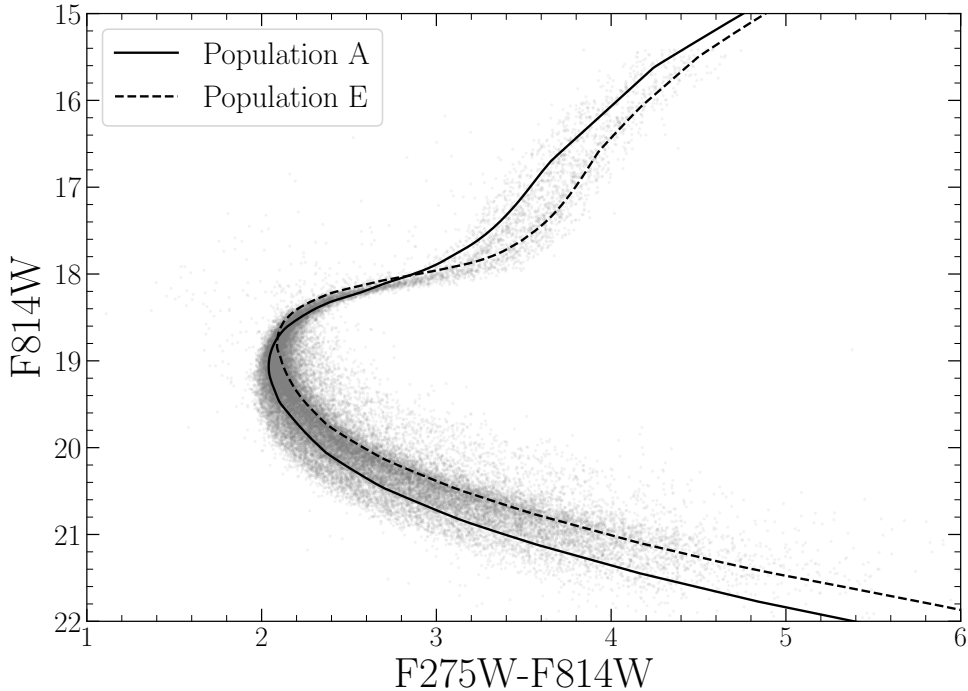


Figure 6.12: Best fit isochrone results for NGC 2808.

### 6.6.1 The Number of Populations in NGC 2808

Fidanka provides a somewhat straightforward way to estimate the number of populations expected in a given magnitude bin given the observations. See Section 6.4 for specific implementation details. Here we perform an analysis of the number of populations seen in the NGC 2808 F814W-F274W vs F814W color-magnitude diagram. We find that for the majority of the main sequence and red giant branches BGMM prefers two populations; whereas, near the main sequence turn off and on the majority of the subgiant branches BGMM prefers a single population model.

[FIGURE SHOWING BGMM population probability]

## 6.7 Conclusion

Here we have performed the first chemically self-consistent modeling of the Milky Way Globular Cluster NGC 2808. We find that, updated atmospheric boundary conditions and opacity tables do not have a significant effect on the inferred helium abundances of multiple populations. Specifically, we find that the older stellar pop-

ulation, population A, has a helium mass fraction of 0.24, while the older population, E, has a helium mass fraction of 0.39.

Further, we introduce a new software suite for globular cluster science, **Fidanka**, which has been released under a permissive open source license. **Fidanka** aims to provide a statistically robust set of tools for estimating the parameters of multiple populations within globular clusters.

## Chapter 7

# Modeling NGC 6752



## Chapter 8

# Gap Sensitivity to Opacity Source

### 8.1 INTRODUCTION

Due to the initial mass requirements of the molecular clouds which collapse to form stars, star formation is strongly biased towards lower mass, later spectral class stars when compared to higher mass stars. Partly as a result of this bias and partly as a result of their extremely long main-sequence lifetimes, M Dwarfs make up approximately 70 percent of all stars in the galaxy. Moreover, some planet search campaigns have focused on M Dwarfs due to the relative ease of detecting small planets in their habitable zones (e.g. [Nutzman & Charbonneau, 2008](#)). M Dwarfs then represent both a key component of the galactic stellar population as well as the possible set of stars which may host habitable exoplanets. Given this key location M Dwarfs occupy in modern astronomy it is important to have a thorough understanding of their structure and evolution.

[Jao et al. \(2018\)](#) discovered a novel feature in the Gaia Data Release 2 (DR2)  $G_{BP} - G_{RP}$  color-magnitude-diagram. Around  $M_G = 10$  there is an approximately 17 percent decrease in stellar density of the sample of stars [Jao et al. \(2018\)](#) considered. Subsequently, this has become known as either the Jao Gap, or Gaia M Dwarf Gap. Following the initial detection of the Gap in DR2 the Gap has also potentially been observed in 2MASS ([Skrutskie et al., 2006](#); [Jao et al., 2018](#)); however, the significance of this detection is quite weak and it relies on the prior of the Gap's location from Gaia data. Further, the Gap is also present in Gaia Early Data Release 3 (EDR3)

(Jao & Feiden, 2021). These EDR3 and 2MASS data sets then indicate that this feature is not a bias inherent to DR2.

The Gap is generally attributed to convective instabilities in the cores of stars straddling the fully convective transition mass (0.3 - 0.35 M<sub>⊕</sub>) (Baraffe & Chabrier, 2018). These instabilities interrupt the normal, slow, main sequence luminosity evolution of a star and result in luminosities lower than expected from the main sequence mass-luminosity relation (Jao & Feiden, 2020).

The Jao Gap, inherently a feature of M Dwarf populations, provides an enticing and unique view into the interior physics of these stars (Feiden et al., 2021). This is especially important as, unlike more massive stars, M Dwarf seismology is infeasible due to the short periods and extremely small magnitudes which both radial and low-order low-degree non-radial seismic waves are predicted to have in such low mass stars (Rodríguez-López, 2019). The Jao Gap therefore provides one of the only current methods to probe the interior physics of M Dwarfs.

Despite the early success of modeling the Gap some issues remain. Jao & Feiden (2020, 2021) identify that the Gap has a wedge shape which has not been successfully reproduced by any current modeling efforts and which implies a somewhat unusual population composition of young, metal-poor stars. Further, Jao & Feiden (2020) identify substructure, an additional over density of stars, directly below the Gap, again a feature not yet fully captured by current models.

All currently published models of the Jao Gap make use of OPAL high temperature radiative opacities. Here we investigate the effect of using the more up-to-date OPLIB high temperature radiative opacities and whether these opacity tables bring models more in line with observations. In Section 8.2 we provide an overview of the physics believed to result in the Jao Gap, in Section 8.3 we review the differences between OPAL and OPLIB and describe how we update DSEP to use OPLIB opacity tables. Section 9.3 walks through the stellar evolution and population synthesis modeling we perform. Finally, in Section 10.4 we present our findings.

## 8.2 Jao Gap

A theoretical explanation for the Jao Gap (Figure 8.1) comes from [van Saders & Pinsonneault \(2012\)](#), who propose that in a star directly above the transition mass, due to asymmetric production and destruction of  ${}^3\text{He}$  during the proton-proton I chain (ppI), periodic luminosity variations can be induced. This process is known as convective-kissing instability. Very shortly after the zero-age main sequence such a star will briefly develop a radiative core; however, as the core temperature exceeds  $7 \times 10^6$  K, enough energy will be produced by the ppI chain that the core once again becomes convective. At this point the star exists with both a convective core and envelope, in addition to a thin, radiative layer separating the two. Subsequently, asymmetries in ppI affect the evolution of the star's convective core.

While kissing instability has been the most widely adopted model to explain the existence of the Jao Gap, slightly different mechanisms have also been proposed. [MacDonald & Gizis \(2018\)](#) make use of a fully implicit stellar evolution suite which treats convective mixing as a diffusive property. [MacDonald & Gizis](#) treat convective mixing this way in order to account for a core deuterium concentration gradient proposed by [Baraffe et al. \(1997\)](#). Under this treatment the instability results only in a single mixing event — as opposed to periodic mixing events. Single mixing events may be more in line with observations (see section 10.4 for more details on how periodic mixings can effect a synthetic population) where there is only well documented evidence of a single gap. However, recent work by [Jao & Feiden \(2021\)](#) which identify an second under density of stars below the canonical gap, does leave the door open for the periodic mixing events.

The proton-proton I chain constitutes three reactions

1.  $p + p \longrightarrow d + e^+ + \nu_e$
2.  $p + d \longrightarrow {}^3\text{He} + \gamma$
3.  ${}^3\text{He} + {}^3\text{He} \longrightarrow {}^3\text{He} + 2p$

Initially, reaction 3 of ppI consumes  ${}^3\text{He}$  at a slower rate than it is produced by reac-

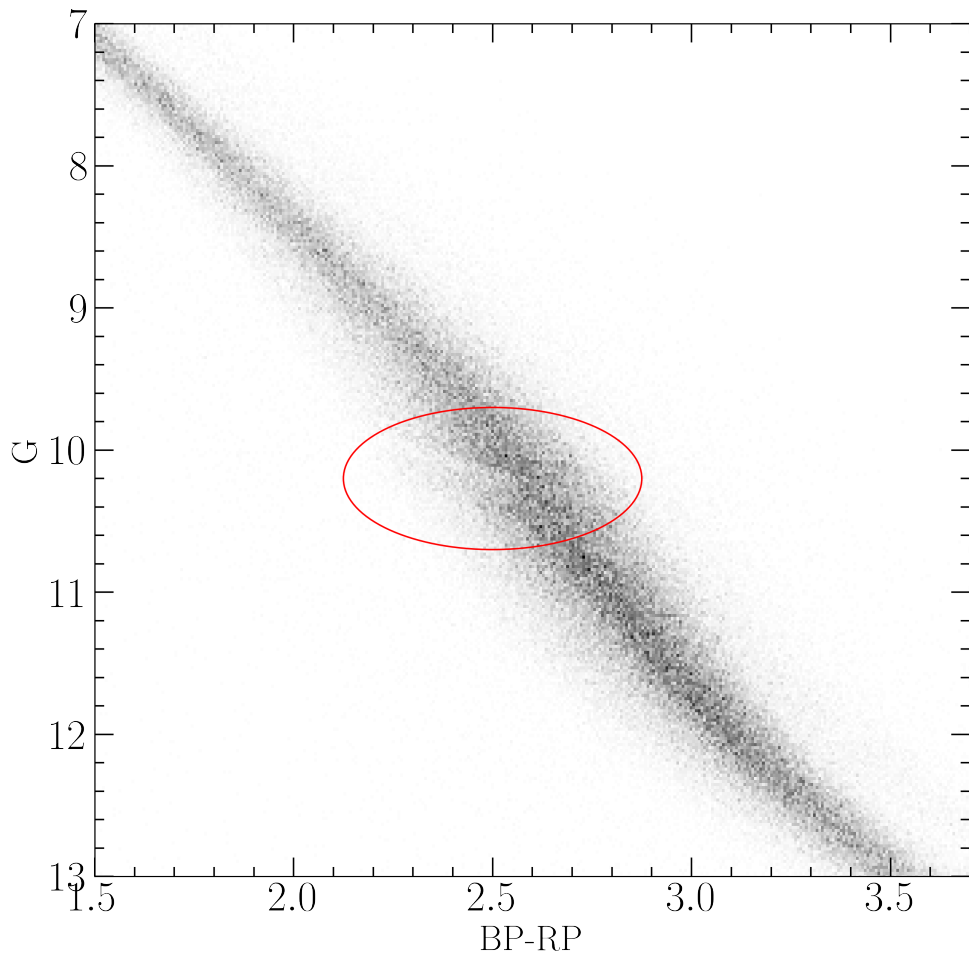


Figure 8.1: The Jao Gap (circled) seen in the Gaia Catalogue of Nearby Stars ([Gaia Collaboration et al., 2021](#)).

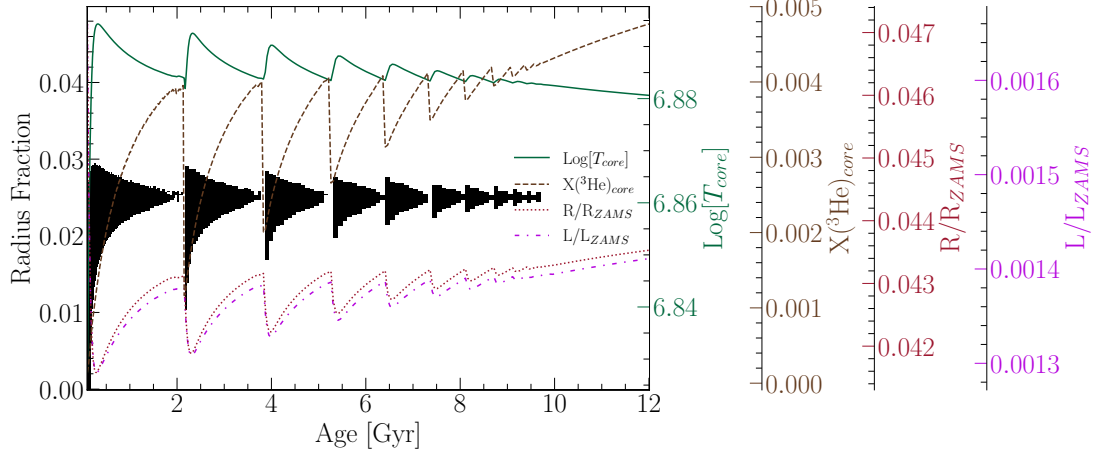


Figure 8.2: Diagram for a characteristic stellar model of  $0.35625 M_{\odot}$  which is within the Jao Gap’s mass range. The black shaded regions denote whether, at a particular model age, a radial shell within the model is radiative (with white meaning convective). The lines trace the models core temperature, core  ${}^3\text{He}$  mass fraction, fractional luminosity wrt. the zero age main sequence and fractional radius wrt. the zero age main sequence.

tion 2 and as a result, the core  ${}^3\text{He}$  abundance and consequently the rate of reaction 3, increases with time. The core convective zone expands as more of the star becomes unstable to convection. This expansion continues until the core connects with the convective envelope. At this point convective mixing can transport material throughout the entire star and the high concentration of  ${}^3\text{He}$  rapidly diffuses outward, away from the core, decreasing energy generation as reaction 3 slows down. Ultimately, this leads to the convective region around the core pulling back away from the convective envelope, leaving in place the radiative transition zone, at which point  ${}^3\text{He}$  concentrations grow in the core until it once again expands to meet the envelope. These periodic mixing events will continue until  ${}^3\text{He}$  concentrations throughout the star reach an equilibrium ultimately resulting in a fully convective star. Figure 8.2 traces the evolution of a characteristic star within the Jao Gap’s mass range.

### 8.2.1 Efforts to Model the Gap

Since the identification of the Gap, stellar modeling has been conducted to better constrain its location, effects, and exact cause. Both [Mansfield & Kroupa \(2021\)](#) and [Feiden et al. \(2021\)](#) identify that the Gap’s mass location is correlated with model

metallicity — the mass-luminosity discontinuity in lower metallicity models being at a commensurately lower mass. [Feiden et al. \(2021\)](#) suggests this dependence is due to the steep relation of the radiative temperature gradient,  $\nabla_{rad}$ , on temperature and, in turn, on stellar mass.

$$\nabla_{rad} \propto \frac{L\kappa}{T^4} \quad (8.1)$$

As metallicity decreases so does opacity, which, by Equation 8.1, dramatically lowers the temperature at which radiation will dominate energy transport ([Chabrier & Baraffe, 1997](#)). Since main sequence stars are virialized the core temperature is proportional to the core density and total mass. Therefore, if the core temperature where convective-kissing instability is expected decreases with metallicity, so too will the mass of stars which experience such instabilities.

The strong opacity dependence of the Jao Gap begs the question: what is the effect of different opacity calculations on Gap properties. As we can see above, changing opacity should affect the Gap’s location in the mass-luminosity relation and therefore in a color-magnitude diagram. Moreover, current models of the Gap have yet to locate it precisely in the CMD ([Feiden et al., 2021](#)) with an approximate 0.16 G-magnitude difference between the observed and modeled Gaps. Opacity provides one, as yet unexplored, parameter which has the potential to resolve these discrepancies.

### 8.3 Updated Opacities

Multiple groups have released high-temperature opacities including, the Opacity Project (OP [Seaton et al., 1994](#)), Laurence Livermore National Labs OPAL opacity tables ([Iglesias & Rogers, 1996](#)), and Los Alamos National Labs OPLIB opacity tables ([Colgan et al., 2016](#)). OPAL high-temperature radiative opacity tables in particular are very widely used by current generation isochrone grids (e.g. Dartmouth, MIST, & StarEvol, [Dotter et al., 2008; Choi et al., 2016; Amard et al., 2019](#)). OPLIB opacity tables ([Colgan et al., 2016](#)) are not widely used but include the most up-to-date

plasma modeling.

While the overall effect on the CMD of using OPLIB compared to OPAL tables is small, the strong theoretical opacity dependence of the Jao Gap raises the potential for these small effects to measurably shift the Gap’s location. We update DSEP to use high temperature opacity tables based on measurements from Los Alamos national Labs T-1 group (OPLIB, [Colgan et al., 2016](#)). The OPLIB tables are created with ATOMIC ([Magee et al., 2004](#); [Hakel et al., 2006](#); [Fontes et al., 2015](#)), a modern LTE and non-LTE opacity and plasma modeling code. These updated tables were initially created in order to incorporate the most up to date plasma physics at the time ([Bahcall et al., 2005](#)).

OPLIB tables include monochromatic Rosseland mean opacities — composed from bound-bound, bound-free, free-free, and scattering opacities — for elements hydrogen through zinc over temperatures 0.5eV to 100 keV (5802 K –  $1.16 \times 10^9$  K) and for mass densities from approximately  $10^{-8}$  g cm $^{-3}$  up to approximately  $10^4$  g cm $^{-3}$  (though the exact mass density range varies as a function of temperature).

DSEP ramps the [Ferguson et al. \(2005\)](#) low temperature opacities to high temperature opacities tables between  $10^{4.3}$  K and  $10^{4.5}$  K; therefore, only differences between high-temperature opacity sources above  $10^{4.3}$  K can effect model evolution. When comparing OPAL and OPLIB opacity tables (Figure 8.3) we find OPLIB opacities are systematically lower than OPAL opacities for temperatures above  $10^5$  K. Between  $10^{4.3}$  and  $10^5$  K OPLIB opacities are larger than OPAL opacities. These generally lower opacities will decrease the radiative temperature gradient throughout much of the radius of a model.

### 8.3.1 Table Querying and Conversion

The high-temperature opacity tables used by DSEP and most other stellar evolution programs give Rosseland-mean opacity,  $\kappa_R$ , along three dimensions: temperature, a density proxy  $R$  (Equation 8.2;  $T_6 = T \times 10^{-6}$ ,  $\rho$  is the mass density), and composition.

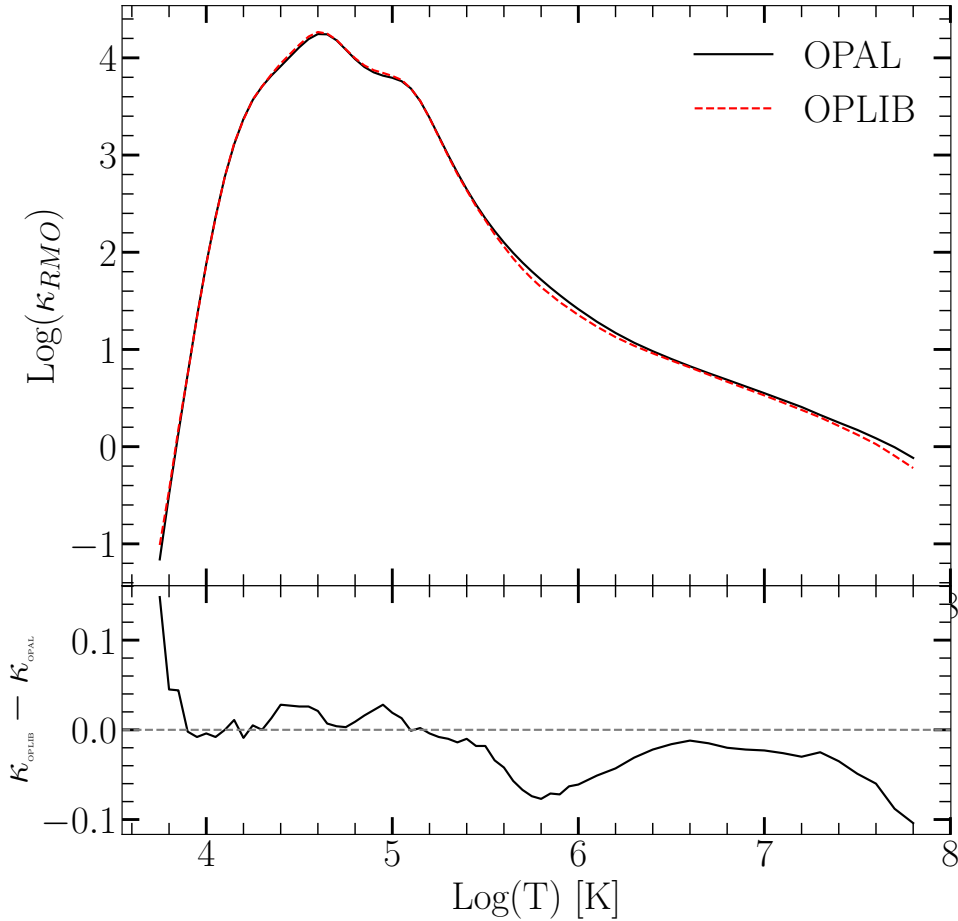


Figure 8.3: Rosseland mean opacity with the GS98 solar composition for both OPAL opacities and OPLIB opacities (top). Residuals between OPLIB opacities and OPAL opacities (bottom). These opacities are plotted at  $\log_{10}(R) = -0.5$ ,  $X = 0.7$ , and  $Z = 0.02$ .  $\log_{10}(R) = -0.5$  approximates much of the interior a  $0.35 M_\odot$  model. Note how the OPLIB opacities are systematically lower than the OPAL opacities for temperatures above  $10^{5.2}$  K.

$$R = \frac{\rho}{T_6^3} \quad (8.2)$$

OPLIB tables may be queried from a web interface<sup>1</sup>; however, OPLIB opacities are parametrized using mass-density and temperature instead of  $R$  and temperature. It is most efficient for us to convert these tables to the OPAL format instead of modifying DSEP to use the OPLIB format directly. In order to generate many tables easily and quickly we develop a web scraper (`pyTOPSScrape`, ?) which can automatically retrieve all the tables needed to build an opacity table in the OPAL format. `pyTOPSScrape`<sup>2</sup> has been released under the permissive MIT license with the consent of the Los Alamos T-1 group. For a detailed discussion of how the web scraper works and how OPLIB tables are transformed into a format DSEP can use see Appendices 8.4 & 8.5.

### 8.3.2 Solar Calibrated Stellar Models

In order to validate the OPLIB opacities, we generate a solar calibrated stellar model (SCSM) using these new tables. We first manually calibrate the surface Z/X abundance to within one part in 100 of the solar value (Grevesse & Sauval, 1998, Z/X=0.23). Subsequently, we allow both the convective mixing length parameter,  $\alpha_{ML}$ , and the initial Hydrogen mass fraction,  $X$ , to vary simultaneously, minimizing the difference, to within one part in  $10^5$ , between resultant models' final radius and luminosity to those of the sun. Finally, we confirm that the model's surface Z/X abundance is still within one part in 100 of the solar value.

Solar calibrated stellar models evolved using GS98 OPAL and OPLIB opacity tables (Figure 8.4) differ  $\sim 0.5\%$  in the SCSM hydrogen mass fractions and  $\sim 1.5\%$  in the SCSM convective mixing length parameters (Table 8.1). While the two evolutionary tracks are very similar, note that the OPLIB SCSM's luminosity is systematically lower past the solar age. While at the solar age the OPLIB SCSM luminosity is effectively the same as the OPAL SCSM. This luminosity difference between OPAL and OPLIB based models is not inconsistent with expectations given the more shallow

---

<sup>1</sup><https://aphysics2.lanl.gov/apps/>

<sup>2</sup><https://github.com/tboudreaux/pytopsscrape>

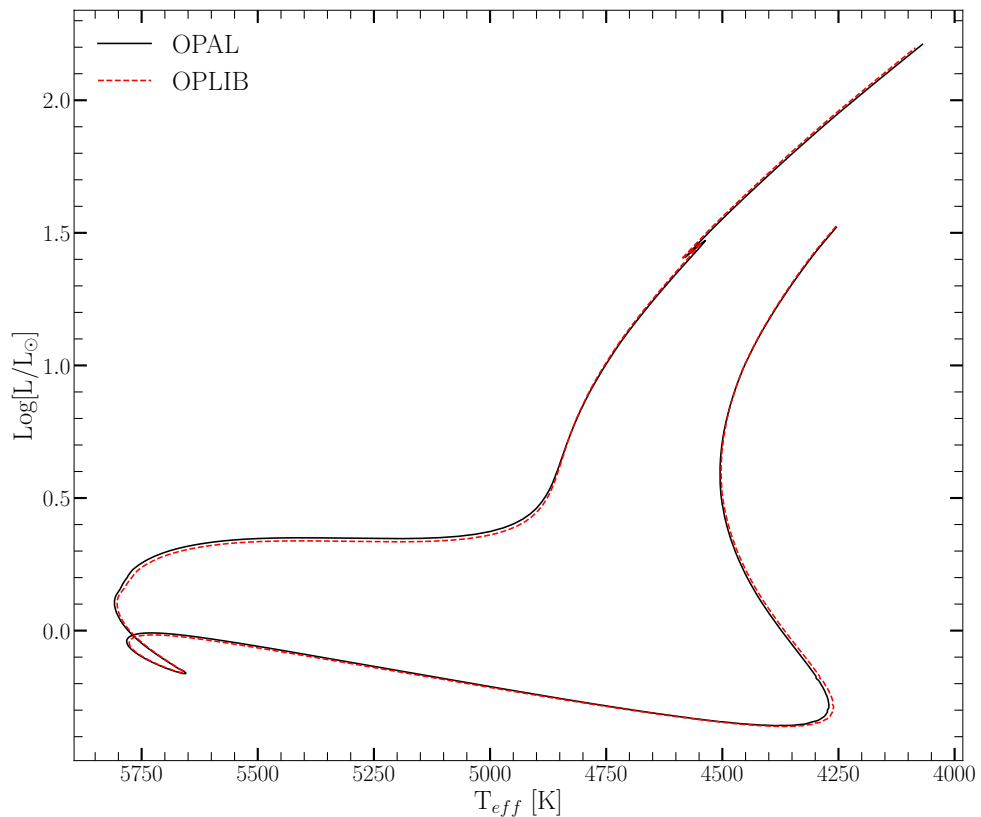


Figure 8.4: HR Diagram for the two SCSMs, OPAL and OPLIB. OPLIB is shown as a red dashed line.

Model	$X$	$\alpha_{ML}$
OPAL	0.7066	1.9333
OPLIB	0.7107	1.9629

Table 8.1: Optimized parameters for SCSMs evolved using OPAL and OPLIB high temperature opacity tables.

radiative temperature gradient resulting from the lower OPLIB opacities

## 8.4 pyTOPSScrape

`pyTOPSScrape` provides an easy to use command line and python interface for the OPLIB opacity tables accessed through the TOPS web form. Extensive documentation of both the command line and programmatic interfaces is linked in the version controlled repository. However, here we provide a brief, illustrative, example of potential use.

Assuming `pyTOPSScrape` has been installed and given some working directory which contains a file describing a base composition (“comp.dat”) and another file containing a list of rescalings of that base composition (“rescalings.dat”) (both of these file formats are described in detail in the documentation), one can query OPLIB opacity tables and convert them to a form mimicking that of type 1 OPAL high temperature opacity tables using the following shell command.

```
$ generateTOPStables comp.dat rescalings.dat -d ./TOPSCache -o out.opac -j 20
```

For further examples of `pyTOPSScrape` please visit the repository.

## 8.5 Interpolating $\rho \rightarrow \mathbf{R}$

OPLIB parameterizes  $\kappa_R$  as a function of mass density, temperature in keV, and composition. Type 1 OPAL high temperature opacity tables, which DSEP and many other stellar evolution programs use, instead parameterizes opacity as a function of temperature in Kelvin,  $R$  (Equation 8.3), and composition. The conversion from

temperature in keV to Kelvin is trivial (Equation 8.4).

$$R = \frac{\rho}{T_6^3} \quad (8.3)$$

$$T_K = T_{keV} * 11604525.0061657 \quad (8.4)$$

However, the conversion from mass density to  $R$  is more involved. Because  $R$  is coupled with both mass density and temperature there is no way to directly convert tabulated values of opacity reported in the OPLIB tables to their equivalents in  $R$  space. The TOPS webform does allow for a density range to be specified at a specific temperature, which allows for  $R$  values to be directly specified. However, issuing a query to the TOPS webform for not just every composition in a Type 1 OPAL high temperature opacity table but also every temperature for every composition will increase the number of calls to the webform by a factor of 70. Therefore, instead of directly specifying  $R$  through the density range we choose to query tables over a broad temperature and density range and then rotate these tables, interpolating  $\kappa_R(\rho, T_{eff}) \rightarrow \kappa_R(R, T_{eff})$ .

To perform this rotation we use the `interp2d` function within `scipy`'s `interpolate` (?) module to construct a cubic bivariate B-spline ([DIERCKX, 1981](#)) interpolating function  $s$ , with a smoothing factor of 0, representing the surface  $\kappa_R(\rho, T_{eff})$ . For each  $R^i$  and  $T_{eff}^j$  reported in type 1 OPAL tables, we evaluate Equation 8.3 to find  $\rho^{ij} = \rho(T_{eff}^j, R^i)$ . Opacities in  $T_{eff}$ ,  $R$  space are then inferred as  $\kappa_R^{ij}(R^i, T_{eff}^j) = s(\rho^{ij}, T_{eff}^j)$ .

As first-order validation of this interpolation scheme we can perform a similar interpolation in the opposite direction, rotating the tables back to  $\kappa_R(\rho, T_{eff})$  and then comparing the initial, “raw”, opacities to those which have gone through the interpolations process. Figure 8.5 shows the fractional difference between the raw opacities and a set which have gone through this double interpolation. The red line denotes  $\log(R) = -0.79$  where models near the Jao Gap mass range will tend to sit for much of their radius. Along the  $\log(R) = -0.79$  line the mean fractional difference

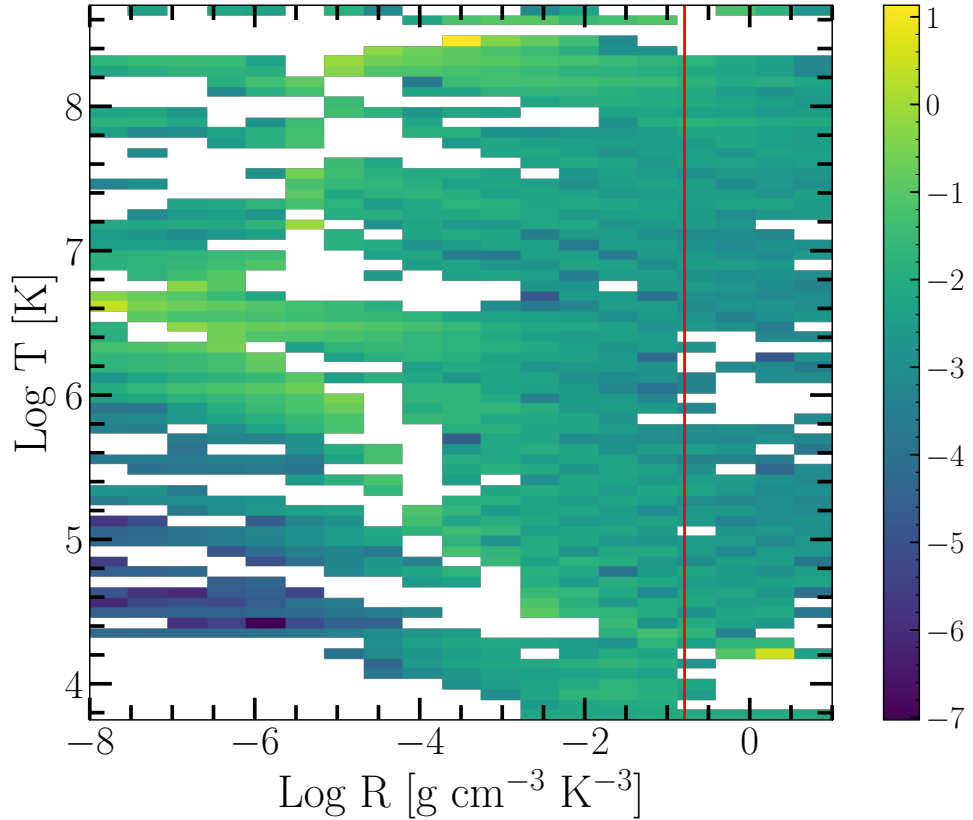


Figure 8.5: Log Fractional Difference between opacities in  $\kappa_R(\rho, T_{eff})$  space directly queried from the OPLIB web-form and those which have been interpolated into  $\log(R)$  space and back. Note that, due to the temperature grid of type 1 OPAL tables not aligning perfectly with the temperature grid OPLIB uses there may be edge effects where the interpolation is poorly constrained. The red line corresponds to  $\log(R) = -0.79$  where much of a stellar model's radius exists.

is  $\langle \delta \rangle = 0.005$  with an uncertainty of  $\sigma_{\langle \delta \rangle} = 0.013$ . One point of note is that, because the initial rotation into  $\log(R)$  space also reduces the domain of the opacity function, interpolation-edge effects which we avoid initially by extending the domain past what type 1 OPAL tables include cannot be avoided when interpolating back into  $\rho$  space.

## 8.6 Modeling

In order to model the Jao Gap we evolve two extremely finely sampled mass grids of models. One of these grids uses the OPAL high-temperature opacity tables while the other uses the OPLIB tables (Figure 8.6). Each grid evolves a model every  $0.00025 M_\odot$  from  $0.2$  to  $0.4 M_\odot$  and every  $0.005 M_\odot$  from  $0.4$  to  $0.8 M_\odot$ . All models in both grids

use a GS98 solar composition, the (1, 101, 0) `FreeEOS` (version 2.7) configuration, and 1000 year old pre-main sequence polytropic models, with polytropic index 1.5, as their initial conditions. We include gravitational settling in our models where elements are grouped together. Finally, we set a maximum allowed timestep of 50 million years to assure that we fully resolve the build of core  $^3\text{He}$  in gap stars.

Despite the alternative view of convection provided by [MacDonald & Gizis \(2018\)](#) discussed in Section 8.2, given that the mixing timescales in these low mass stars are so short (between  $10^7$ s and  $10^8$ s per [Jermyn et al., 2022](#), Figure 2 & Equation 39, which present the averaged velocity over the convection zone) instantaneous mixing is a valid approximation. Moreover, one principal motivation for a diffusive model of convective mixing has been to account for a deuterium concentration gradient which [Chabrier & Baraffe \(1997\)](#) identify will develop when the deuterium lifetime against proton capture is significantly shorter than the mixing timescale. However, the treatment of energy generation used by DSEP ([Bahcall et al., 2001](#)) avoids this issue by computing both the equilibrium deuterium abundance and luminosity of each shell individually, implicitly accounting for the overall luminosity discrepancy identified by [Chabrier & Baraffe](#).

Because in this work we are just interested in the location shift of the Gap as the opacity source varies, we do not model variations in composition. [Mansfield & Kroupa \(2021\)](#); [Jao & Feiden \(2020\)](#); [Feiden et al. \(2021\)](#) all look at the effect composition has on Jao Gap location. They find that as population metallicity increases so too does the mass range and consequently the magnitude of the Gap. From an extremely low metallicity population ( $Z=0.001$ ) to a population with a more solar like metallicity this shift in mass range can be up to  $0.05 M_{\odot}$  ([Mansfield & Kroupa, 2021](#)).

### 8.6.1 Population Synthesis

In order to compare the Gap to observations we use in house population synthesis code. We empirically calibrate the relation between G, BP, and RP magnitudes and their uncertainties along with the parallax/G magnitude uncertainty relation using the Gaia Catalogue of Nearby Stars (GCNS, [Gaia Collaboration et al., 2021](#)) and

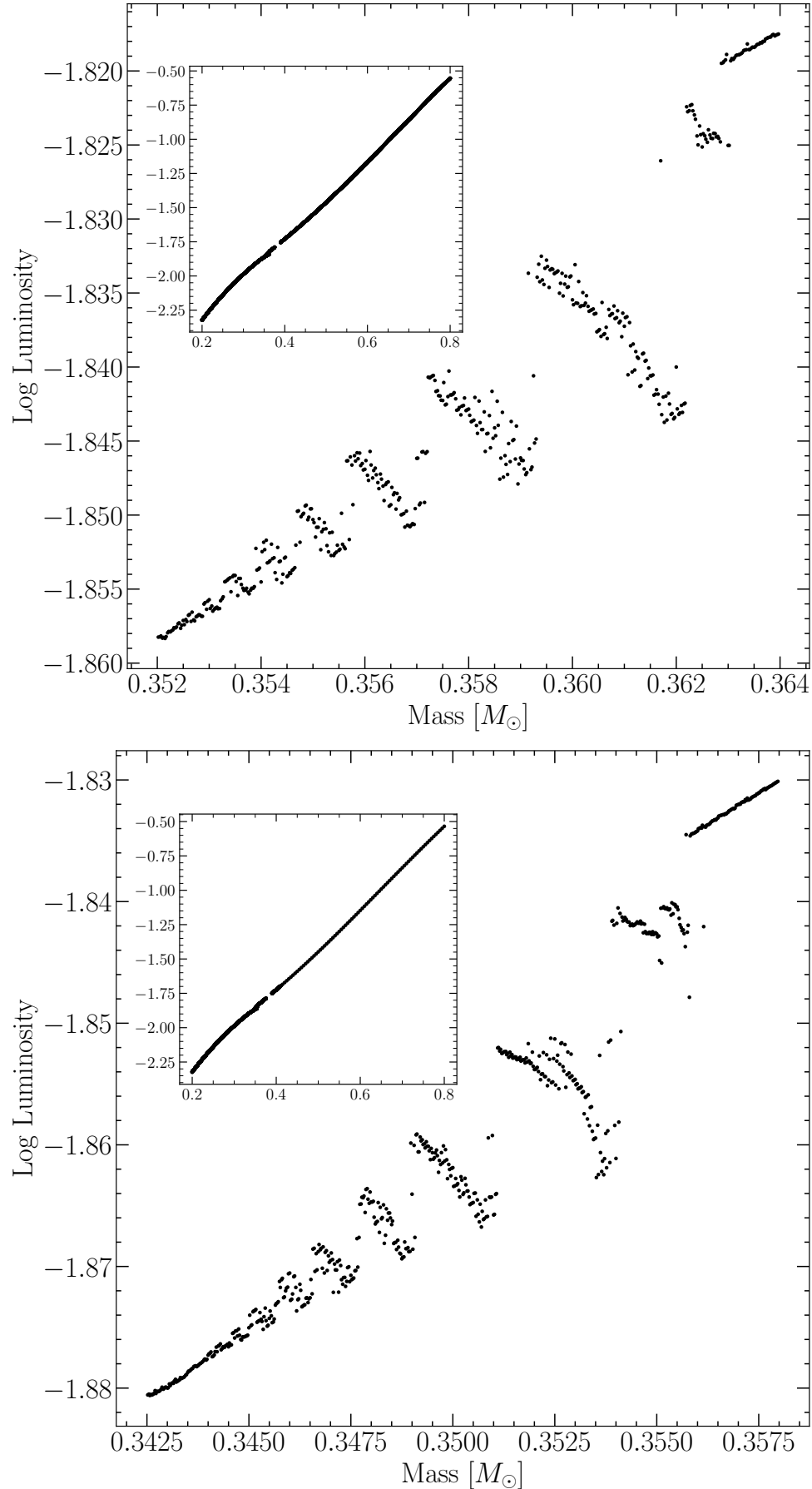


Figure 8.6: Mass-luminosity relation at 7 Gyrs for models evolved using OPAL opacity tables (top) and those evolved using OPLIB opacity tables (bottom). Note the lower value of the OPLIB C parameter.

Equations 8.5 & 8.6.  $M_g$  is the Gaia G magnitude while  $M_i$  is the magnitude in the  $i^{\text{th}}$  band, G, BP, or RP. The coefficients  $a$ ,  $b$ , and  $c$  determined using a non-linear least squares fitting routine. Equation 8.5 then models the relation between G magnitude and parallax uncertainty while Equation 8.6 models the relation between each magnitude and its uncertainty.

$$\sigma_{plx}(M_g) = ae^{bM_g} + c \quad (8.5)$$

$$\sigma_i(M_i) = ae^{M_i - b} + c \quad (8.6)$$

The full series of steps in our population synthesis code are:

1. Sample from a [Sollima \(2019\)](#) ( $0.25M_\odot < M < 1M_\odot$ ,  $\alpha = -1.34 \pm 0.07$ ) IMF to determine synthetic star mass.
2. Find the closest model above and below the synthetic star, linearly interpolate these models'  $T_{\text{eff}}$ ,  $\log(g)$ , and  $\log(L)$  to those at the synthetic star mass.
3. Convert synthetic star  $g$ ,  $T_{\text{eff}}$ , and  $\log(L)$  to Gaia G, BP, and RP magnitudes using the Gaia (E)DR3 bolometric corrections ([Creevey et al., 2022](#)) along with code obtained thorough personal communication with Aaron Dotter ([Choi et al., 2016](#)).
4. Sample from the GCNS parallax distribution (Figure 8.7), limited to stars within the BP-RP color range of  $2.3 - 2.9$ , to assign synthetic star a “true” parallax.
5. Use the true parallax to find an apparent magnitude for each filter.
6. Evaluate the empirical calibration given in Equation 8.5 to find an associated parallax uncertainty. Then sample from a normal distribution with a standard deviation equal to that uncertainty to adjust the true parallax resulting in an “observed” parallax.

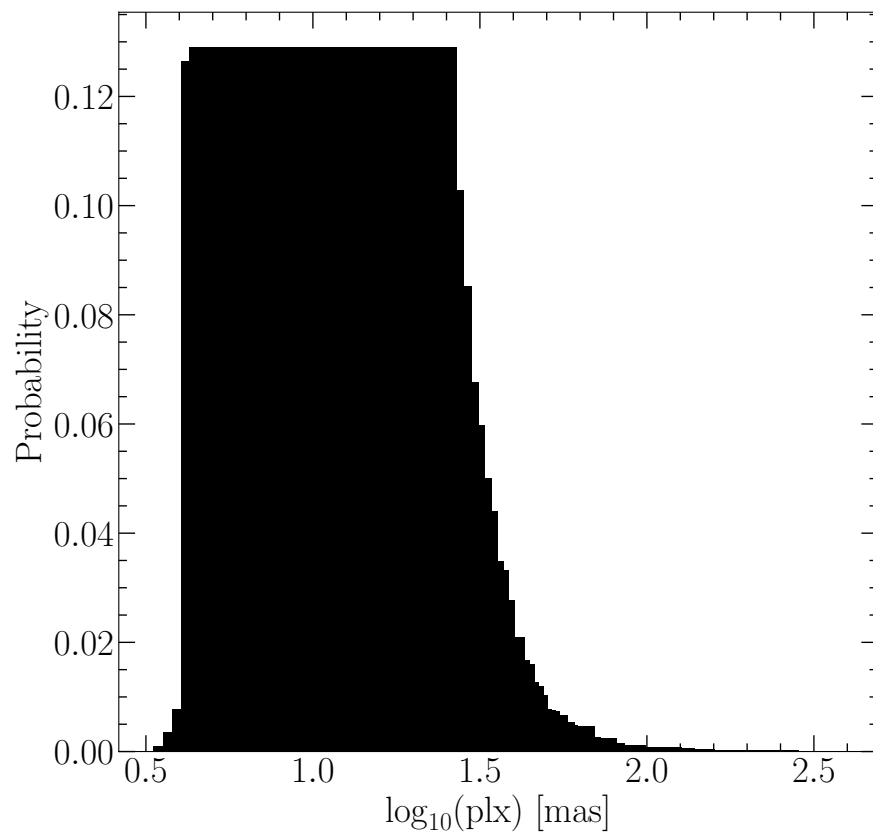


Figure 8.7: Probability distribution sampled when assigning true parallaxes to synthetic stars. This distribution is built from the GCNS and includes all stars with BP-RP colors between 2.3 and 2.9, the same color range of the Jao Gap.

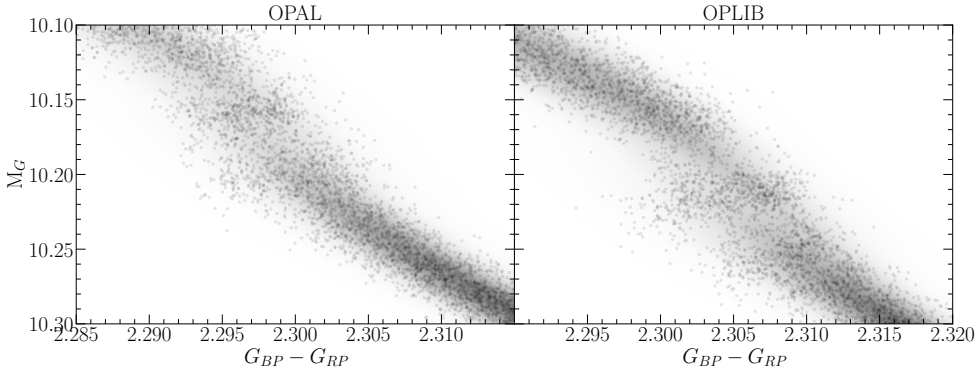


Figure 8.8: Population synthesis results for models evolved with OPAL (left) and models evolved with OPLIB (right). A Gaussian kernel-density estimate has been overlaid to better highlight the density variations.

7. Use the “observed” parallax and the apparent magnitude to find an “observed” magnitude.
8. Fit the empirical calibration given in Equation 8.6 to the GCNS and evaluate it to give a magnitude uncertainty scale in each band.
9. Adjust each magnitude by an amount sampled from a normal distribution with a standard deviation of the magnitude uncertainty scale found in the previous step.

This method then incorporates both photometric and astrometric uncertainties into our population synthesis. An example 7 Gyr old synthetic populations using OPAL and OPLIB opacities are presented in Figure 8.8.

### 8.6.2 Mixing Length Dependence

In order to test the sensitivity of Gap properties to mixing length we evolve three separate sets OPLIB of models. The first uses a GS98 solar calibrated mixing length, the second uses a mixing length of 1.5, and the third uses a mixing length of 1.0.

We find a clear inverse correlation between mixing length parameter used and the magnitude of the Jao Gap Figures 8.9 & 8.10 ( $\mu_G \propto -1.5\alpha_{ML}$ , where  $\mu_G$  is the mean magnitude of the Gap). This is somewhat surprising given the long established view that the mixing length parameter is of little relevance in fully convective

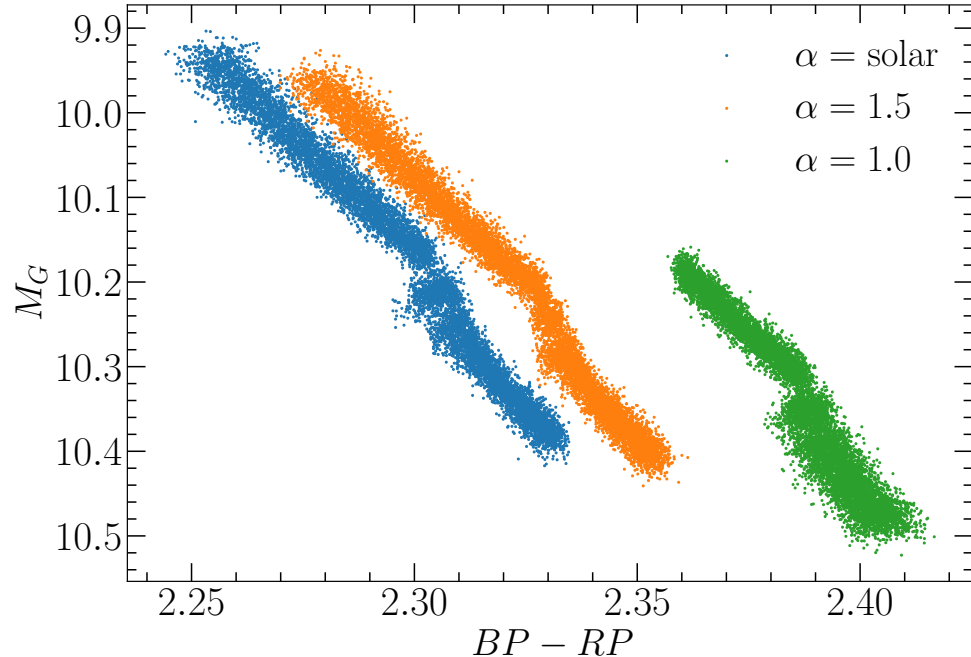


Figure 8.9: CMD showing OPLIB populations (from left to right) A, B, and C.

stars (Baraffe et al., 1997). We find an approximate 0.3 magnitude shift in both the color and magnitude comparing a solar calibrated mixing length to a mixing length of 1.5, despite only a 16K difference in effective temperature at 7Gyr between two 0.3 solar mass models. The slight temperature differences between these models are attributable to the steeper adiabatic temperature gradients just below the atmosphere in the solar calibrated mixing length model compared to the  $\alpha_{ML} = 1.5$  model ( $\nabla_{ad,solar} - \nabla_{ad,1.5} \approx 0.05$ ). Despite this relatively small temperature variance, the large magnitude difference is expected due to the extreme sensitivity of the bolometric corrections on effective temperature at these low temperatures. The mixing length then provides a free parameter which may be used to shift the gap location in order to better match observations without having a major impact on the effective temperature of models. Moreover, recent work indicates that using a solar calibrated mixing length is not appropriate for all stars (e.g. Trampedach et al., 2014; Joyce & Chaboyer, 2018).

Given the variability of gap location with mixing length, it is possible that a better fit to the gap location may be achieved through adjustment of the convective mixing

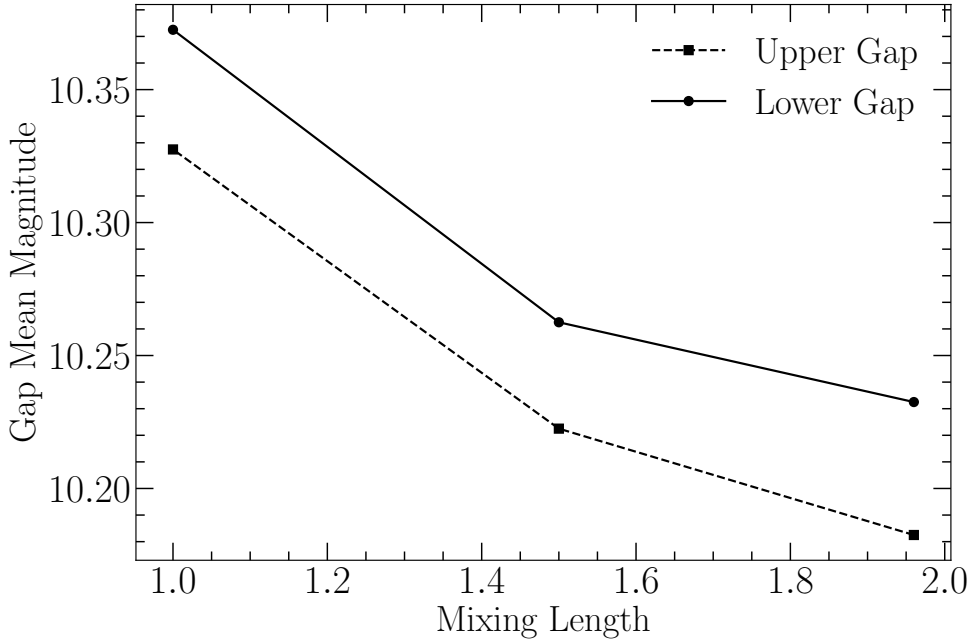


Figure 8.10: Location of the two identified paucities of stars in OPLIB synthetic populations as a function of the mixing length used.

length parameter. However, calibrations of the mixing length for stars other than the sun have focused on stars with effective temperature at or above that of the sun and there are no current calibrations of the mixing length parameter for M dwarfs. Moreover, there are additional uncertainties when comparing the predicted gap location to the measured gap location, such as those in the conversion from effective temperature, surface gravity, and luminosity to color, which must be considered if the mixing length is to be used as a gap location free parameter. Given the dangers of freely adjustable parameters and the lack of an a priori expectation for what the convective mixing parameter should be for the population of M Dwarfs in the Gaia DR2 and EDR3 CMD any attempt to use the Jao Gap magnitude to calibrate a mixing length value must be done with caution, and take into account the other uncertainties in the stellar models which could affect the Jao Gap magnitude.

## 8.7 Results

We quantify the Jao Gap location along the magnitude (Table 8.2) axis by subsampling our synthetic populations, finding the linear number density along the mag-

Model	Location	Prominence	Width
OPAL 1	10.138	0.593	0.027
OPAL 2	10.183	0.529	0.023
OPLIB 1	10.188	0.724	0.032
OPLIB 2	10.233	0.386	0.027

Table 8.2: Locations identified as potential Gaps.

nitude axis of each sub-sample, averaging these linear number densities, and extracting any peaks above a prominence threshold of 0.1 as potential magnitudes of the Jao Gap (Figure 8.11). Gap widths are measured at 50% the height of the peak prominence. We use the python package `scipy` (?) to both identify peaks and measure their widths.

In both OPAL and OPLIB synthetic populations our Gap identification method finds two gaps above the prominence threshold. The identification of more than one gap is not inconsistent with the mass-luminosity relation seen in the grids we evolve. As noise is injected into a synthetic population smaller features will be smeared out while larger ones will tend to persist. The mass-luminosity relations shown in Figure 8.6 make it clear that there are: (1), multiple gaps due to stars of different masses undergoing convective mixing events at different ages, and (2), the gaps decrease in width moving to lower masses / redder. Therefore, the multiple gaps we identify are attributable to the two bluest gaps being wide enough to not smear out with noise. In fact, if we lower the prominence threshold just slightly from 0.1 to 0.09 we detect a third gap in both the OPAL and OPLIB datasets where one would be expected.

Previous modeling efforts (e.g. [Feiden et al., 2021](#)) have not identified multiple gaps. This is likely due to two reasons: (1), previous studies have allowed metallicity to vary across their model grids, further smearing the gaps out, and (2), previous studies have used more coarse underlying mass grids, obscuring features smaller than their mass step. While this dual-gap structure has not been seen in models before, a more complex gap structure is not totally unprecedented as [Jao & Feiden \(2021\)](#) identifies an additional under-dense region below the primary gap in EDR3 data. As part of a follow up series of papers, we are conducting further work to incorporate metallicity variations while still using the finer mass sampling presented here.

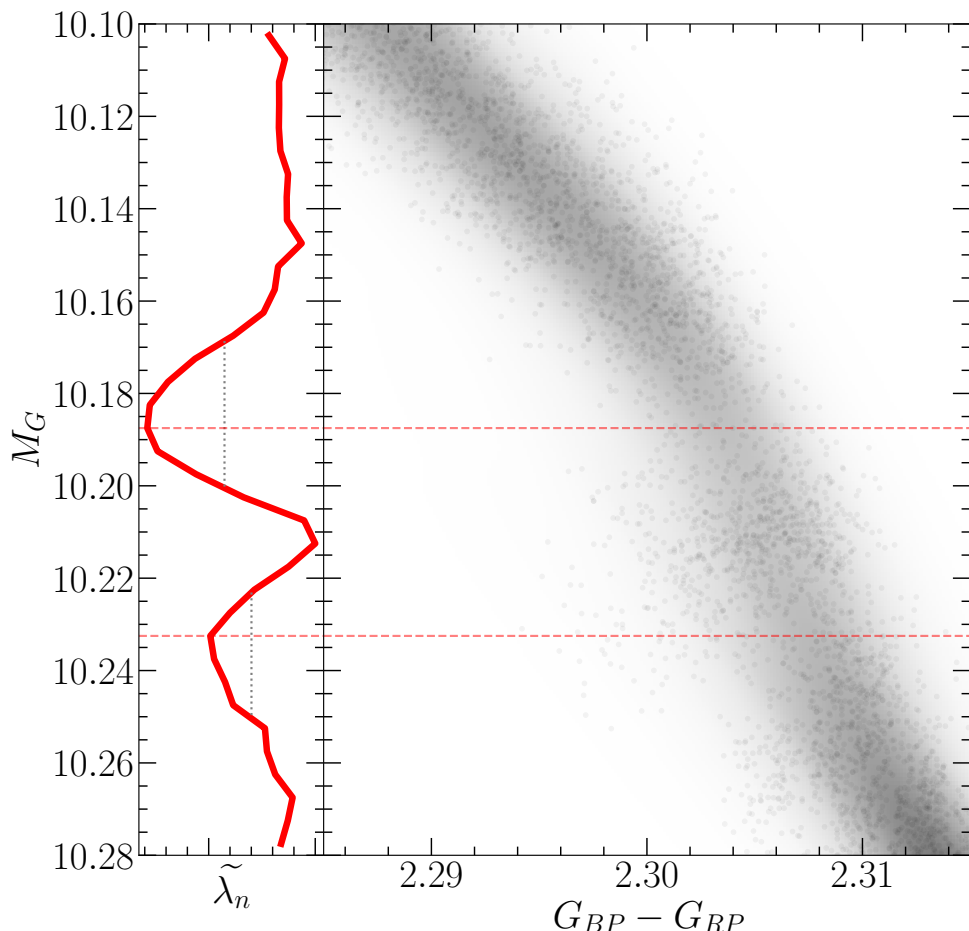
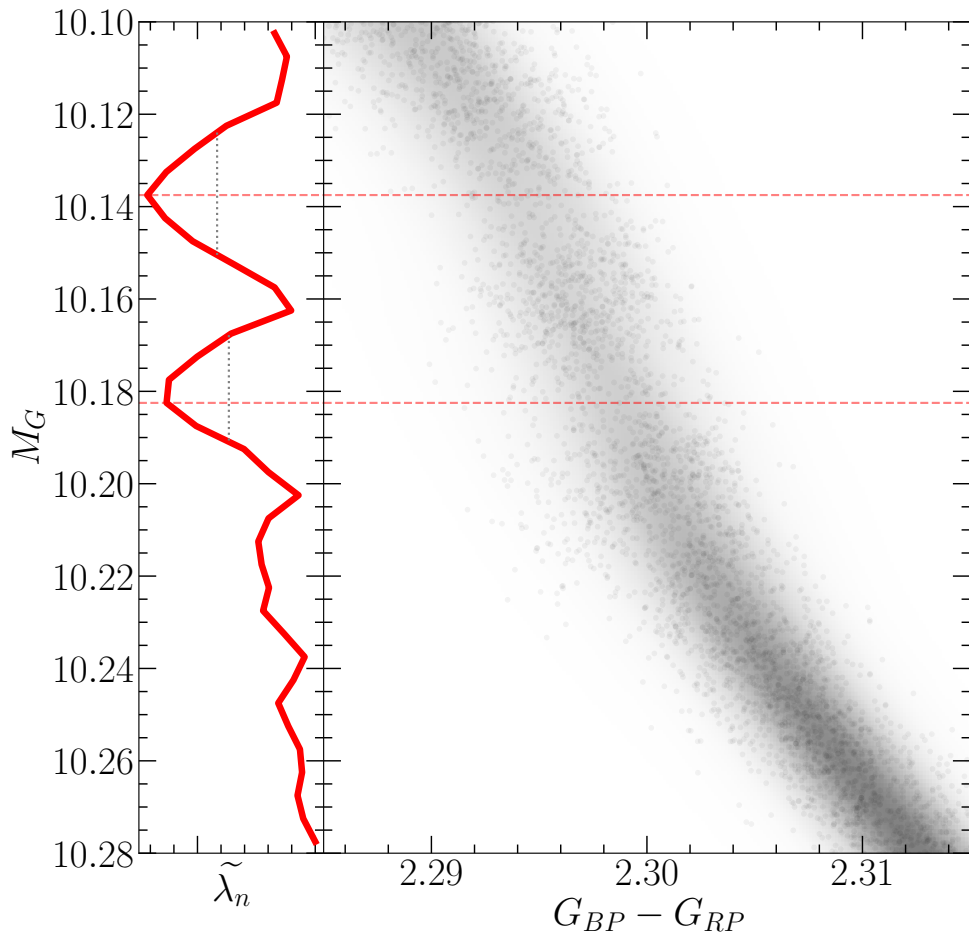
The mean gap location of the OPLIB population is at a fainter magnitude than the mean gap location of the OPAL population. Consequently, in the OPLIB sample the convective mixing events which drive the kissing instability begin happening at lower masses (i.e. the convective transition mass decreases). A lower mass range will naturally result in a fainter mean gap magnitude.

Mixing events at lower masses in OPLIB models are attributable to the radially thicker, at the same mass, radiative zones (Figure 8.12). This thicker radiative zone will take more time to break down and is characteristic of OPLIB models as of a result of their slightly lower opacities. A lower opacity fluid will have a more shallow radiative temperature gradient than a higher opacity fluid; however, as the adiabatic temperature gradient remains essentially unchanged as a function of radius, a larger interior radius of the model will remain unstable to radiation. This thicker radiative zone will increase the time it takes the core convective zone to meet up with convective envelope meaning that lower mass models can sustain a radiative zone for longer than they could otherwise; thus; lower opacities push the convective transition mass down. We can additionally see this longer lived radiative zone in the core  $^3\text{He}$  mass fraction, in which OPLIB models reach much higher concentrations — at approximately the same growth rate — for the same mass as OPAL models do (Figure 8.13).

The most precise published Gap location comes from [Jao & Feiden \(2020\)](#) who use EDR3 to locate the Gap at  $M_G \sim 10.3$ , we identify the Gap at a similar location in the GCNS data. The Gap in populations evolved using OPLIB tables is closer to this measurement than it is in populations evolved using OPAL tables (Table 8.2). It should be noted that the exact location of the observed Gap is poorly captured by a single value as the Gap visibly compresses across the width of the main-sequence, wider on the blue edge and narrower on the red edge such that the observed Gap has downward facing a wedge shape (Figure 8.1). This wedge shape is not successfully reproduced by either any current models or the modeling we perform here. We elect then to specify the Gap location where this wedge is at its narrowest, on the red edge of the main sequence.

The Gaps identified in our modeling have widths of approximately 0.03 magni-

tudes, while the shift from OPAL to OPLIB opacities is 0.05 magnitudes. With the prior that the Gaps clearly shift before noise is injected we know that this shift is real. However, the shift magnitude and Gap width are of approximately the same size in our synthetic populations. Moreover, Feiden et al. (2021) identify that the shift in the modeled Gap mass from  $[Fe/H] = 0$  to  $[Fe/H] = +0.5$  is  $0.04M_{\odot}$ , whereas we only see an approximate  $0.01 M_{\odot}$  shift between OPAL and OPLIB models. Therefore, the Gap location will likely not provide a usable constraint on the opacity source.



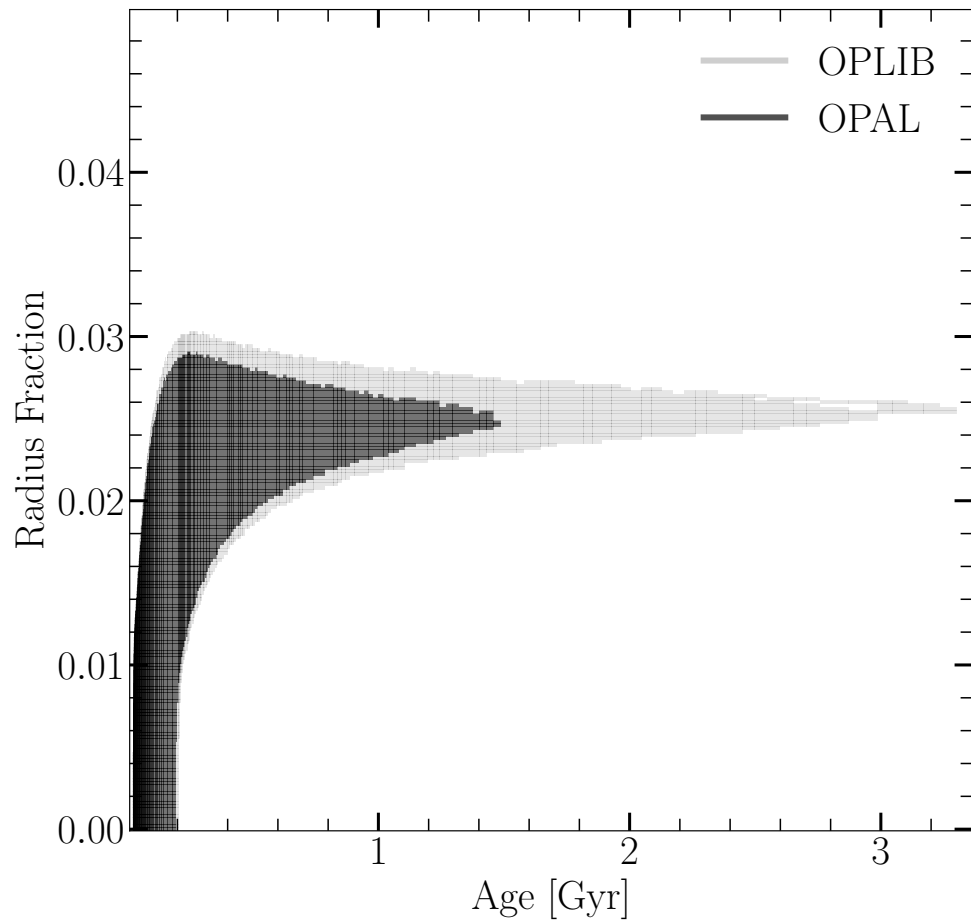


Figure 8.12: Portions of  $0.3526 M_{\odot}$  OPAL and OPLIB stellar models showing the interior shells which are radiative (black region). Note that for clarity only one convective mixing event from each model is shown. Note how the radiative zone in the OPLIB model is larger.

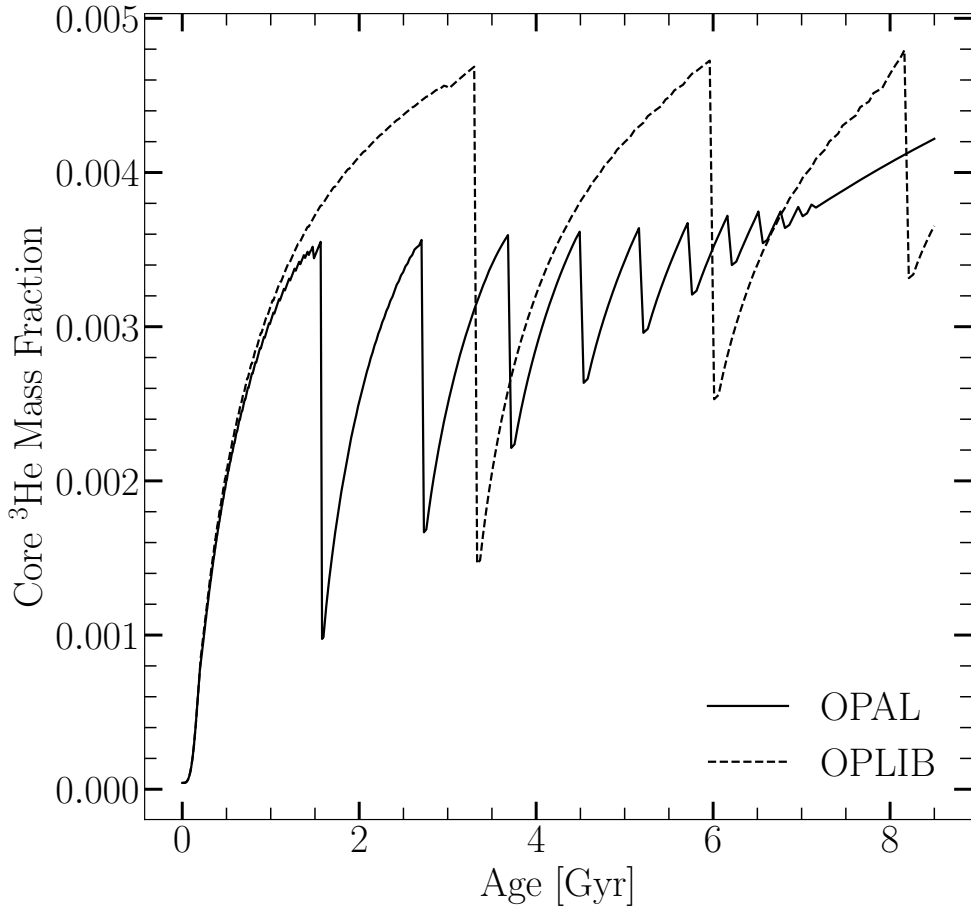


Figure 8.13: Core  ${}^3\text{He}$  mass fraction for  $0.3526 M_{\odot}$  models evolved with OPAL and OPLIB (within the Jao Gap's mass range for both). Note how the OPLIB model's core  ${}^3\text{He}$  mass fraction grows at approximately the same rate as the OPAL model's but continues uninterrupted for longer.

# Chapter 9

## Jao Gap connection to Magnetism

### 9.1 INTRODUCTION

The initial mass requirements of molecular clouds collapsing to form stars results in a strong bias towards lower masses and later spectral classes during star formation. Partly as a result of this bias and partly as a result of their extremely long main-sequence lifetimes, M Dwarfs make up approximately 70 percent of all stars in the galaxy ([Winters et al., 2019](#)). Moreover, many planet search campaigns have focused on M Dwarfs due to the relative ease of detecting small planets in their habitable zones (e.g. [Nutzman & Charbonneau, 2008](#)). M Dwarfs then represent both a key component of the galactic stellar population as well as the most numerous possible set of stars which may host habitable exoplanets. Given this key location M Dwarfs occupy in modern astronomy it is important to have a thorough understanding of their structure and evolution.

[Jao et al. \(2018\)](#) discovered a novel feature in the Gaia Data Release 2 (DR2)  $G_{BP} - G_{RP}$  color-magnitude-diagram. Around  $M_G = 10$  there is an approximately 17 percent decrease in stellar density of the sample of stars [Jao et al. \(2018\)](#) considered. Subsequently, this has become known as either the Jao Gap, or Gaia M Dwarf Gap. Following the initial detection of the Gap in DR2 the Gap has also potentially been observed in 2MASS ([Skrutskie et al., 2006](#); [Jao et al., 2018](#)); however, the significance of this detection is quite weak and it relies on the prior of the Gap's location from Gaia data. The Gap is also present in Gaia Early Data Release 3 (EDR3) ([Jao &](#)

(Feiden, 2021). These EDR3 and 2MASS data sets then indicate that this feature is not a bias inherent to DR2.

The Gap is generally attributed to convective instabilities in the cores of stars straddling the fully convective transition mass (0.3 - 0.35 M<sub>☉</sub>) **known as convective kissing instabilities** (Baraffe & Chabrier, 2018). These instabilities interrupt the normal, slow, main sequence luminosity evolution of a star and result in luminosities lower than expected from the main sequence mass-luminosity relation (Jao & Feiden, 2020).

The Jao Gap, inherently a feature of M Dwarf populations, provides an enticing and unique view into the interior physics of these stars (Feiden et al., 2021). This is especially important as, unlike more massive stars, M Dwarf seismology is infeasible due to the short periods and extremely small magnitudes which both radial and low-order low-degree non-radial seismic waves are predicted to have in such low mass stars (Rodríguez-López, 2019). The Jao Gap therefore provides one of the only current methods to probe the interior physics of M Dwarfs.

The magnetic activity of M dwarfs is of particular interest due to the theorised links between habitability and the magnetic environment which a planet resides within (e.g. ???). M dwarfs are known to be more magnetically active than earlier type stars (???) while simultaneously this same high activity calls into question the canonical magnetic dynamo believed to drive the magnetic field of solar-like stars (the  $\alpha\Omega$  dynamo) (?). One primary challenge which M dwarfs pose is that stars less than approximately 0.35 M<sub>☉</sub> are composed of a single convective region. This denies any dynamo model differential rotation between adjacent levels within the star. Alternative dynamo models have been proposed, such as the  $\alpha^2$  dynamo along with modifications to the  $\alpha\Omega$  dynamo which may be predictive of M dwarf magnetic fields (???).

Despite this work, very few studies have dived specifically into the magnetic field of M dwarfs at or near the convective transition region . This is not surprising as that only spans approximately a 0.2 magnitude region in the Gaia BP-RP color magnitude diagram and is therefore populated by a relatively small sample of stars.

Jao et al. (2023) identify the Jao Gap as a strong discontinuity point for magnetic

activity in M dwarfs. Two primary observations from their work are that the Gap serves as a boundary where very few active stars, in their sample of 640 M dwarfs, exist below the Gap and that the overall downward trend of activity moving to fainter magnitudes is anomalously high in within the 0.2 mag range of the Gap. [Jao et al.](#) Figures 3 and 13 make this paucity in H $\alpha$  emission particularly clear. Based on previous work from ??? the authors propose that the mechanism resulting in the reduced fraction of active stars within the Gap is that as the radiative zone dissipates due to core expansion, angular momentum from the outer convective zone is dumped into the core resulting in a faster spin down than would otherwise be possible. Effectively the core of the star acts as a sink, reducing the amount of angular momentum which needs to be lost by magnetic braking for the outer convective region to reach the same angular velocity. Given that H $\alpha$  emission is strongly coupled magnetic activity in the upper chromosphere ([Newton et al., 2016](#); ?) and that a star's angular velocity is a primary factor in its magnetic activity, a faster spin down will serve to more quickly dampen H $\alpha$  activity.

In addition to H $\alpha$  the Calcium Fraunhauser lines may be used to trace the magnetic activity of a star. These lines originate from magnetic heating of the lower chromosphere driven by magnetic shear stresses within the star. Both [Perdelwitz et al. \(2021\)](#) and [Boudreux et al. \(2022\)](#) present calcium emission measurements for stars spanning the Jao Gap. In this paper we search for similar trends in the Ca II H& K emission as [Jao et al.](#) see in the H $\alpha$  emission. In Section 10.4 we investigate the empirical star-to-star variability in emission and quantify if this could be due to noise or sample bias; in Section 9.3 we present a simplified toy model which shows that the mixing events characteristic of convective kissing instabilities could lead to increased star-to-star variability in activity as is seen empirically.

## 9.2 Correlation

Using Ca II H&K emission data from [Perdelwitz et al. \(2021\)](#) and [Boudreux et al. \(2022\)](#) (quantified using the  $R'_{HK}$  metric [Middelkoop, 1982](#); [Rutten, 1984](#)) we investigate the correlation between the Jao Gap magnitude and stellar magnetic activity. We

are more statistically limited here than past authors have been due to the requirement for high resolution spectroscopic data when measuring Calcium emission.

The merged dataset is presented in Figure 9.1. **The sample overlap between Perdelwitz et al. (2021) and Boudreux et al. (2022) is small (only consisting of five targets). For those five targets there is an approximately 1.5 percent average difference between measured  $\log(R'_{HK})$  values with measurements from Boudreux et al. biased to be slightly more negative than those from Perdelwitz et al.**

There is a visual discontinuity in **the spread of stellar activity** below the Jao Gap magnitude. **Further discussion of why there may be disagreement between the observed magnitude of the gap and the discontinuity which we identify may be found in Section 9.2.1.** In order to quantify the significance of this discontinuity we measure the false alarm probability of the change in standard deviation.

First we split the merged dataset into bins with a width of 0.5 mag. In each bin we measure the standard deviation about the mean of the data. The results of this are shown in Figure 9.1 (bottom). In order to measure the false alarm probability of this discontinuity we first resample the merged calcium emission data based on the associated uncertainties for each datum as presented in their respective publications. Then, for each of these “resample trials” we measure the probability that a change in the standard deviation of the size seen would happen purely due to noise. Results of this test are show in in Figure 9.2.

This rapid increase star-to-star variability would only arise due purely to noise  $0.3 \pm 0.08$  percent of the time and is therefore likely either a true effect or an alias of some sample bias.

If the observed increase in variability is not due to a sample bias and rather is a physically driven effect then there is an obvious similarity between these findings and those of Jao et al. (2023). Specifically we find a increase in variability below the magnitude of the Gap. Moreover, this variability increase is primarily driven by an increase in the number of low activity stars (as opposed to an increase in the number of

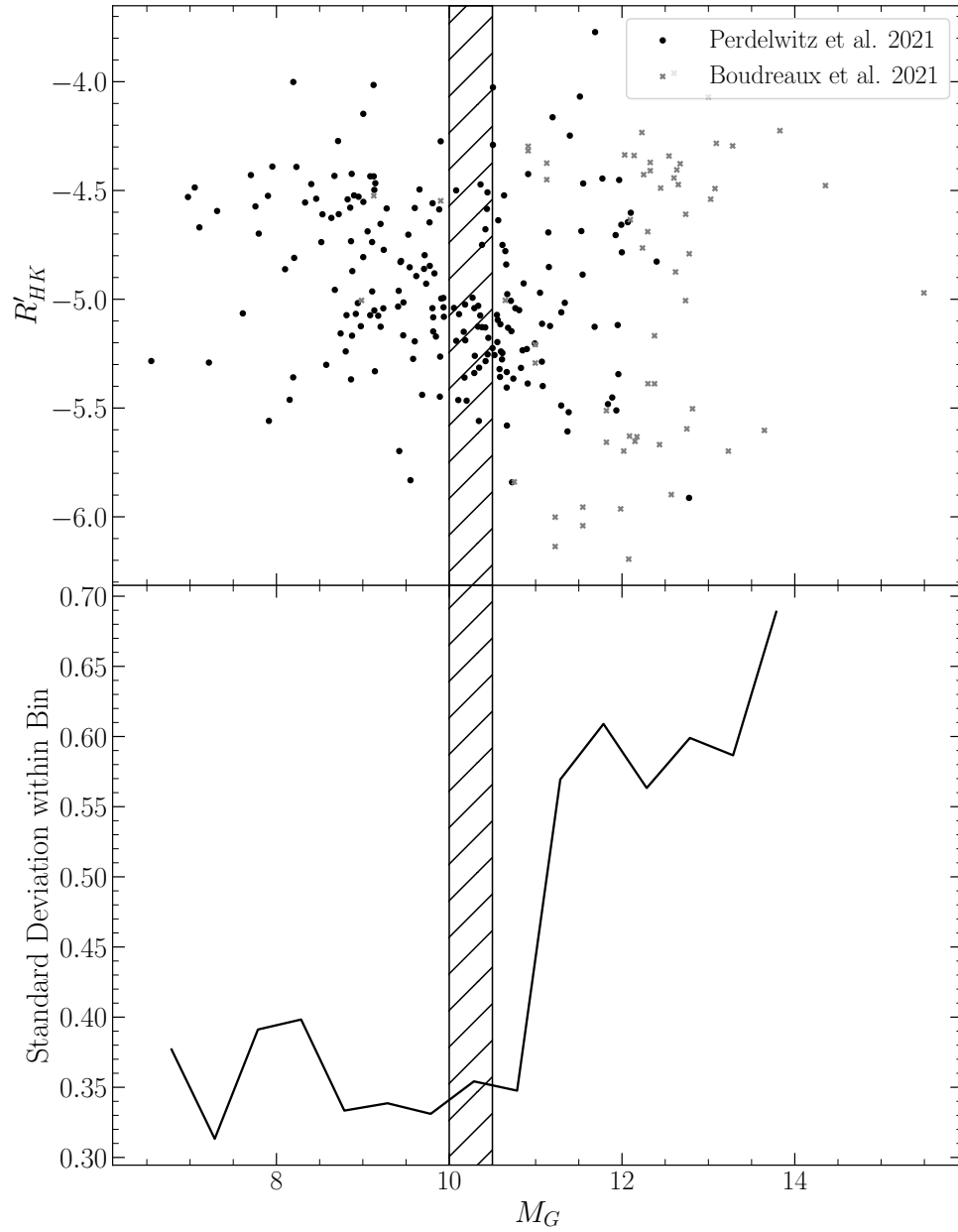


Figure 9.1: Merged Dataset from [Perdelwitz et al. \(2021\)](#); [Boudreux et al. \(2022\)](#). Note the increase in the spread of  $R'_{HK}$  around the Jao Gap Magnitude (top). Standard deviation of Calcium emission data within each bin. Note the discontinuity near the Jao Gap Magnitude (bottom). The location of the Gap as identified in literature is shown by the hatched region ( $\sim 10\text{--}10.5 M_G$ ). Potential explanations for the disagreement in magnitude are discussed in detail in Section 9.2.1.

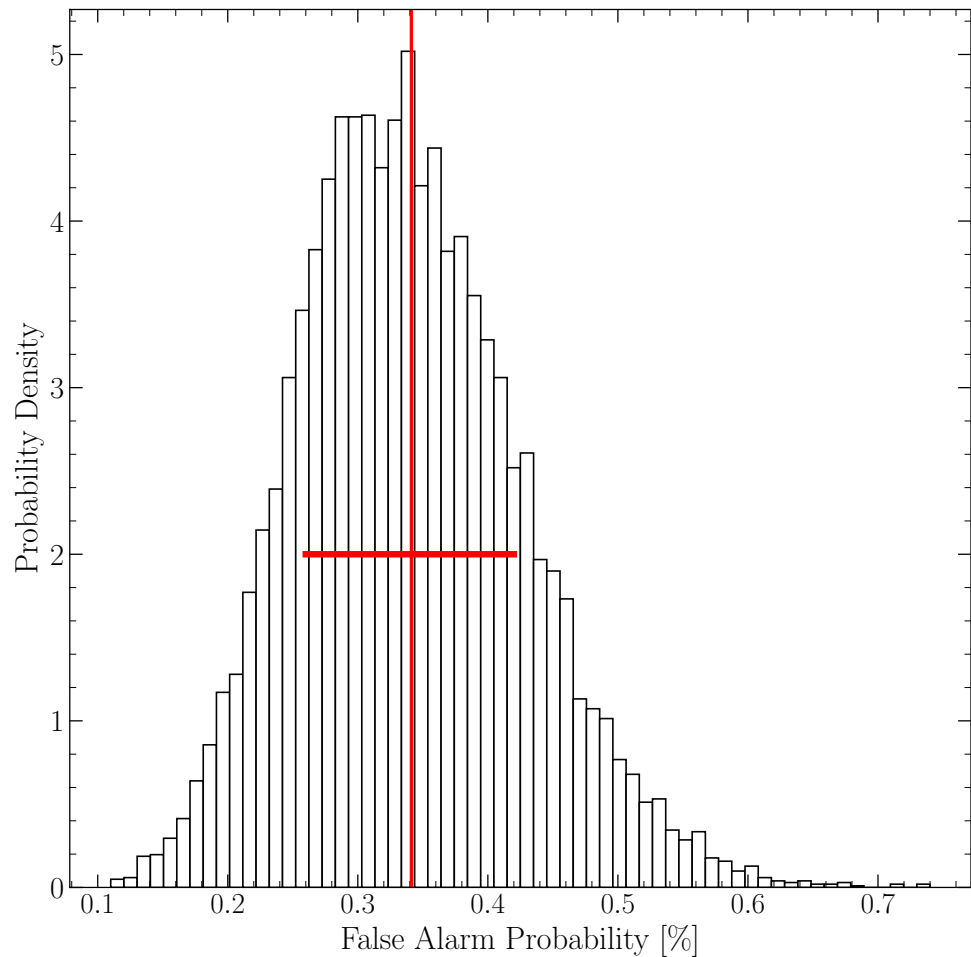


Figure 9.2: Probability distribution of the false alarm probability for the discontinuity seen in Figure 9.1. The mean of this distribution is  $0.341\% \pm 0.08$ .

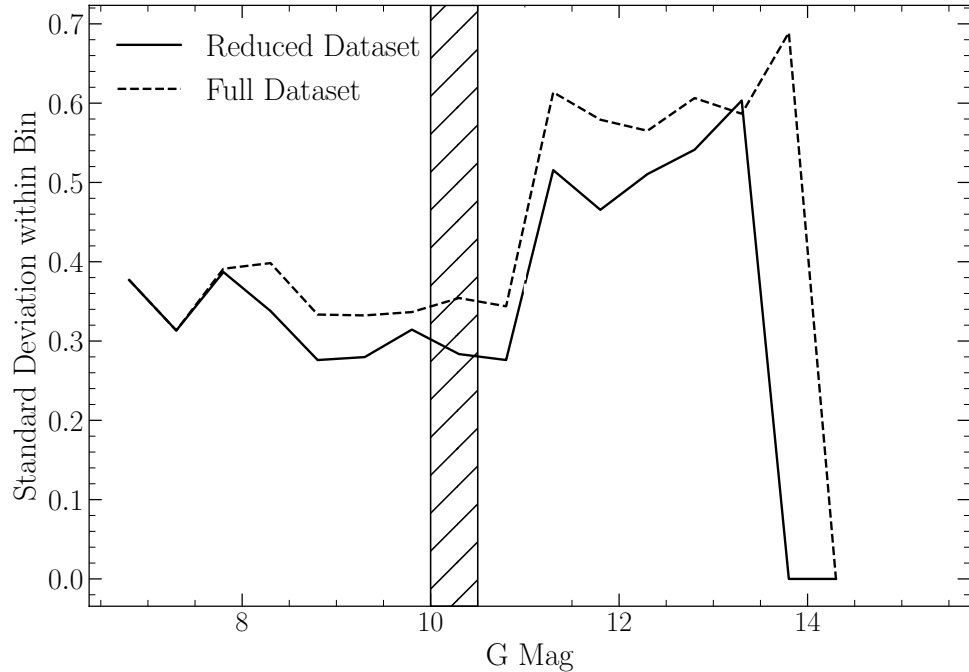


Figure 9.3: Spread in the magnetic activity metric for the merged sample with any stars  $\log(R'_{HK}) > -4.436$  filtered out. **The location of the Gap as identified in literature is shown by the hatched region ( $\sim 10\text{--}10.5 M_G$ ).**

high activity stars). We can further investigate the observed change in variability for only low activity stars by filtering out those stars at or above the saturated threshold for magnetic activity. [Boudreault et al. \(2022\)](#) identify  $\log(R'_{HK}) = -4.436$  as the saturation threshold. We adopt this value and filter out all stars where  $\log(R'_{HK}) \geq -4.436$ . Applying the same analysis to this reduced dataset as was done to the full dataset we still find a discontinuity at the same location (Figure 9.3). This discontinuity is of a smaller magnitude and consequently is more likely to be due purely to noise, with a  $7 \pm 0.2$  percent false alarm probability. This false alarm probability is however only concerned with the first point after the jump in variability. If we consider the false alarm probability of the entire high variability region then the probability that the high variability region is due purely to noise drops to  $1.4 \pm 0.04$  percent.

Further, various authors have shown that the strength of Calcium II H&K emission may evolve over month to year timescales (e.g. [Rauscher & Marcy, 2006](#); [Perdelwitz et al., 2021](#); ?). Targets from [Boudreault et al.](#)

(2022) were observed an average of only four times and over year long timescales. Therefore, the nominal  $\log(R'_{HK})$  values derived in that work may be biased by stellar variability. However, the scale of observed variability in the activity metric is significantly smaller than the star-to-star activity variability addressed here and therefore activity cycles are not expected to be of particular relevance. Specifically, the amplitude of variability is generally  $\Delta \log(R'_{HK}) \lesssim 0.2$  whereas in this work we address variability on the order of  $\Delta \log(R'_{HK}) \lesssim 2$ .

We observe a strong, likely statistically significant, discontinuity in the star-to-star variability of Ca II H&K emission below the magnitude of the Jao Gap. However, modeling is required to determine if this discontinuity may be due to the same underlying physics.

### 9.2.1 Conicidence with the Jao Gap Magnitude

While the observed increase in variability seen here does not seem to be coincident with the Jao Gap — instead appearing to be approximately 0.5 mag fainter, in agreement with what is observed in [Jao et al. \(2023\)](#) — a number of complicating factors prevent us from falsifying that the these two features are not coincident. [Jao et al.](#) find, similar to the results presented here, that the paucity of  $H\alpha$  emission originates below the Gap. Moreover, we use a 0.5 magnitude bin size when measuring the star-to-star variability which injects error into the positioning of any feature in magnitude space. We can quantify the degree of uncertainty the magnitude bin choice injects by conducting Monte Carlo trials where bins are randomly shifted redder or bluer. We conduct 10,000 trials where each trial involves sampling a random shift to the bin start location from a normal distribution with a standard deviation of 1 magnitude. For each trial we identify the discontinuity location as the maximum value of the gradient of the standard deviation (this is the derivative of the data in Figures ?? & 9.3). Some trials result in the maximal value lying at the 0th index of the magnitude array due to edge effects, these trials are rejected (and account for 11% of the trials). The uncertainty in the identified magnitude of the discontinuity due to the selected start

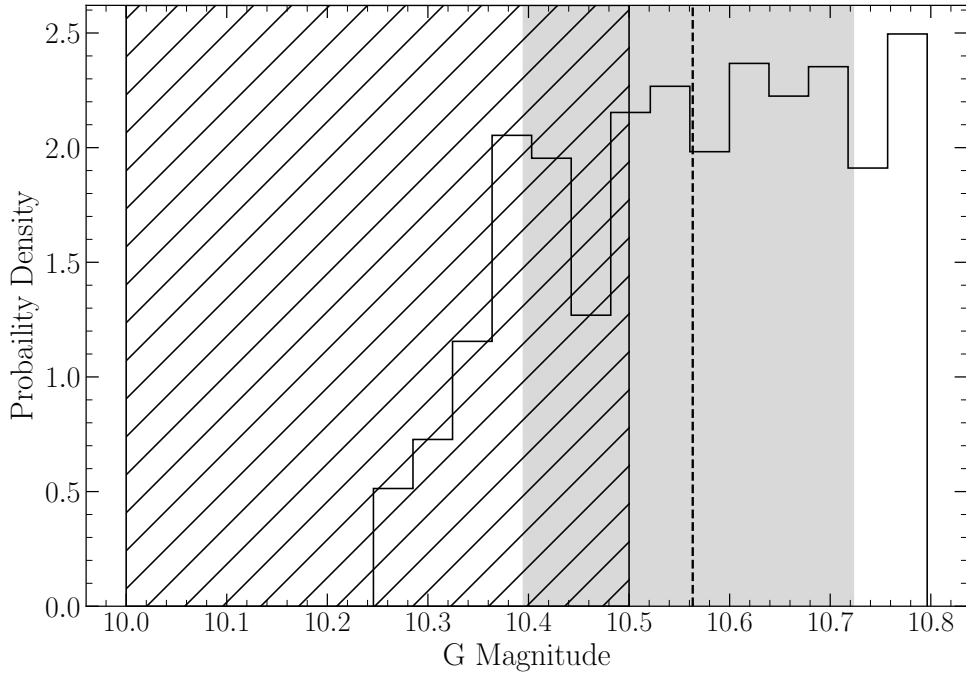


Figure 9.4: Probability density distribution of discontinuity location as identified in the merged dataset. The dashed line represents the mean of the distribution while the shaded region runs from the 16th percentile to the 84th percentile of the distribution. This distribution was built from 10,000 independent samples where the discontinuity was identified as the highest value in the gradient of the standard deviation. **The location of the Gap as identified in literature is shown by the hatched region ( $\sim 10\text{-}10.5 M_G$ ).**

point of the magnitude bins reveals a  $1\sigma = \pm 0.32$  magnitude uncertainty in the location of the discontinuity (Figure 9.4). Finally, all previous studies of the M dwarf Gap (Jao et al., 2018; Jao & Feiden, 2021; Mansfield & Kroupa, 2021; Boudreux et al., 2022; Jao et al., 2023) demonstrate that the Gap has a color dependency, shifting to fainter magnitudes as the population reddens and consequently an exact magnitude range is ill-defined. Therefore we cannot falsify the model that the discontinuity in star-to-star activity variability is coincident with the Jao Gap magnitude.

### 9.2.2 Rotation

It is well known that star's magnetic activity tend to be correlated with their rotational velocity (?Newton et al., 2016; ?; ?; Boudreux et al., 2022); therefore, we investigate whether there is a similar correlation between Gap location and rotational

period in our dataset. All targets from [Boudreax et al. \(2022\)](#) already have published rotational periods; however, targets from [Perdelwitz et al. \(2021\)](#) do not necessarily have published periods. Therefore, we derive photometric rotational periods for these targets here. Given the inherent heterogeneity of M Dwarf stellar surfaces ([??](#)) we are able to determine the rotational period of a star through the analysis of active regions. Various methodologies can be employed for this purpose, including the examination of photometry and light curves (e.g., [Newton et al., 2016](#)), and the observation of temporal changes in the strength of chromospheric emission lines such as Ca II H & K or H $\alpha$  (e.g., [??](#)). In this work, new rotational periods are derived from TESS 2-minute cadence data<sup>1</sup>.

Due to both the large frequency and amplitudes of M dwarf flaring rates the photometric period can prove difficult to measure — as frequency directly correlates with periodicity. Thus, following the process described in [García Soto et al. \(2023\)](#), we utilize two methods in this paper to reduce the effect of flares. One method uses `stella` a python package which implements a series of pre-trained convolutional neural networks (CNNs) to remove flare-shaped features in a light curve ([Feinstein et al., 2020a](#)). The second method separates a star’s photometry into 10 minute bins to account for misshapen flares which `stella` is known to be biased against detecting.

`stella` employs a diverse library of models trained with varying initial seeds ([Feinstein et al., 2020b,a](#)). The Convolutional Neural Networks in `stella` are trained on labeled TESS 2-min for both flares and non-flares. For the purposes of this paper, we use an ensemble of 100 models in `stella`’s library to optimize model performance ([Feinstein et al., 2020b](#), for further detail). `stella` scores flares with a probability of between 0 to 1 — where higher values indicate a higher confidence that a feature is a flare. Here we adopt a score of 0.5 as the cutoff threshold, all features with a score of 0.5 or greater are classed as flares and removed (e.g. [Feinstein et al., 2020b](#)).

Furthermore, we also bin the data from a 2-min to 10-min cadence using the python package `lightkurve`’s binning function ([Lightkurve Collaboration et al., 2018](#);

---

<sup>1</sup>Some M Dwarfs lacking a documented rotational period did not have sufficient TESS data to yield fiducial rotational periods

(Barentsen et al., 2020). This further reduces any flaring-contribution that might have been missed by `stella`<sup>2</sup>. Subsequently, we filter photometry, only retaining data whose residuals are less than 4 times the root-mean-square deviation.

Gaussian processes for modeling the periods are based on Angus et al. (2018) for the subset of M Dwarfs with no fiducial periods. The `starspot` package is adapted for light curve analysis (Angus, 2021; ?). Our Gaussian process kernel function incorporates two stochastically-driven simple harmonic oscillators, representing primary ( $P_{\text{rot}}$ ) and secondary ( $P_{\text{rot}}/2$ ) rotation modes. First, we implement the Lomb-Scargle periodogram within `starspot` to initially estimate the period. After which, we create a maximum a posteriori (MAP) fit using `starspot` to generate a model for stellar rotation. To obtain the posterior of the stellar rotation model, we use Markov Chain Monte Carlo (MCMC) sampling using the `pymc3` package (?) within our adapted `starspot` version. All rotational periods are presented in Table 9.1. Our final sample contains 187 stars with measured rotational periods. We derive new rotational periods for 7 of these.

Table 9.1: All data used from P2021 and B2022.

ID	G Mag	V Mag	K Mag	$\log(R'_{HK})$	e_Log( $R'_{HK}$ )	Ro	prot	r_prot
	mag	mag	mag			d		
2MASS J00094508-4201396	12.14	13.659	8.223	-4.339	0.001	0.009	0.859	Bou22
2MASS J00310412-7201061	12.301	13.648	8.445	-5.388	0.003	0.928	80.969	Bou22
2MASS J01040695-6522272	12.447	13.95	8.532	-4.489	0.001	0.006	0.624	Bou22
2MASS J02004725-1021209	12.778	14.113	9.092	-4.791	0.001	0.188	14.793	Bou22
2MASS J02014384-1017295	13.026	14.477	9.189	-4.54	0.001	0.034	3.152	Bou22
2MASS J02125458+0000167	12.096	13.58	8.168	-4.635	0.001	0.048	4.732	Bou22
2MASS J02411510-0432177	12.251	13.79	8.246	-4.427	0.001	0.004	0.4	Bou22
2MASS J03100305-2341308	12.23	13.5	8.567	-4.234	0.001	0.028	2.083	Bou22
2MASS J03205178-6351524	12.087	13.433	8.195	-5.629	0.004	1.029	91.622	Bou22
2MASS J05015746-0656459	10.649	12.196	6.736	-5.005	0.002	0.875	88.5	Bou22
2MASS J06000351+0242236	9.901	11.31	6.042	-4.547	0.002	0.02	1.809	Bou22
2MASS J06022261-2019447	12.02	13.289	8.374	-5.698	0.006	1.285	95.0	Bou22
2MASS J06105288-4324178	10.996	12.23	7.312	-5.251	0.004	0.726	53.736	Bou22
2MASS J07401183-4257406	12.031	13.835	7.768	-4.336	0.001	0.002	0.307	Bou22
2MASS J08184619-4806172	13.092	14.37	9.351	-4.283	0.001	0.021	1.653	Bou22
2MASS J08443891-4805218	12.434	13.932	8.562	-5.668	0.002	1.348	129.513	Bou22
2MASS J09342791-2643267	12.544	13.992	8.619	-4.341	0.001	0.007	0.694	Bou22

Continued on next page

<sup>2</sup>This is relevant for flares that are misshapen at the start or break in the dataset due to missing either the ingress or egress.

**Table 9.1 – continued from previous page**

ID	G Mag mag	V Mag mag	K Mag mag	$\log(R'_{HK})$	e_Log(R'\$_{HK}\$)	Ro	prot d	r_prot
2MASS J09524176-1536137	12.173	13.463	8.507	-5.632	0.003	1.317	99.662	Bou22
2MASS J11075025-3421003	13.828	15.02	9.407	-4.225	0.001	0.069	7.611	Bou22
2MASS J11381671-7721484	12.816	14.78	8.521	-5.503	0.003			
2MASS J11575352-2349007	13.28	14.77	9.355	-4.295	0.001	0.031	3.067	Bou22
2MASS J12102834-1310234	12.298	13.801	8.412	-4.689	0.001	0.443	42.985	Bou22
2MASS J12384914-3822527	11.226	12.74	7.386	-6.069	0.004			
2MASS J12440075-1110302	12.635	14.18	8.674	-4.405	0.001	0.02	2.099	Bou22
2MASS J13442092-2618350	11.984	13.253	8.285	-5.963	0.005	2.032	154.885	Bou22
2MASS J14211512-0107199	11.82	12.95	8.093	-5.584	0.004	1.279	91.426	Bou22
2MASS J14253413-1148515	12.237	13.51	8.391	-4.764	0.001	0.301	25.012	Bou22
2MASS J14294291-6240465	8.985	11.13	4.384	-5.005	0.001	0.394	83.5	Bou22
2MASS J14340491-1824106	12.738	14.32	8.708	-4.609	0.001	0.275	30.396	Bou22
2MASS J15165576-0037116	13.001	14.472	9.105	-4.07	0.007			
2MASS J15290145-0612461	12.601	14.01	8.781	-4.201	0.001	0.095	8.434	Bou22
2MASS J16204186-2005139	12.326	13.801	8.419	-4.39	0.001	0.029	2.814	Bou22
2MASS J16352464-2718533	12.751	14.2	8.998	-5.596	0.002	1.407	122.656	Bou22
2MASS J16570570-0420559	10.913	12.25	7.12	-4.307	0.001	0.014	1.212	Bou22
2MASS J18494929-2350101	9.126	10.43	5.37	-4.524	0.001	0.036	2.869	Bou22
2MASS J19204795-4533283	10.753	12.23	6.845	-5.839	0.004			
2MASS J20035892-0807472	12.15	13.4	8.286	-5.653	0.004	1.025	84.991	Bou22
2MASS J20091824-0113377	12.673	14.45	8.512	-4.377	0.001	0.01	1.374	Bou22
2MASS J21390081-2409280	12.078	13.4	8.359	-6.194	0.008	1.186	94.254	Bou22
2MASS J22480446-2422075	11.129	12.624	7.206	-4.412	0.001	0.005	0.466	Bou22
2MASS J23071524-2307533	12.376	13.674	8.738	-5.278	0.003	0.684	51.204	Bou22
Karmn J00184+440	9.687	11.04	5.948	-5.439	0.0			
Karmn J01013+613	9.846	10.87	6.483	-5.171	0.0	0.636	34.7	SM18
Karmn J01125-169	10.437	12.074	6.42	-4.585	0.0	0.612	69.2	DA19
Karmn J01433+043	9.907	10.915	6.516	-4.997	0.0			
Karmn J02002+130	10.681	12.298	6.648	-5.131	0.0			
Karmn J02123+035	9.206	10.042	6.077	-5.126	0.0			
Karmn J02358+202	9.709	10.628	6.328	-4.86	0.0	0.615	31.9	DA19
Karmn J02442+255	9.467	10.563	5.961	-5.166	0.0	0.627	38.7	DA19
Karmn J03133+047	12.101	14.001	7.833	-4.602	0.0	0.83	126.2	New16a
Karmn J03181+382	9.415	10.28	6.164	-4.961	0.0	1.654	77.2	DA19
Karmn J03217-066	10.362	11.314	6.983	-4.472	0.0	0.4	21.1	DA19
Karmn J03473-019	10.506	11.537	6.933	-4.026	0.0	0.063	3.88	Rev20
Karmn J04290+219	7.704	8.3	4.875	-4.429	0.0	0.81	25.4	DA19
Karmn J04376+528	7.953	8.648	5.047	-4.39	0.0			
Karmn J04376-110	9.408	10.331	6.091	-5.034	0.0			
Karmn J04429+189	9.004	9.951	5.607	-4.806	0.0	0.765	40.7	DA19
Karmn J04429+214	10.727	11.93	7.101	-5.841	0.0	0.679	47.8	DA19
Karmn J04520+064	10.714	12.018	6.942	-5.007	0.0			

Continued on next page

**Table 9.1 – continued from previous page**

ID	G Mag mag	V Mag mag	K Mag mag	$\log(R'_{HK})$	e_Log( $R'_{HK}$ )	Ro	prot d	r_prot
Karmn J04538-177	9.938	10.894	6.598	-5.081	0.0			
Karmn J05019+011	11.513	12.859	7.677	-4.068	0.0	0.024	2.08	Rev20
Karmn J05019-069	10.649	12.196	6.736	-4.779	0.0	0.875	88.5	Kir12
Karmn J05033-173	10.562	11.735	6.936	-5.095	0.0			
Karmn J05062+046	11.992	13.46	8.067	-4.658	0.0	0.009	0.9	Rev20
Karmn J05127+196	9.815	10.746	6.47	-5.148	0.0			
Karmn J05314-036	7.108	7.968	3.9	-4.67	0.0	0.745	33.8	DA19
Karmn J05365+113	8.195	8.898	5.269	-4.001	0.0	0.326	11.51	CC23
Karmn J05366+112	11.197	12.58	7.406	-4.164	0.0			
Karmn J05421+124	10.114	11.509	6.389	-5.068	0.0			
Karmn J06000+027	9.901	11.31	6.042	-4.274	0.0	0.02	1.8	Rev20
Karmn J06105-218	7.313	8.125	4.17	-4.594	0.0	0.642	27.3	DA19
Karmn J06371+175	8.878	9.593	5.862	-4.871	0.0			
Karmn J07274+052	8.576	9.872	4.857	-5.301	0.0	1.194	93.5	SM17b
Karmn J07287-032	10.296	11.456	6.704	-5.26	0.0			
Karmn J07319+362N	10.506	11.738	6.755	-4.29	0.0	0.213	16.4	DA19
Karmn J07386-212	10.611	11.712	7.063	-5.276	0.0			
Karmn J07393+021	8.898	9.589	5.872	-4.523	0.0			
Karmn J07582+413	10.666	13.912	6.878	-5.335	0.0			
Karmn J08126-215	10.672	12.13	6.705	-4.977	0.0			
Karmn J08161+013	9.133	10.091	5.766	-5.051	0.0	0.773	40.7	DA19
Karmn J08293+039	10.443	11.437	7.026	-4.509	0.0			
Karmn J08409-234	10.765	11.975	7.028	-5.041	0.0			
Karmn J09161+018	11.689	13.03	7.96	-3.772	0.0	0.017	1.4	Rev20
Karmn J09163-186	9.807	10.739	6.492	-4.559	0.0			
Karmn J09307+003	10.502	11.71	6.871	-5.225	0.0			
Karmn J09360-216	9.892	10.906	6.475	-5.448	0.0	1.328	74.3	SM15
Karmn J09411+132	9.443	10.37	6.128	-4.824	0.0			
Karmn J09439+269	10.849	13.962	7.19	-5.235	0.0	0.064	13.7	DA19
Karmn J09447-182	11.082	12.455	7.257	-5.399	0.0			
Karmn J09511-123	9.242	10.016	6.15	-4.773	0.0			
Karmn J09561+627	8.231	9.18	5.2	-4.392	0.0	0.336	14.501	This Work
Karmn J10122-037	8.332	9.264	5.015	-4.555	0.0	0.429	21.6	DA19
Karmn J10167-119	9.934	10.998	6.452	-5.037	0.0			
Karmn J10251-102	9.276	10.139	6.032	-4.583	0.0	0.226	10.483	This Work
Karmn J10289+008	8.676	9.65	5.311	-4.957	0.0	0.617	32.72	CC23
Karmn J10350-094	10.991	12.11	7.393	-5.203	0.0			
Karmn J10396-069	10.27	11.281	6.818	-4.993	0.0			
Karmn J10508+068	10.291	11.675	6.371	-5.041	0.0	0.692	64.0	DA19
Karmn J11000+228	8.977	10.02	5.503	-5.124	0.0	0.092	5.429	This Work
Karmn J11026+219	8.811	9.572	5.688	-5.073	0.0	0.331	13.53	CC23
Karmn J11033+359	6.551	7.52	3.34	-5.284	0.0	0.991	48.0	Kir07

Continued on next page

**Table 9.1 – continued from previous page**

ID	G Mag mag	V Mag mag	K Mag mag	$\log(R'_{HK})$	e_Log(R'_{HK})	Ro	prot d	r_prot
Karmn J11110+304W	9.055	9.983	5.734	-4.688	0.0			
Karmn J11126+189	9.884	10.85	6.579	-4.587	0.0			
Karmn J11302+076	12.401	13.5	8.899	-4.827	0.0	0.63	38.84	CC23
Karmn J11417+427	10.582	13.795	6.822	-5.321	0.0	0.296	71.5	DA19
Karmn J11421+267	9.582	10.613	6.073	-5.274	0.0	0.749	44.6	DA19
Karmn J11467-140	10.616	11.7	7.069	-4.75	0.0			
Karmn J11476+002	11.967	13.34	8.098	-4.452	0.0	0.13	11.6	DA19
Karmn J11477+008	9.601	11.153	5.654	-5.194	0.0	1.576	163.0	DA19
Karmn J11511+352	8.854	9.802	5.606	-4.579	0.0	0.467	22.8	DA19
Karmn J12100-150	10.742	12.083	6.863	-5.365	0.0			
Karmn J12111-199	10.588	11.709	7.044	-5.357	0.0			
Karmn J12189+111	11.926	13.9	7.57	-4.705	0.0	0.003	0.5	DA19
Karmn J12230+640	10.552	13.481	7.122	-5.072	0.0	0.194	32.9	DA19
Karmn J12248-182	10.29	11.272	6.95	-5.339	0.0			
Karmn J12312+086	8.951	9.664	5.892	-4.529	0.0			
Karmn J12350+098	10.453	11.405	7.153	-5.177	0.0	0.725	36.6	DA19
Karmn J12373-208	11.958	13.28	8.085	-5.344	0.0			
Karmn J12388+116	10.336	11.502	6.691	-5.03	0.0			
Karmn J12479+097	10.105	11.395	6.362	-5.463	0.0			
Karmn J13283-023W	10.186	11.336	6.613	-5.189	0.0	0.701	46.42	Rae20
Karmn J13299+102	8.205	9.029	5.036	-4.81	0.0	0.69	30.0	SM17b
Karmn J13427+332	10.72	13.896	6.982	-5.147	0.0			
Karmn J13450+176	9.108	9.75	6.22	-4.964	0.0			
Karmn J13457+148	7.611	8.5	4.415	-5.065	0.0	1.141	52.3	SM15
Karmn J13458-179	10.598	11.872	6.902	-5.24	0.0			
Karmn J13591-198	11.396	12.88	7.445	-4.248	0.0	0.033	3.3	Rev20
Karmn J14010-026	8.863	9.707	5.683	-4.733	0.0	0.992	43.9	SM17b
Karmn J14257+236E	9.205	9.973	6.091	-4.654	0.0	0.432	17.6	DA19
Karmn J14257+236W	9.006	9.72	5.973	-4.553	0.0	2.942	111.0	DA19
Karmn J14294+155	9.733	10.676	6.393	-4.929	0.0	0.847	43.5	SM18
Karmn J14307-086	8.721	9.392	5.769	-4.609	0.0			
Karmn J14310-122	10.668	11.903	6.961	-5.581	0.0			
Karmn J14342-125	9.895	11.317	5.939	-5.264	0.0			
Karmn J15013+055	11.075	12.265	7.432	-5.113	0.0	0.06	4.223	This Work
Karmn J15095+031	10.378	11.473	6.858	-5.128	0.0	0.06	3.756	This Work
Karmn J15194-077	9.422	10.56	5.837	-5.698	0.0	2.002	132.5	SM15
Karmn J15218+209	9.124	10.003	5.756	-4.015	0.0	0.068	3.4	Rev20
Karmn J15369-141	11.369	12.726	7.572	-5.608	0.0			
Karmn J15598-082	9.601	10.487	6.343	-4.58	0.0	0.422	20.0	SM18
Karmn J16028+205	11.167	12.56	7.369	-5.123	0.0			
Karmn J16254+543	9.14	10.07	5.833	-5.331	0.0	1.535	76.8	DA19
Karmn J16303-126	8.802	10.072	5.075	-5.24	0.0	1.536	119.0	DA19

Continued on next page

**Table 9.1 – continued from previous page**

ID	G Mag mag	V Mag mag	K Mag mag	$\log(R'_{HK})$	e_Log( $R'_{HK}$ )	Ro	prot d	r_prot
Karmn J16327+126	11.072	12.158	7.675	-5.287	0.0			
Karmn J16462+164	10.592	11.68	7.094	-5.115	0.0			
Karmn J16554-083N	10.444	11.759	6.724	-5.253	0.0	0.082	6.52	DA19
Karmn J16570-043	10.913	12.25	7.12	-4.425	0.0	0.007	0.55	DA19
Karmn J16581+257	8.824	9.655	5.624	-4.541	0.0	0.536	23.8	DA19
Karmn J17052-050	9.178	10.071	5.975	-5.076	0.0	1.088	50.2	DA19
Karmn J17071+215	10.557	11.677	7.042	-5.197	0.0			
Karmn J17303+055	8.533	9.433	5.422	-4.61	0.0			
Karmn J17378+185	8.743	9.577	5.572	-5.157	0.0			
Karmn J17578+046	8.194	9.511	4.524	-5.359	0.0	1.882	145.0	TP19
Karmn J18051-030	8.519	9.36	5.306	-4.737	0.0	2.838	127.8	SM15
Karmn J18319+406	10.81	12.046	7.184	-5.05	0.0	0.7	50.2	DA19
Karmn J18353+457	9.107	9.83	6.082	-4.737	0.0	0.9	34.0	DA19
Karmn J18363+136	11.154	12.46	7.367	-4.852	0.0	0.613	50.2	DA19
Karmn J18409-133	9.772	10.63	6.546	-4.647	0.0			
Karmn J18419+318	10.201	13.126	6.722	-5.466	0.0			
Karmn J18498-238	9.126	10.43	5.37	-4.435	0.0	0.035	2.85	CC23
Karmn J18580+059	8.461	9.217	5.357	-4.538	0.0	0.874	35.2	DA19
Karmn J19070+208	9.815	10.774	6.521	-5.083	0.0			
Karmn J19072+208	9.805	10.771	6.517	-5.041	0.0	0.075	3.8	DA19
Karmn J19169+051N	8.1	9.115	4.673	-4.862	0.0	0.817	46.0	DA19
Karmn J19216+208	11.934	13.42	7.935	-5.511	0.0	1.296	133.0	DA19
Karmn J19346+045	8.714	9.326	5.918	-4.273	0.0	0.416	12.9	DA19
Karmn J20405+154	11.837	13.41	7.75	-5.482	0.0	0.934	106.0	DA19
Karmn J20450+444	9.829	10.704	6.533	-4.881	0.0	0.413	19.9	DA19
Karmn J20525-169	10.082	11.458	6.199	-5.191	0.0	0.75	67.6	DA19
Karmn J20567-104	10.419	11.487	6.884	-4.678	0.0	0.156	9.63	DA19
Karmn J21019-063	10.183	11.276	6.692	-5.024	0.0			
Karmn J22020-194	10.831	12.03	7.185	-5.316	0.0			
Karmn J22021+014	8.403	9.146	5.322	-4.471	0.0	0.748	29.5	DA19
Karmn J22096-046	9.237	10.366	5.594	-5.042	0.0	0.576	39.2	SM15
Karmn J22125+085	10.908	11.982	7.472	-5.387	0.0			
Karmn J22137-176	12.067	13.672	8.115	-4.646	0.0			
Karmn J22231-176	11.551	13.3	7.319	-4.468	0.0	0.031	4.256	This Work
Karmn J22330+093	9.542	10.373	6.356	-4.853	0.0	0.273	12.038	This Work
Karmn J22468+443	9.005	10.26	5.299	-4.148	0.0	0.057	4.35	Rev20
Karmn J22503-070	9.133	9.847	6.104	-4.497	0.0			
Karmn J22532-142	8.875	10.192	5.01	-5.168	0.0	0.94	81.0	DA19
Karmn J22559+178	9.656	10.558	6.449	-4.495	0.0	0.581	27.0	SM18
Karmn J22565+165	7.795	8.638	4.523	-4.698	0.0	0.847	39.5	DA19
Karmn J23216+172	10.359	11.71	6.507	-5.074	0.0	0.856	74.7	DA19
Karmn J23340+001	10.177	11.16	6.828	-5.36	0.0			

Continued on next page

**Table 9.1 – continued from previous page**

ID	G Mag mag	V Mag mag	K Mag mag	$\log(R'_{HK})$	e_Log(R'_{HK})	Ro	prot d	r_prot
Karmn J23381-162	10.343	11.288	7.003	-5.559	0.0	1.2	61.7	Wat06
Karmn J23492+024	8.153	8.993	5.043	-5.462	0.0	1.177	49.9	SM18

One might expect a decrease in mean rotational period around the magnitude of the Gap, due to the slight decrease in magnetic activity. However, there is no statistically significant correlation between rotational period and G magnitude which we can detect given our sample size (Figure 9.5). Rotational period is however, not the ideal parametrization to use, as magnetic activity is more directly related to the Rossby number ( $Ro$ ). Using the empirical calibration presented in ? (Equation 9.1) we find the mixing timescale for each star such that the Rossby Number is defined as  $Ro = P_{rot}/\tau_c$ .

$$\tau_c = 0.64 + 0.25 * (V - K) \quad (9.1)$$

When we compare Rossby number to G magnitude (Figure 9.6) we find that there may be a slight paucity of rotation coincident with the decrease in spread of the activity metric. We quantify the statistical significance of this drop by building a Gaussian kernel density estimator (kde) based on the data outside of this range, and then resampling that kde 10000 times for each data point in the theorized paucity range. The false alarm probability that that drop is due to noise is then the product of the fraction of samples which are less than or equal to the value of each data point. We find that there is a 0.022 percent probability that this dip is due purely to noise.

### 9.2.3 Limitations

There are two primary limitation of our dataset. First, we only have 264 star in our dataset (with measured  $R'_{HK}$ , 187 with rotational periods) limiting the statistical power of our analysis. This is primarily due to the relative difficulty of obtaining Ca II H&K measurements compared to obtaining  $H\alpha$  measurements. Reliable measurements require both high spectral resolutions ( $R \sim 16000$ ) and a comparatively blue

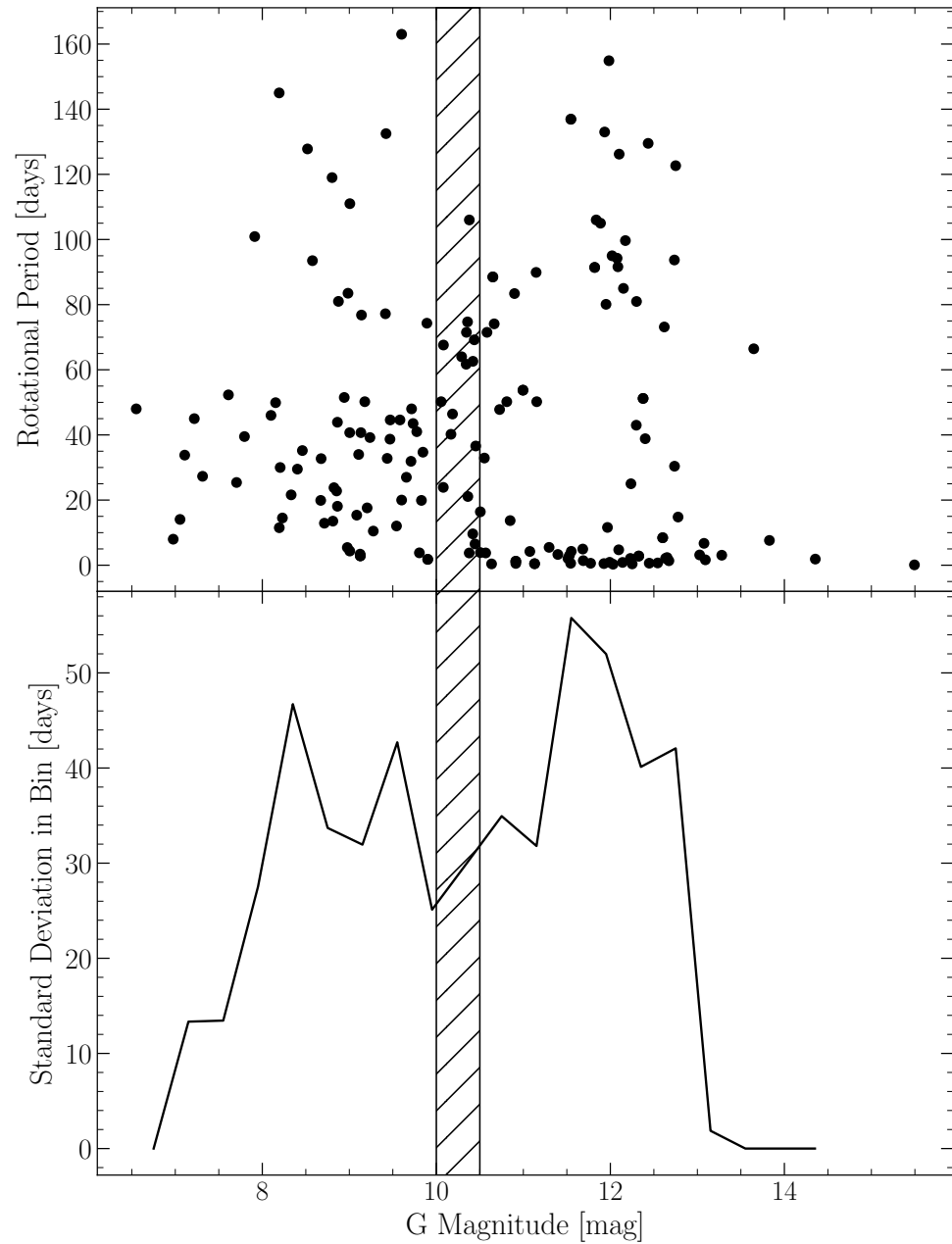


Figure 9.5: Rotational Periods against G magnitude for all stars with rotational periods (top). Standard deviation of rotational period within magnitude bin (bottom). The location of the Gap as identified in literature is shown by the hatched region ( $\sim 10\text{--}10.5 M_G$ ).

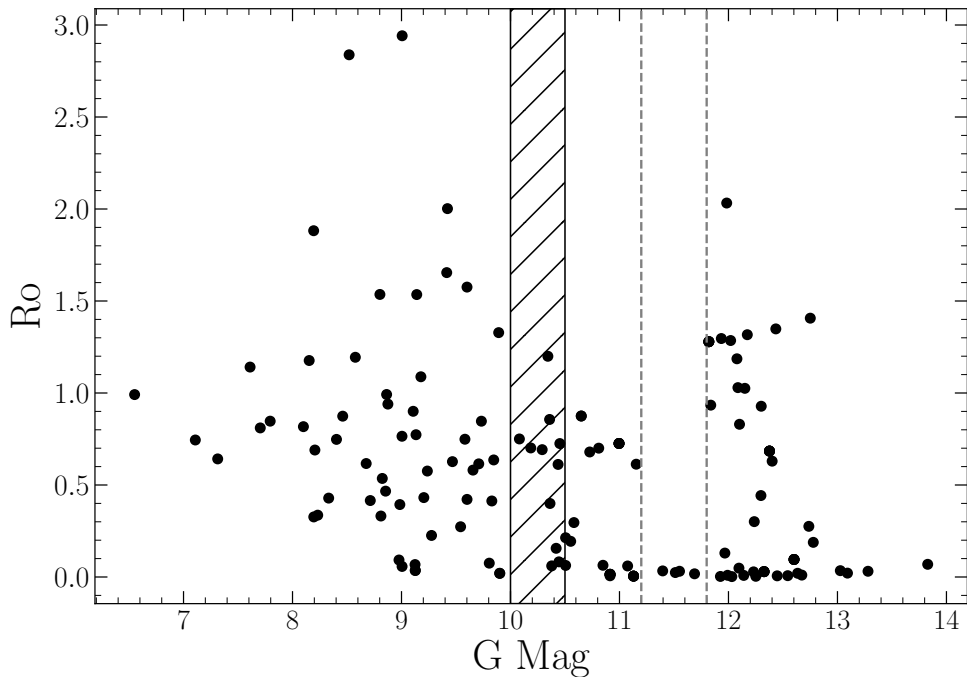


Figure 9.6: Rossby number vs. G magnitude for all stars with rotational periods and V-K colors on Simbad. Dashed lines represent the hypothesized region of decreased rotation. **The location of the Gap as identified in literature is shown by the hatched region ( $\sim 10\text{-}10.5 M_G$ ).**

wavelength range <sup>3</sup>.

Additionally, the sample we do have does not extend to as low mass as would be ideal. This presents a degeneracy between two potential causes for the observed increased star-to-star variability. One option, as presented above and elaborated on in the following section, is that this is due to kissing instabilities. However, another possibility is that this increased variability is intrinsic to the magnetic fields of fully convective stars. This alternate option may be further supported by the shape of the magnetic activity spread vs. G magnitude relation. Convective kissing instabilities are not expected to continue to much lower masses than the fully convective transition mass. The fact that the increase in variance which we observe continues to much fainter magnitudes would therefore be somewhat surprising in a purely convective kissing instability driven framework (though the degeneracy between potentially physically driven increase in variance and increase in variance due to the noise-magnitude relation complicates attempts to constrain this.) There is limited discussion in the literature of overall magnetic field strength spanning the fully convective transition mass; however, [Shulyak et al. \(2019\)](#) present estimated magnetic field strengths for 47 M dwarfs, spanning a larger area around the convective transition region and their dataset does not indicate a inherently increased variability for fully convective stars.

### 9.3 Modeling

One of the most pressing questions related to this work is whether or not the increased star-to-star variability in the activity metric and the Jao Gap, which are coincident in magnitude, are driven by the same underlying mechanism. The challenge when addressing this question arises from current computational limitations. Specifically, the kinds of three dimensional magneto-hydrodynamical simulations — which would be needed to derive the effects of convective kissing instabilities on the magnetic field of the star — are infeasible to run over gigayear timescales while maintaining thermal

---

<sup>3</sup>wrt. to what many spectrographs cover. There is no unified resource listing currently commissioned spectrographs; however, it is somewhat hard to source glass which transmits well at H&K wavelengths limiting the lower wavelength of most spectrographs.

timescale resolutions needed to resolve periodic mixing events.

In order to address this and answer the specific question of *could kissing instabilities result in increased star-to-star variability of the magnetic field*, we adopt a very simple toy model. Kissing instabilities result in a transient radiative zone separating the core of a star (convective) from its envelope (convective). When this radiative zone breaks down two important things happen: one, the entire star becomes mechanically coupled, and two, convective currents can now move over the entire radius of the star. [Jao et al. \(2023\)](#) propose that this mechanical coupling may allow the star's core to act as an angular momentum sink thus accelerating a stars spin down and resulting in anomalously low H $\alpha$  emission.

Regardless of the exact mechanism by which the magnetic field may be affected, it is reasonable to expect that both the mechanical coupling and the change to the scale of convective currents will have some effect on the star's magnetic field. On a microscopic scale both of these will change how packets of charge within a star move and may serve to disrupt a stable dynamo. Therefore, in the model we present here we make only one primary assumption: *every mixing event may modify the star's magnetic field by some amount*. Within our model this assumption manifests as a random linear perturbation applied to some base magnetic field at every mixing event. The strength of this perturbation is sampled from a normal distribution with some standard deviation,  $\sigma_B$ .

Synthetic stars are sampled from a grid of stellar models evolved using the Dartmouth Stellar Evolution Program (DSEP) with similar parameters to those used in ?. Each stellar model was evolved using a high temporal resolution (timesteps no larger than 10,000 years) and typical numerical tolerances of one part in  $10^5$ . Each model was based on a GS98 ([Grevesse & Sauval, 1998](#)) solar composition with a mass range from  $0.3 M_\odot$  to  $0.4 M_\odot$ . Finally, models adopt OPLIB high temperature radiative opacities, Ferguson 2004 low temperature radiative opacities, and include both atomic diffusion and gravitational settling. A Kippenhan-Iben diagram showing the structural evolution of a model within the Gap is shown in Figure 9.7.

Each synthetic star is assigned some base magnetic activity ( $B_0 \sim \mathcal{N}(1, \sigma_B)$ ) and

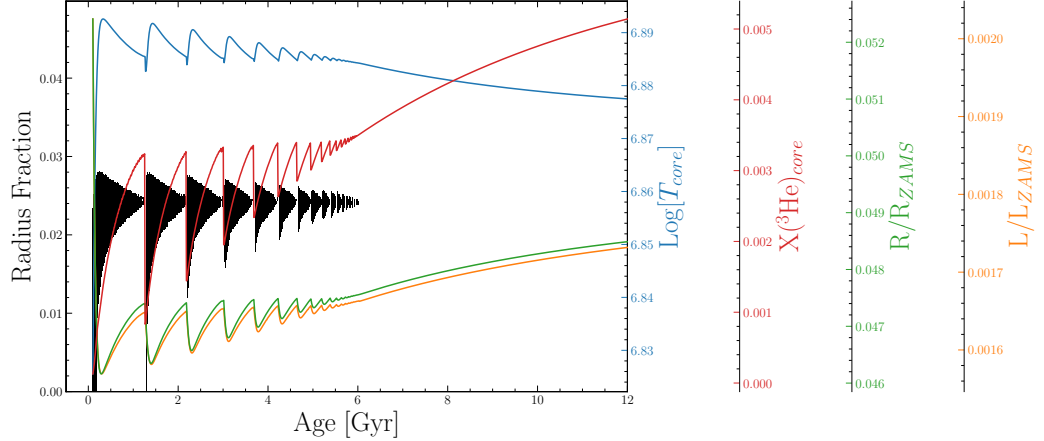


Figure 9.7: Kippenhan-Iben diagram for a 0.345 solar mass star. Note the periodic mixing events (where the plotted curves peak).

then the number of mixing events before some age  $t$  are counted based on local maxima in the core temperature. The toy magnetic activity at age  $t$  for the model is given in Equation 9.2. An example of the magnetic evolution resulting from this model is given in Figure 9.8. Fundamentally, this model presents magnetic activity variation due to mixing events as a random walk and therefore results will increasing divergence over time.

$$B(t) = B_0 + \sum_i B_i \sim \mathcal{N}(1, \sigma_B) \quad (9.2)$$

Applying the same analysis to these models as was done to the observations as described in Section 10.4 we find that this simple model results in a qualitatively similar trend in the standard deviation vs. Magnitude graph (Figure 9.9). In order to reproduce the approximately 50 percent change to the spread of the activity metric observed in the combined dataset in section 10.4 a distribution with a standard deviation of 0.1 is required when sampling the change in the magnetic activity metric at each mixing event. This corresponds to 68 percent of mixing events modifying the activity strength by 10 percent or less. The interpretation here is important: what this qualitative similarity demonstrates is that it may be reasonable to expect kissing instabilities to result in the observed increased star-to-star variation. Importantly, we

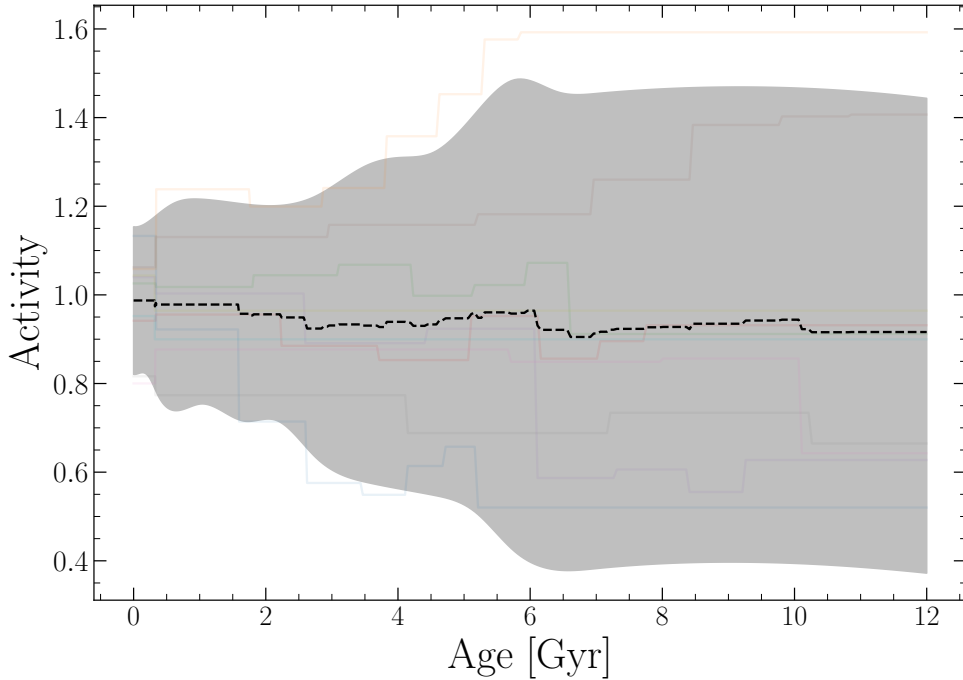


Figure 9.8: Example of the toy model presented here resulting in increased divergence between stars magnetic fields. The shaded region represents the maximum spread in the two point correlation function at each age.

are not able to claim that kissing instabilities *do* lead to these increased variations, only that they reasonably could. Further modeling, observational, and theoretical efforts will be needed to more definitively answer this question.

### 9.3.1 Limitations

The model presented in this paper is very limited and it is important to keep these limitations in mind when interpreting the results presented here. Some of the main challenges which should be leveled at this model are the assumption that the magnetic field will be altered by some small random perturbation at every mixing event. This assumption was informed by the large number of free parameters available to a physical star during the establishment of a large scale magnetic field and the associated likely stochastic nature of that process. However, it is similarly believable that the magnetic field will tend to alter in a uniform manner at each mixing event. For example, since differential rotation is generally proportional to the temperature gradient within a star and activity is strongly coupled to differential rotation then it

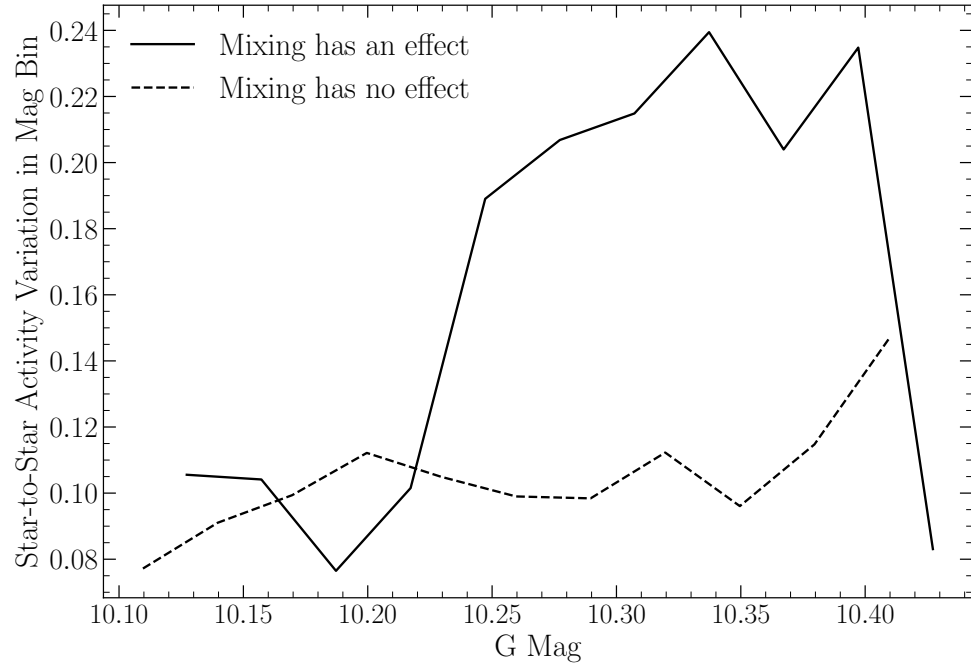


Figure 9.9: Toy model results showing a qualitatively similar discontinuity in the star-to-star magnetic activity variability.

may be that as the radiative zone reforms over thermal timescales the homogenization of angular momentum throughout the star results in overall lower amounts of differential rotation each after mixing event than would otherwise be present.

Moreover, this model does not consider how other degenerate sources of magnetic evolution such as stellar spin down, relaxation, or coronal heating may effect star-to-star variability. These could conceivably lead to a similar increase in star-to-star variability which is coincident with the Jao Gap magnitude as the switch from fully to partially convective may effect efficiency of these process.

Additionally, there are challenges with this toy model that originate from the stellar evolutionary model. Observations of the Jao Gap show that the feature is not perpendicular to the magnitude axis; rather, it is inversely proportional to the color. No models of the Jao Gap published at the time of writing capture this color dependency and *what causes this color dependency* remains one of the most pressing questions relating to the underlying physics. This non captured physics is one potential explanation for why the magnitude where our model predicts the increase in variability is not in agreement with where the variability jump exists in the data.

Finally, we have not considered detailed descriptions of the dynamos of stars. The magnetohydrodynamical modeling which would be required to model the evolution of the magnetic field of these stars at thermal timescale resolutions over gigayears is currently beyond the ability of practical computing. Therefore future work should focus on limited modeling which may inform the evolution of the magnetic field directly around the time of a mixing event.

## 9.4 Conclusion

It is, at this point, well established that the Jao Gap may provide a unique view of the interiors of stars for which other probes, such as seismology, fail. However, it has only recently become clear that the Gap may lend insight into not just structural changes within a star but also into the magnetic environment of the star. [Jao et al. \(2023\)](#) presented evidence that the physics driving the Gap might additionally result in a paucity of H $\alpha$  emission. These authors propose potential physical mechanisms which could explain this paucity, including the core of the star acting as an angular momentum sink during mixing events.

Here we have expanded upon this work by probing the degree and variability of Calcium II H&K emission around the Jao Gap. We lack the same statistical power of [Jao et al.](#)'s sample; however, by focusing on the star-to-star variability within magnitude bins we are able to retain statistical power. We find that there is an anomalous increase in variability at a G magnitude of  $\sim 11$ . This is only slightly below the observed mean gap magnitude.

Additionally, we propose a simple model to explain this variability. Making the assumption that the periodic convective mixing events will have some small but random effect on the overall magnetic field strength we are able to qualitatively reproduce the increase activity spread in a synthetic population of stars.

## **Part III**

# **Individual Stars as Laboratories**



# Chapter 10

## Magnetic Fields In M Dwarfs

### 10.1 Magnetic Activity in M dwarfs

M-dwarfs are the most numerous stars in our galaxy. Some planet search campaigns have focused on M-dwarfs due to the relative ease of detecting small planets in their habitable zones (e.g. Nutzman & Charbonneau, 2008); however, spun-up M-dwarfs are more magnetically active when compared to larger and hotter stars (Hawley & Pettersen, 1991; Delfosse et al., 1998; Schmidt et al., 2014). The increase in activity may accelerate the stripping of an orbiting planet's atmosphere (e.g. Owen & Mohanty, 2016), and may dramatically impact habitability (Shields et al., 2016). Therefore, it is essential to understand the magnetic activity of M-dwarfs in order to constrain the potential habitability and history of the planets that orbit them. Additionally, rotation and activity may impact the detectability of hosted planets (e.g. Robertson et al., 2014; Newton et al., 2016; Vanderburg et al., 2016).

Robust theories explaining the origin of solar-like magnetic fields exist and have proven extensible to other regions of the main sequence (Charbonneau, 2014). The classical  $\alpha\Omega$  dynamo relies on differential rotation between layers of a star to stretch a seed poloidal field into a toroidal field (Parker, 1955; Cameron et al., 2017). Magnetic buoyancy causes the toroidal field to rise through the star. During this rise, turbulent helical stretching converts the toroidal field back into a poloidal field (Parker, 1955). Seed fields may originate from the stochastic movement of charged particles within a star's atmospheres.

In non-fully convective stars the initial conversion of the toroidal field to a poloidal field is believed to take place at the interface layer between the radiative and convective regions of a star — the tachocline (Noyes et al., 1984; Tomczyk et al., 1996; Dikpati & Charbonneau, 1999). The tachocline has two key properties that allow it to play an important role in solar type magnetic dynamos: 1), there are high shear stresses, which have been confirmed by astroseismology (Thompson et al., 1996), and 2), the density stratification between the radiative and convective zones serves to “hold” the newly generated toroidal fields at the tachocline for an extended time. Over this time, the fields build in strength significantly more than they would otherwise (Parker, 1975). This theory does not trivially extend to mid-late M-dwarfs, as they are believed to be fully convective and consequently do not contain a tachocline (?). Moreover, fully convective M-dwarfs are not generally expected to exhibit internal differential rotation (e.g. Barnes et al., 2004, 2005), though, some models do produce it (Gastine et al., 2014).

Currently, there is no single accepted process that serves to build and maintain fully convective M-dwarf magnetic fields in the same way that the  $\alpha$  and  $\Omega$  processes are presently accepted in solar magnetic dynamo theory. Three-dimensional magneto anelastic hydrodynamical simulations have demonstrated that local fields generated by convective currents can self organize into large scale dipolar fields. These models indicate that for a fully convective star to sustain a magnetic field it must have a high degree of density stratification — density contrasts greater than 20 at the tachocline — and a sufficiently large magnetic Reynolds number<sup>1</sup>.

An empirical relation between the rotation rate and the level of magnetic activity has been demonstrated in late-type stars (Skumanich, 1972; Pallavicini et al., 1981). This is believed to be a result of faster rotating stars exhibiting excess non-thermal emission from the upper chromosphere or corona when compared to their slower rotating counterparts. This excess emission is due to magnetic heating of the upper atmosphere, driven by the underlying stellar dynamo. **The faster a star rotates, up to some saturation threshold, the more such emission is expected.**

---

<sup>1</sup>The Reynolds Number is the ratio of magnetic induction to magnetic diffusion; consequently, a plasma with a larger magnetic Reynolds number will sustain a magnetic field for a longer time than a plasma with a smaller magnetic Reynolds number.

However, the dynamo process is not dependent solely on rotation; rather, it depends on whether the contribution from the rotational period ( $P_{rot}$ ) or convective motion — parameterized by the convective overturn time scale ( $\tau_c$ ) — dominates the motion of a charge packet within a star. Therefore, the Rossby Number ( $Ro = P_{rot}/\tau_c$ ) is often used in place of the rotational period as it accounts for both.

The rotation-activity relation was first discovered using the ratio of X-ray luminosity to bolometric luminosity ( $L_X/L_{bol}$ ) (Pallavicini et al., 1981) and was later demonstrated to be a more general phenomenon, observable through other activity tracers, such as Ca II H&K emission (Vilhu, 1984). This relation has a number of important structural elements. Noyes et al. (1984) showed that magnetic activity as a function of Rossby Number is well modeled as a piecewise power law relation including a saturated and non-saturated regime. In the saturated regime, magnetic activity is invariant to changes in Rossby Number; in the non-saturated regime, activity decreases as Rossby Number increases. The transition between the saturated and non-saturated regions occurs at  $Ro \sim 0.1$  (e.g. Wright et al., 2011). Recent evidence may suggest that, instead of an unsaturated region where activity is fully invariant to rotational period, activity is more weakly, but still positively, correlated with rotation rate (Mamajek & Hillenbrand, 2008; Reiners et al., 2014; Lehtinen et al., 2020; Magaudda et al., 2020).

Previous studies of the Ca II H&K rotation-activity relation (e.g. Vaughan et al., 1981; Suárez Mascareño et al., 2015; Astudillo-Defru et al., 2017; Houdebine et al., 2017) have focused on spectral ranges which both extend much earlier than M-dwarfs and which do not fully probe late M-dwarfs. **Other studies have relied on  $v \sin(i)$  measurements (e.g. Browning et al., 2010; Houdebine et al., 2017), which are not sensitive to the long rotation periods reached by slowly rotating, inactive mid-to-late type M dwarfs (70-150 days: Newton et al., 2016).** Therefore, these studies can present only coarse constraints on the rotation activity relation in the fully convective regime. The sample we present in this paper is focused on mid-to-late type M dwarfs, **with photometrically measured rotational periods**, while maintaining of order the same number of targets as previous

studies. Consequently, we provide much finer constraints on the rotation–activity relation in this regime.

We present a high resolution spectroscopic study of 53 mid-late M-dwarfs. We measure Ca II H&K strengths, quantified through the  $R'_{HK}$  metric, which is a bolometric flux normalized version of the Mount Wilson S-index. These activity tracers are then used in concert with photometrically determined rotational periods, compiled by [Newton et al. \(2017\)](#), to generate a rotation–activity relation for our sample. This paper is organized as follows: Section 10.2 provides an overview of the observations and data reduction, Section 10.3 details the analysis of our data, and Section 10.4 presents our results and how they fit within the literature.

## 10.2 Observations & Data Reduction

We **initially** selected a sample of 55 mid-late M-dwarfs from targets of the MEarth survey ([Berta et al., 2012](#)) to observe. Targets were selected based on high proper motions and availability of a previously measured photometric rotation period, or an expectation of a measurement based on data available from MEarth-South at the time. These rotational periods were derived photometrically (e.g. [Newton et al., 2016](#); [Mann et al., 2016](#); [Medina et al., 2020](#)). For star 2MASS J06022261-2019447, which was categorized as an “uncertain detection” from MEarth photometry by [Newton et al. \(2018\)](#), including new data from MEarth DR10 we find a period of 95 days. This value was determined following similar methodology to [Irwin et al. \(2011\)](#) and [Newton et al. \(2016, 2018\)](#), and is close to the reported candidate period of 116 days. References for all periods are provided in the machine readable version of Table 10.1.

High resolution spectra were collected from March to October 2017 using the Magellan Inamori Kyocera Echelle (MIKE) spectrograph on the 6.5 meter Magellan 2 telescope at the Las Campanas Observatory in Chile. MIKE is a high resolution double echelle spectrograph with blue and red arms. Respectively, these cover wavelengths from 3350 - 5000 Å and 4900-9500 Å ([Bernstein et al., 2003](#)). We collected data using a 0.75x5.00” slit resulting in a resolving power of 32700. Each science target was observed an average of four times with mean integration times per obser-

vation ranging from 53.3 to 1500 seconds. **Ca II H&K lines were observed over a wide range of signa-to-noise ratios, from  $\sim 5$  up to  $\sim 240$  with mean and median values of 68 and 61 respectively.**

We use the CarPy pipeline (Kelson et al., 2000; Kelson, 2003) to reduce our blue arm spectra. CarPy’s data products are wavelength calibrated, blaze corrected, and background subtracted spectra comprising 36 orders. We shift all resultant target spectra into the rest frame by cross correlating against a velocity template spectrum. For the velocity template we use an observation of Proxima Centari in our sample. This spectrum’s velocity is both barycentrically corrected, using astropy’s `SkyCoord` module (Astropy Collaboration et al., 2018), and corrected for Proxima Centari’s measured radial velocity,  $-22.4 \text{ km s}^{-1}$  (Torres et al., 2006). Each echelle order of every other target observation is cross correlated against the corresponding order in the template spectra using `specutils template correlate` function (Earl et al., 2021). Velocity offsets for each order are inferred from a Gaussian fit to the correlation vs. velocity lag function. For each target, we apply a three sigma clip to list of echelle order velocities, visually verifying this clip removed low S/N orders. We take the mean of the sigma-clipped velocities Finally, each wavelength bin is shifted according to its measured velocity.

Ultimately, two targets (2MASS J16570570-0420559 and 2MASS J04102815-5336078) had S/N ratios around the Ca II H&K lines which were too low to be of use, reducing the number of  $R'_{HK}$  measurement we can make from 55 to 53.

### 10.3 Analysis

Since the early 1960s, the Calcium Fraunhauer lines have been used as chromospheric activity tracers (Wilson, 1963). Ca II H&K lines are observed as a combination of a broad absorption feature originating in the upper photosphere along with a narrow emission feature from non-thermal heating of the upper chromosphere (Catalano & Marilli, 1983). Specifically, the ratio between emission in the Ca II H&K lines and flux contributed from the photosphere is used to define an activity metric known as the S-index (Wilson, 1968). The S-index increases with increasing magnetic activity.

The S-index is defined as

$$S = \alpha \frac{f_H + f_K}{f_V + f_R} \quad (10.1)$$

where  $f_H$  and  $f_K$  are the integrated flux over triangular passbands with a full width at half maximum of 1.09 Å centered at 3968.47 Å and 3933.66 Å, respectively. The values of  $f_V$  and  $f_R$  are integrated, top hat, broadband regions. They approximate the continuum (Figure 10.1) and are centered at 3901 Å and 4001 Å respectively, with widths of 20 Å each. Finally,  $\alpha$  is a scaling factor with  $\alpha = 2.4$ .

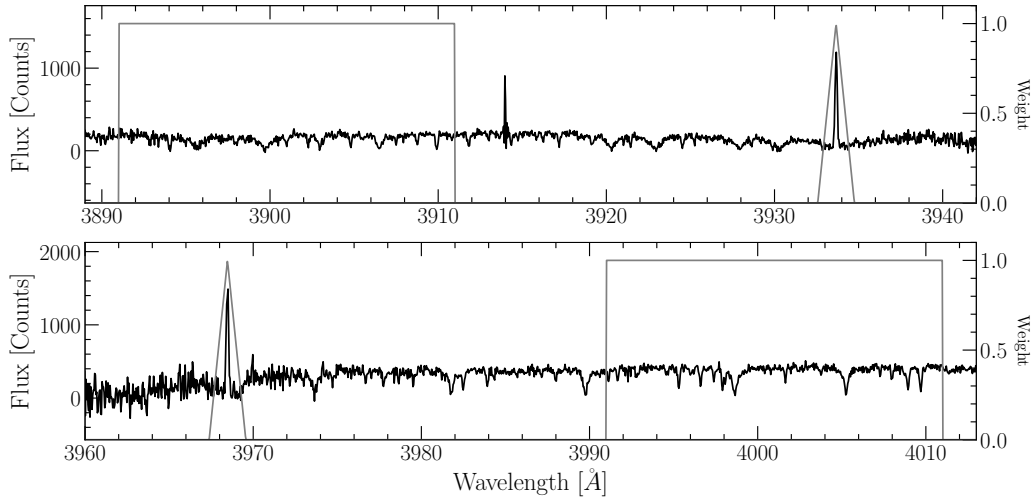


Figure 10.1: Spectrum of 2MASS J06105288-4324178 overplotted with the S index bandpasses. (top) V band and Ca II K emission line. (bottom) Ca II H emission line and R band. Note that the rectangular and triangular regions denote both the wavelength range of the band and the relative weight assigned to each wavelength in the band while integrating.

Following the procedure outlined in Lovis et al. (2011) we use the mean flux per wavelength interval,  $\tilde{f}_i$ , as opposed to the integrated flux over each passband when computing the S-index. This means that for each passband,  $i$ , with a blue most wavelength  $\lambda_{b,i}$  and a red most wavelength  $\lambda_{r,i}$ ,  $\tilde{f}_i$  is the summation of the product of flux ( $f$ ) and weight ( $w_i$ ) over the passband.

$$\tilde{f}_i = \frac{\sum_{l=\lambda_{b,i}}^{\lambda_{r,i}} f(l)w_i(l)}{\lambda_{r,i} - \lambda_{b,i}} \quad (10.2)$$

where  $w_i$  represents the triangular passband for  $f_H$  &  $f_K$  and the tophat for  $f_V$  &  $f_R$ .

Additionally, the spectrograph used at Mount Wilson during the development of the S-index exposed the H & K lines for eight times longer than the continuum of the spectra. Therefore, for a modern instrument that exposes the entire sensor simultaneously, there will be 8 times less flux in the Ca II H&K passbands than the continuum passbands than for historical observations. This additional flux is accounted for by defining a new constant  $\alpha_H$ , defined as:

$$\alpha_H = 8\alpha \left( \frac{1.09 \text{ \AA}}{20 \text{ \AA}} \right) \quad (10.3)$$

Therefore, S-indices are calculated here not based on the historical definition given in Equation 10.1; rather, the slightly modified version:

$$S = \alpha_H \frac{\tilde{f}_H + \tilde{f}_K}{\tilde{f}_V + \tilde{f}_R} \quad (10.4)$$

The S-index may be used to make meaningful comparisons between stars of similar spectral class; however, it does not account for variations in photospheric flux and is therefore inadequate for making comparisons between stars of different spectral classes. The  $R'_{HK}$  index (Middelkoop, 1982) is a transformation of the S-index intended to remove the contribution of the photosphere.

$R'_{HK}$  introduces a bolometric correction factor,  $C_{cf}$ , developed by Middelkoop (1982) and later improved upon by Rutten (1984). Calibrations of  $C_{cf}$  have focused on FGK-type stars using broad band color indices, predominately B-V. However, these FGK-type solutions do not extend to later type stars easily as many mid-late M-dwarfs lack B-V photometry. Consequently,  $C_{cf}$  based on B-V colors were never calibrated for M-dwarfs as many M-dwarfs lack B and V photometry. Suárez Mascareño et al. (2016) provided the first  $C_{cf}$  calibrations for M-dwarfs using the more appropriate color index of  $V - K$ . The calibration was later extended by Astudillo-Defru et al. (2017), which we adopt here.

Generally  $R'_{HK}$  is defined as

$$R'_{HK} = K\sigma^{-1}10^{-14}C_{cf}(S - S_{phot}) \quad (10.5)$$

where K is a factor to scale surface fluxes of arbitrary units into physical units; the current best value for K is taken from Hall et al. (2007),  $K = 1.07 \times 10^6 \text{ erg cm}^{-2} \text{ s}^{-1}$ .  $S_{phot}$  is the photospheric contribution to the S-index; in the spectra this manifests as the broad absorption feature wherein the narrow Ca II H&K emission resides.  $\sigma$  is the Stephan-Boltzmann constant. If we define

$$R_{phot} \equiv K\sigma^{-1}10^{-14}C_{cf}S_{phot} \quad (10.6)$$

then we may write  $R'_{HK}$  as

$$R'_{HK} = K\sigma^{-1}10^{-14}C_{cf}S - R_{phot}. \quad (10.7)$$

We use the color calibrated coefficients for  $\log_{10}(C_{cf})$  and  $\log_{10}(R_{phot})$  presented in Table 1 of Astudillo-Defru et al. (2017).

We estimate the uncertainty of  $R'_{HK}$  as the standard deviation of a distribution of  $R'_{HK}$  measurements from 5000 Monte Carlo tests. For each science target we offset the flux value at each wavelength bin by an amount sampled from a normal distribution. The standard deviation of this normal distribution is equal to the estimated error at each wavelength bin. These errors are calculated at reduction time by the pipeline. **The  $R'_{HK}$  uncertainty varies drastically with signal-to-noise; targets with signal-to-noise ratios  $\sim 5$  have typical uncertainties of a few percent whereas targets with signal-to-noise ratios  $\sim 100$  have typical uncertainties of a few tenth of a percent.**

### 10.3.1 Rotation and Rossby Number

The goal of this work is to constrain the rotation activity relation; therefore, in addition to the measured  $R'_{HK}$  value, we also need the rotation of the star. As mentioned, one of the selection criteria for targets was that their rotation periods were already measured; however, ultimately **6** of the 53 targets with acceptable S/N did not have well constrained rotational periods. We therefore only use the remaining 47 targets to fit the rotation-activity relation.

In order to make the most meaningful comparison possible we transform rotation period into Rossby Number . This transformation was done using the convective overturn timescale,  $\tau_c$ , such that the Rossby Number,  $Ro = P_{rot}/\tau_c$  . To first order  $\tau_c$  can be approximated as 70 days for fully-convective M-dwarfs (Pizzolato et al., 2000). However, Wright et al. (2018) Equation (5) presents an empirically calibrated expression for  $\tau_c$ . This calibration is derived by fitting the convective overturn timescale as a function of color index, in order to minimize the horizontal offset between stars of different mass in the rotation-activity relationship. The calibration from Wright et al. (2018) that we use to find convective overturn timescales and subsequently Rossby numbers is:

$$\log_{10}(\tau_c) = (0.64 \pm 0.12) + (0.25 \pm 0.08)(V - K) \quad (10.8)$$

We adopt symmetric errors for the parameters of Equation 10.8 equal to the larger of the two anti-symmetric errors presented in Wright et al. (2018) Equation 5.

## 10.4 Rotation–Activity Relation

We show our rotation-activity relation in Figures 10.2 & 10.3. Note that errors are shown in both figures; however, they render smaller than the data point size. Ca II H&K is also known to be time variable (e.g. Baroch et al., 2020; Perdelwitz et al., 2021), which is not captured in our single-epoch data. There is one target cut off by the domain of this graph, 2MASS J10252645+0512391. This target has a measured  $v\sin i$  of  $59.5 \pm 2.1$   $\text{km s}^{-1}$  (Kesseli et al., 2018) and is therefore quite rotationally broadened, which is known to affect  $R'_{HK}$  measurements (Schröder et al., 2009, figure 8). The data used to generate this figure is given in Table 10.1. Table 10.1 includes uncertainties, the  $R'_{HK}$  measurements for stars which did not have photometrically derived rotational periods in MEarth, and data for 2MASS J10252645+0512391

We find a rotation activity relationship qualitatively similar to that presented in

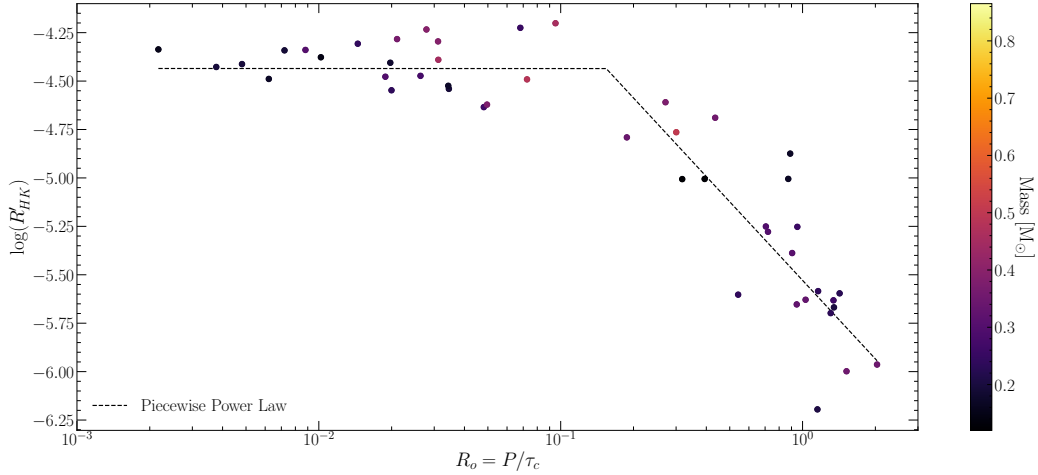


Figure 10.2: Rotation activity relation from this work. The color axis gives each stars mass. The dashed line is the best fit to our data set.

[Astudillo-Defru et al. \(2017\)](#). Our rotation activity relationship exhibits both the expected saturated and unsaturated regimes — the flat region at  $Ro < Ro_s$  and the sloped region at  $Ro \geq Ro_s$  respectively. We fit the rotation activity relation given in Equation 10.9 to our data using Markov Chain Monte Carlo (MCMC), implemented in `pymc` ([Salvatier et al., 2016](#)).

$$\log(R'_{HK}) = \begin{cases} \log(R_s) & Ro < Ro_s \\ k \log(Ro) + \log(R_s) - k \log(Ro_s) & Ro \geq Ro_s \end{cases} \quad (10.9)$$

$Ro_s$  is the Rossby number cutoff between the saturated and unsaturated regime.  $R_s$  is the maximum, saturated, value of  $R'_{HK}$  and  $k$  is the index of the power law when  $Ro \geq Ro_s$ . **Due to the issues measuring  $R'_{HK}$  for high  $vsini$  targets discussed above, we exclude 2MASS J10252645+0512391 from this fit.** All logarithms are base ten unless another base is explicitly given.

We find best fit parameters with one  $\sigma$  errors:

- $k = -1.347 \pm 0.203$
- $Ro_s = 0.155 \pm 0.045$
- $\log(R_s) = -4.436 \pm 0.048$

A comparison of the rotation activity derived in this work to those from

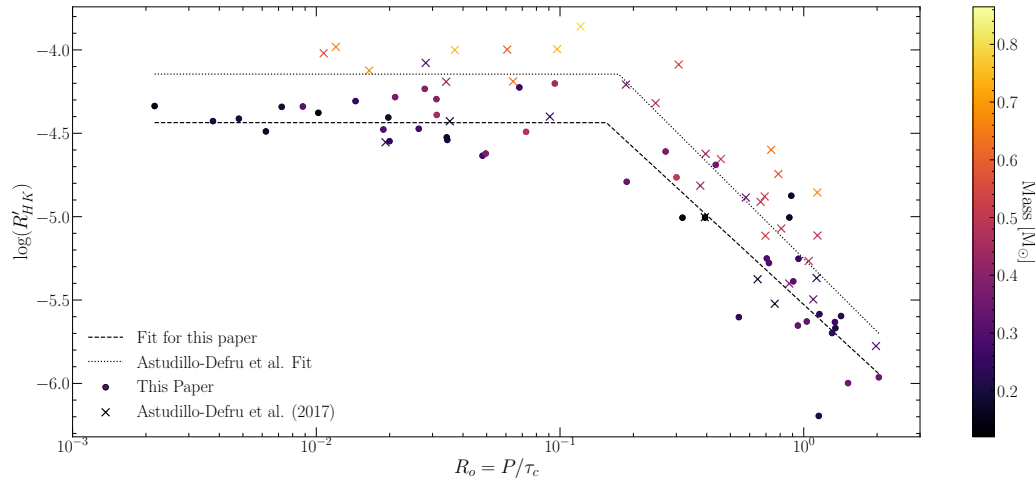


Figure 10.3: Rotation activity relation for both our work and [Astudillo-Defru et al. \(2017\)](#). The dotted line is the best fit to the re-derived rotation-activity relation from [Astudillo-Defru et al. \(2017\)](#). Note that targets from [Astudillo-Defru et al. \(2017\)](#) are systematically higher than targets presented here as a consequence of the range in mass probed by the samples.

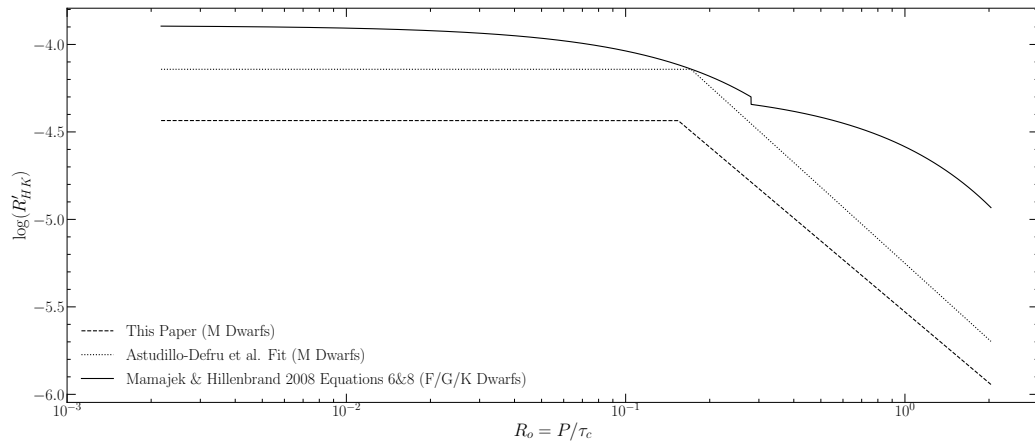


Figure 10.4: Derived rotation-activity curves from this work, [Astudillo-Defru et al. \(2017\)](#) and [Mamajek & Hillenbrand \(2008\)](#). Note both that [Mamajek & Hillenbrand \(2008\)](#) focuses their work on earlier spectral classes and fits the rotation activity relation in linear space.

both [Astudillo-Defru et al. \(2017\)](#) and [Mamajek & Hillenbrand \(2008\)](#) is presented in Figure 10.4. For the 6 targets which do not have measured rotational periods we include an estimate of  $Ro$  and  $p_{rot}$  in the machine readable version of Table 10.1. The convective overturn timescale for one of these 6 targets (2MASS J13464102-5830117) can not be inferred via Equation 10.8 as it lacks a V-K color measurement. Instead, we infer  $\tau_c$  via [Wright et al. \(2018\)](#) Equation 6 (this paper Equation 10.10) using mass. Similar to our manner of inferring  $\tau_c$  via color, when inferring  $\tau_c$  via mass, we adopt the larger of the two antisymmetric errors from [Wright et al. \(2018\)](#).

$$\log_{10}(\tau_c) = 2.33 \pm 0.06 - 1.5 \pm 0.21 (M/M_\odot) + 0.31 \pm 0.17 (M/M_\odot)^2 \quad (10.10)$$

Note that  $R'_{HK}$  for one of six of these targets (2MASS J15165576-0037116) is consistent to within  $1\sigma$  of the saturated value; therefore, the reported  $Ro$  for this target should only be taken as an upper bound. The remaining five targets have measured  $R'_{HK}$  values consistent with the unsaturated regime. Estimated periods are consistent with previous constraints. Of the six stars, two were listed as non-detections in [Newton et al. \(2018\)](#), and the remaining four as uncertain (possible) detections. Of the four classed as uncertain, 2MASS 12384914-3822527 and 2MASS 19204795-4533283 have candidate periods  $> 100$  days and non-detections of H-alpha emission ([Hawley et al., 1996](#)). These two stars and the two non-detections have Ca II H&K activity levels suggesting very long periods. 2MASS 13464102-5830117 has a candidate period of 45 days, and 2MASS 15165576-0037116 of 0.8 days, both consistent with their higher levels of Ca II H&K emission.

As a test of the proposed weak correlation between activity and rotation in the “saturated” regime seen in some works ([Mamajek & Hillenbrand, 2008](#); [Reiners et al., 2014](#); [Lehtinen et al., 2020](#); [Medina et al., 2020](#)) — though not

in others (Wright et al., 2011; Núñez et al., 2015; Newton et al., 2017) — we fit a second model whose power law index is allowed to vary at  $Ro < Ro_s$ . We find a saturated regime power law index of  $-0.052 \pm 0.117$ , consistent with 0 to within  $1\sigma$ . Moreover, all other parameter for this model are consistent to within one  $\sigma$  of the nominal parameters for the model where the index is constrained to 0 below  $Ro = Ro_s$ . We can constrain the slope in the saturated regime to be between -0.363 and 0.259 at the  $3\sigma$  confidence level. Ultimately, we adopt the most standard activity interpretation, a fully-saturated regime at  $Ro < Ro_s$ .

We investigate whether our lack of detection of a slope for  $Ro < Ro_s$  is due to the limited number of observations in that region when compared to other works (e.g. Medina et al., 2020, 93 targets  $Ro < Ro_s$ ) through injection and recovery tests. We inject, fake, rotation-activity measurements into the saturated regime with an a priori slope of -0.13 — the same as in Medina et al.. These fake data are given a standard deviation equal to the standard deviation of our residuals (12%). We preform the same MCMC model fitting to this new data set as was done with the original dataset multiple times, each with progressively more injected data, until we can detect the injected slope to the three sigma confidence level. Ultimately, we need more than 65 data points — 43 more than we observed in the saturated regime — to consistently recover this slope. Therefore, given the spread of our data we cannot detect slopes on the order of what has previously been reported in the literature.

We observe a gap in rotational period over a comparable range to the one presented in Newton et al. (2016) Figure 2. Namely, that M-dwarfs are preferentially observed as either fast or slow rotators, with a seeming lack of stars existing at mid rotational periods. This period gap manifests in the Rossby Number and can be seen in Figure 10.3 as a lack of our targets near to the knee-point in the fit. This period gap likely corresponds to that seen by Browning et al. (2010), who found a paucity of M dwarfs at intermediate activity levels in Ca II H&K and

note the similarity to the Vaughn-Preston gap established in higher mass stars ([Vaughan & Preston, 1980](#)). [Magaudda et al. \(2020\)](#) also identify a double-gap in x-ray activity for stars in the unsaturated regime; it is not clear that the gap we see is related. As a consequence of this period gap, there exists a degeneracy in our data between moving the knee-point and allowing the activity level to vary in the saturated regime. In the following, we adopt the model of a fully saturated regime.

We wish to compare our best fit parameters to those derived in [Astudillo-Defru et al. \(2017\)](#); however, the authors of that paper do not fit the knee-point of the rotation-activity relation. They select the canonical value for the rotational period separating the saturated regime from the unsaturated regime ( $P_{rot,s} = 10$  days) and use a fixed convective overturn timescale ( $\tau_c = 70$  days). To make our comparison more meaningful we use the  $P_{rot}$  and  $V - K$  colors presented in [Astudillo-Defru et al. \(2017\)](#) to re-derive  $Ro$  values using  $\tau_c$  ([Wright et al., 2018](#)). Doing this for all targets presented in [Astudillo-Defru et al. \(2017\)](#) Table 3 and fitting the same piecewise power law as before, we find best fit parameters of  $Ro_s = 0.17 \pm 0.04$ ,  $\log(R_s) = -4.140 \pm 0.067$ , and  $k = -1.43 \pm 0.21$ . Compared to the best fit parameters for our data,  $Ro_s$  and the unsaturated regime's index,  $k$ , are consistent to within one sigma, while the saturated value,  $R_s$ , differs.

The mass ranges of our respective samples explain the differences in saturation values between our work and that of [Astudillo-Defru et al. \(2017\)](#). Our work focuses on mid-to-late M-dwarfs and includes no stars above a mass of  $0.5 M_\odot$  (Figure 10.5). The strength of Ca II H&K emission is known to decrease as stellar mass decreases ([Schrijver & Rutten, 1987](#); [Rauscher & Marcy, 2006](#); [Houdebine et al., 2017](#)). As [Rauscher & Marcy \(2006\)](#) note, this is the opposite as the trend seen in H-alpha; the latter primarily reflects the increasing length of time that lower M dwarfs remain active and rapidly rotating ([West et al., 2015](#); [Newton et al., 2016](#)).

A mass dependence can be seen in Figure 10 in [Astudillo-Defru et al. \(2017\)](#), consistent with expectations from the literature. If we clip the data

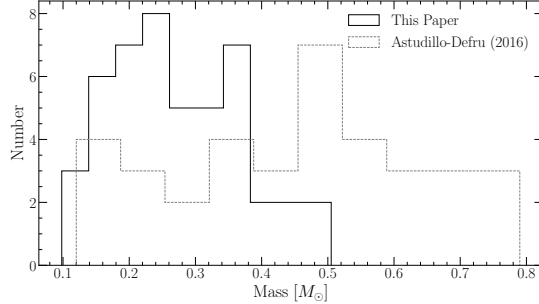


Figure 10.5: Distribution of masses between our sample and the sample presented in [Astudillo-Defru et al. \(2017\)](#). Note how the two studies have approximately the same sample sizes; however, our sample is more tightly concentrated at lower masses \later spectral classes.

from [Astudillo-Defru et al. \(2017\)](#) Table 3 to the same mass range as our data-set ( $M_* < 0.5M_\odot$ ) and fit the same function as above, we find that all best fit parameters are consistent to within one sigma between the two data-sets.

We also compare our best fit  $Ro_s$  to both those derived in [Newton et al. \(2017\)](#) using  $H_\alpha$  as an activity measure and those derived in ([Wright et al., 2018](#); [Magaudda et al., 2020](#)) using  $L_X/L_{bol}$  as an activity measure. Works using  $L_X/L_{bol}$  identify a similar, yet not consistent to within one sigma result for  $Ro_s$ ; while, the value of  $k$  we find here is consistent between all four works. Therefore, we find similar results not only to other work using the same activity tracer, but also a power-law slope that is consistent with work using different tracers.

## 10.5 Magnetic Activities in M dwarfs Closing Thoughts

In this work we have approximately doubled the number of M-dwarfs with both empirically measured  $R'_{HK}$  with  $M_* < 0.5M_\odot$ . This has enabled us to more precisely constrain the rotation-activity relation. This relationship is consistent with other measurements using  $R'_{HK}$ , and  $L_X/L_{bol}$ ; our data does not require a slope in the saturated regime. Finally, we identify a mass dependence in the activity level of the saturated regime, consistent with trends seen in more massive stars in previous works.

2MASS ID	Mass $M_{\odot}$	$Ro$	$\log(R'_{HK})$	$\log(R'_{HK})_{err}$	$V_{mag}$ mag	$V - K$ mag	prot d	$r_{prot}$	Estimate
06000351+0242236	0.24	0.020	-4.5475	0.0021	11.31	5.268	1.809	2016ApJ...821...93N	False
02125458+0000167	0.27	0.048	-4.6345	0.0014	13.58	5.412	4.732	2016ApJ...821...93N	False
01124752+0154395	0.28	0.026	-4.4729	0.0017	14.009	5.240	2.346	2016ApJ...821...93N	False
10252645+0512391	0.11	0.000	-4.9707	0.0380	18.11	7.322	0.102	2016ApJ...821...93N	False
05015746-0656459	0.17	0.873	-5.0049	0.0028	12.2	5.464	88.500	2012AcA....62..67K	False
06022261-2019447	0.23	1.307	-5.6980	0.0192	13.26	4.886	95.000	This Work	False
06105288-4324178	0.30	0.705	-5.2507	0.0139	12.28	4.968	53.736	2018AJ....156..217N	False
09442373-7358382	0.24	0.542	-5.6026	0.0147	15.17	5.795	66.447	2018AJ....156..217N	False
14211512-0107199	0.24	1.160	-5.5846	0.0125	13.12	5.027	91.426	2018AJ....156..217N	False
14294291-6240465	0.12	0.394	-5.0053	0.0014	11.13	6.746	83.500	1998AJ....116..429B	False
16352464-2718533	0.23	1.423	-5.5959	0.0108	14.18	5.182	122.656	2018AJ....156..217N	False
16570570-0420559	0.24	0.014	-4.3071	0.0014	12.25	5.130	1.212	2012AcA....62..67K	False
02004725-1021209	0.34	0.188	-4.7907	0.0026	14.118	5.026	14.793	2018AJ....156..217N	False
18494929-2350101	0.18	0.034	-4.5243	0.0015	10.5	5.130	2.869	2007AcA....57..149K	False
20035892-0807472	0.33	0.946	-5.6530	0.0077	13.54	5.254	84.991	2018AJ....156..217N	False
21390081-2409280	0.21	1.152	-6.1949	0.0190	13.45	5.091	94.254	2018AJ....156..217N	False
23071524-2307533	0.30	0.720	-5.2780	0.0077	13.587	4.849	51.204	2018AJ....156..217N	False
00094508-4201396	0.30	0.009	-4.3392	0.0018	13.62	5.397	0.859	2018AJ....156..217N	False
00310412-7201061	0.31	0.906	-5.3879	0.0074	13.69	5.245	80.969	2018AJ....156..217N	False
01040695-6522272	0.17	0.006	-4.4889	0.0024	13.98	5.448	0.624	2018AJ....156..217N	False
02014384-1017295	0.19	0.034	-4.5400	0.0022	14.473	5.284	3.152	2018AJ....156..217N	False
03100305-2341308	0.40	0.028	-4.2336	0.0017	13.502	4.935	2.083	2018AJ....156..217N	False
03205178-6351524	0.33	1.029	-5.6288	0.0096	13.433	5.238	91.622	2018AJ....156..217N	False
07401183-4257406	0.15	0.002	-4.3365	0.0022	13.81	6.042	0.307	2018AJ....156..217N	False
08184619-4806172	0.37	0.021	-4.2834	0.0025	14.37	5.019	1.653	2018AJ....156..217N	False
08443891-4805218	0.20	1.348	-5.6682	0.0067	13.932	5.370	129.513	2018AJ....156..217N	False
09342791-2643267	0.19	0.007	-4.3415	0.0025	13.992	5.373	0.694	2018AJ....156..217N	False
09524176-1536137	0.26	1.342	-5.6319	0.0110	13.43	4.923	99.662	2018AJ....156..217N	False
11075025-3421003	0.25	0.068	-4.2250	0.0032	15.04	5.633	7.611	2018AJ....156..217N	False
11575352-2349007	0.39	0.031	-4.2952	0.0026	14.77	5.415	3.067	2018AJ....156..217N	False
12102834-1310234	0.36	0.435	-4.6892	0.0029	13.83	5.418	42.985	2018AJ....156..217N	False
12440075-1110302	0.18	0.020	-4.4053	0.0033	14.22	5.546	2.099	2018AJ....156..217N	False
13442092-2618350	0.35	2.032	-5.9634	0.0253	13.253	4.968	154.885	2018AJ....156..217N	False
14253413-1148515	0.51	0.301	-4.7641	0.0030	13.512	5.121	25.012	2018AJ....156..217N	False
14340491-1824106	0.38	0.271	-4.6093	0.0038	14.346	5.638	30.396	2018AJ....156..217N	False
15154371-0725208	0.38	0.050	-4.6214	0.0023	12.93	5.224	4.379	2018AJ....156..217N	False
15290145-0612461	0.46	0.095	-4.2015	0.0017	14.011	5.230	8.434	2018AJ....156..217N	False
16204186-2005139	0.45	0.031	-4.3900	0.0035	13.68	5.261	2.814	2018AJ....156..217N	False
16475517-6509116	0.17	0.889	-4.8744	0.0045	13.98	5.101	73.142	2018AJ....156..217N	False
20091824-0113377	0.15	0.010	-4.3772	0.0023	14.47	5.958	1.374	2018AJ....156..217N	False
20273733-5452592	0.35	1.520	-5.9982	0.0181	13.18	5.259	136.924	2018AJ....156..217N	False
20444800-1453208	0.49	0.073	-4.4912	0.0023	14.445	5.305	6.715	2018AJ....156..217N	False
15404341-5101357	0.10	0.318	-5.0062	0.0081	15.26	7.317	93.702	2018AJ....156..217N	False
22480446-2422075	0.20	0.005	-4.4123	0.0016	12.59	5.384	0.466	2013AJ....146..154M	False
06393742-2101333	0.26	0.952	-5.2524	0.0069	12.77	5.120	79.152	2018AJ....156..217N	False
04130560+1514520	0.30	0.019	-4.4775	0.0088	15.881	5.437	1.881	2016ApJ...818..46M	False
02411510-0432177	0.20	0.004	-4.4272	0.0016	13.79	5.544	0.400	2020ApJ...905..107M	False
11381671-7721484	0.12	0.958	-5.5015	0.0369	14.78	6.259	153.506	This Work	True
12384914-3822527	0.15	2.527	-6.0690	0.0156	12.75	5.364	241.913	This Work	True
13464102-5830117	0.48	1.340	-5.6977	0.0146			65.017	This Work	True
15165576-0037116	0.31	0.157	-4.0704	0.0024	14.469	5.364	15.028	This Work	True
19204795-4533283	0.18	1.706	-5.8392	0.0091	12.25	5.405	167.225	This Work	True
21362532-4401005	0.20	1.886	-5.8978	0.0168	14.14	5.610	207.983	This Work	True

Table 10.1: Calculated Rossby Numbers and  $R'_{HK}$  values. All circular data points in Figures 10.2 & 10.3 are present in this table. Masses are taken from the MEarth database. A machine readable version of this table is available

## Chapter 11

# The Red Giant Branch Bump

The red giant branch bump (RGBB) is a feature experienced by many stellar evolutionary tracks as they ascend the RGB. During this period, as the core of the star is contracting and heating the surrounding material shell burning begins. Regions of the star which were previously too cool to fuse hydrogen (and so therefore still have hydrogen fuel despite core depletion) begin to fuse. At the same time, because of the increase energy output from the heating core and shell burning the balance between the adiabatic and radiative temperature gradients near the convective envelope of the star begins to flip. This results in the convective envelope pushing further into the star. As the convective envelope reaches further into the star hydrogen from the star's outer layers may be efficiently mixed deeper. The convective envelope only ever manages to reach part way down a star's radius during this phase of evolution; however, due to the efficient mixing, by the time it starts to recede to the surface there is a radial discontinuity in the hydrogen concentration within the star. If shell burning reaches this far out then the normal course of RGB ascent will be interrupted by an anomalously large amount of fuel. The star will remain burning that shell for longer than might otherwise be predicted leading to a "bump" in the luminosity function. This is known as the Red Giant Branch Bump.

The RGBB provides yet another view into the interior physics of a star and may allow for calibration and testing of stellar models against observations. Previous work by [Joyce and Chaboyer](#) has found that current generation 1D stellar models, such as

DSEP, may underestimate the bump luminosity for metal poor stars but that they generally models the bump well for more metal rich stars.

In this chapter we will provide two breif views into the RGBB. First, we will look at how different self consistent models of multiple populations in NGC 2808 (the same models dissiscused in Chapter [CHAPTER](#)) effect the RGBB location. Second, we will investigate how the updated low and high temperature opacities which we have incorperated into DSEP effect the RGBB location.

## 11.1 The Red Giant Branch Bunch in NGC 2808

NGC 2808 is made up of of anywhere from 2 - 5 seperate stellar populations. In Chapter [CHAPTER](#) we dissiscused modeling efforts of the primordial and the most enriched of these populations. Here we attempt to identifiy the RGBB location in both populations and compare that to observations of the RGBB luminosity.

Identification of the RGBB may be preformed with either isochrones or stellar evolutionary tracks. For the same reasons laied out in [Joyce and Chaboyer 2015](#) we use evolutionary tracks in place of isochrones. This is primarily due to the limited sampling of equivilent evolutionary points near the bump which can result in the bump be interpolated over.

We select two evolutionary tracks from the Population A ( $Y \sim 0.14$ ) and Population E ( $Y \sim 0.36$ ) model sets each of a mass so that they reach the red giant branch within 100 Myr of each other. The population A model is of mass [MASS](#) while the population E model is of mass [MASS](#). Identification of the RGBB in the tracks is then straigtforward. First we preform bolometric corrections to take the tracks into WFC3/ACS filters with the same distance modulus and extiction as we fit in chapter [CHAPTER](#), then we identify the maximum of the derivitve of F814W magnitude vs. age. This metric prooves to reliably extracy the center of the RGBB. We identify the bump in population A at a mag of [16.5](#) while we are unable to identify the gap in population E.

In order to verify this is a attribute of the population and not the particular model we selected we preform stellar population synthethis using the best fit isochrones from

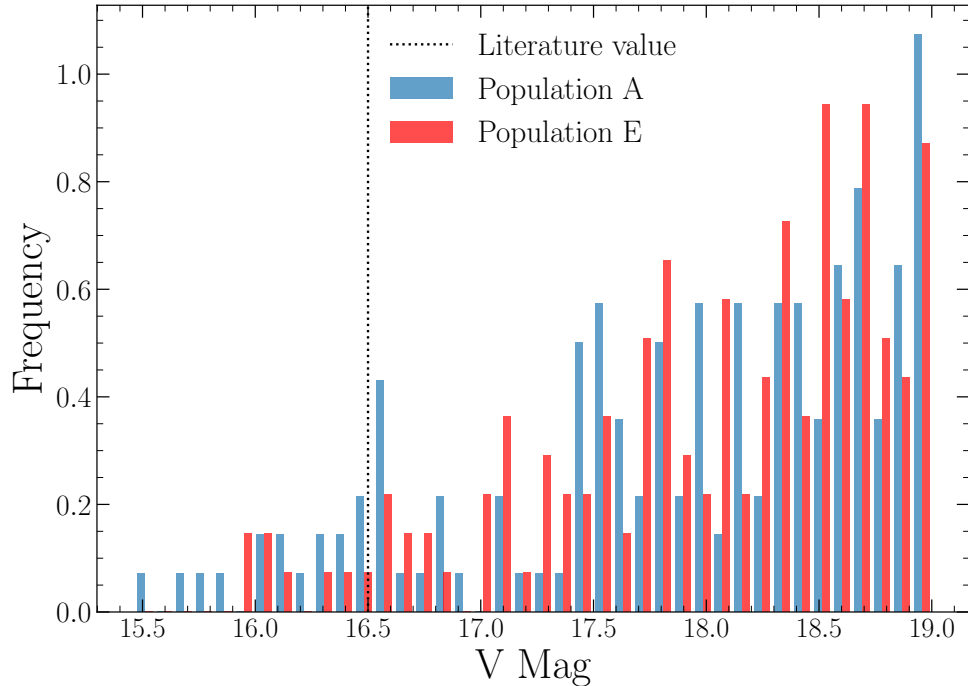


Figure 11.1: Luminosity function for a population A and E model. Note how there is a bump at approximately  $M_V = 16.5$  for population A but not for E. The dashed line represents the literature value for the observed RGBB in NGC 2808.

Chapter [CHAPTER](#). This is done using the population synthethis module in [Fidanka](#). Further, HUGS artificial star tests are used in order to inject proper uncertainties and to model completeness. Figure 11.1 shows both the synthetic population (left) and the luminosity function of that population (right). Note that the bump at [16.5](#) is in agreement with literature values for the magnitude of the RGBB in NGC 2808. However, once again we do not see a bump in the synthetic population E data. The pertinatnt question then becomes why do we not see a RGBB in population E when compared to population A.

### 11.1.1 Population E and the Case of the Missing Bump

It is well estabilshed that stars with lower metallicities will have a less pronounced bump [\[CITATION HERE\]](#). Population E in fact is dramatically more depleted in general metallicity than population A ( $[Fe/H] = -1.34$  and  $[Fe/H] = -0.94$  respectivley). Lower metallicities decrease the opacity of a star and therefore make the coupling between the radiation field and the fluid field weaker. This results in less efficient

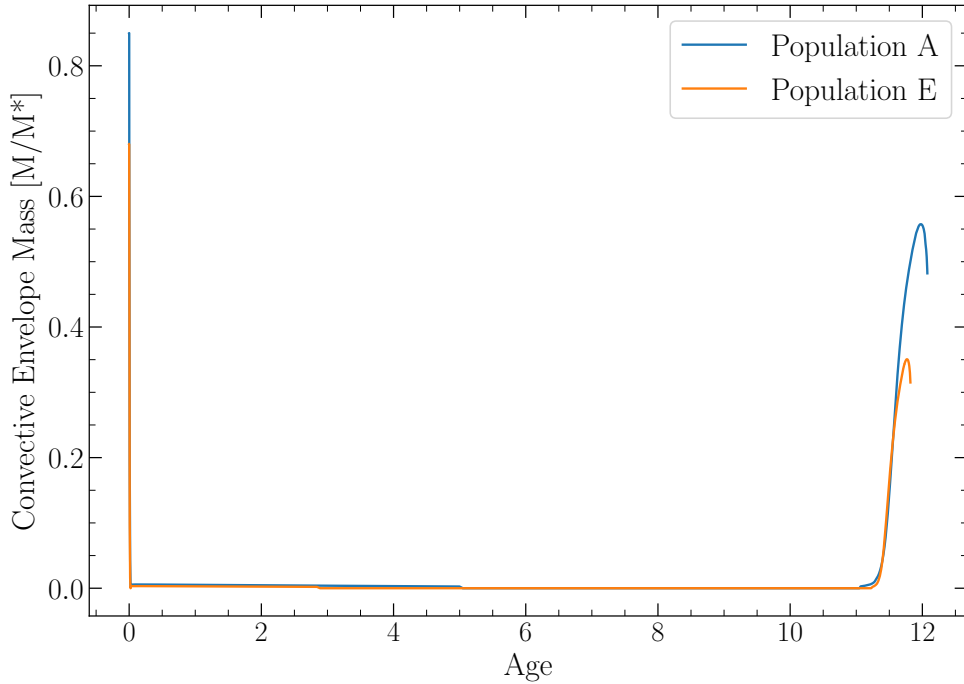


Figure 11.2: Fractional mass of the convective envelope of a population A and E model vs. model age. Note how the population A model's convective envelope reaches approximately 60 percent of the star by mass while the population E convective envelope only reaches 40 percent of the star by mass.

thermal transfer into the fluid of the star. This results in a more shallow outer convective zone (Figure 11.2) which may not be able mix new hydrogen fuel deep enough to induce the RGBB.

## 11.2 Effects of Opacities on the Red Giant Branch Bump

## 11.3 Going forward

## **Part IV**

# **Conclusions**



# Bibliography

- Alcaino, G. 1975, A&AS, 21, 15
- Amard, L., Palacios, A., Charbonnel, C., et al. 2019, A&A, 631, A77
- Angus, R. 2021, Zenodo, doi:10.5281/zenodo.4613887
- Angus, R., Morton, T., Aigrain, S., Foreman-Mackey, D., & Rajpaul, V. 2018, Monthly Notices of the Royal Astronomical Society, 474, 2094
- Astropy Collaboration, Price-Whelan, A. M., Sipőcz, B. M., et al. 2018, AJ, 156, 123
- Astudillo-Defru, N., Delfosse, X., Bonfils, X., et al. 2017, A&A, 600, A13
- Bahcall, J. N., Pinsonneault, M. H., & Basu, S. 2001, ApJ, 555, 990
- Bahcall, J. N., Serenelli, A. M., & Basu, S. 2005, ApJL, 621, L85
- Baraffe, I., & Chabrier, G. 2018, A&A, 619, A177
- Baraffe, I., Chabrier, G., Allard, F., & Hauschildt, P. H. 1997, A&A, 327, 1054
- Barber, C. B., Dobkin, D. P., & Huhdanpaa, H. 1996, ACM Transactions on Mathematical Software (TOMS), 22, 469
- Barentsen, G., Hedges, C., Vinícius, Z., et al. 2020, KeplerGO/Lightkurve: Lightkurve v1.11.0, Zenodo, , , doi:10.5281/zenodo.3836658
- Barnes, J., Cameron, A. C., Donati, J.-F., et al. 2005, Monthly Notices of the Royal Astronomical Society: Letters, 357, L1
- Barnes, J., James, D., & Cameron, A. C. 2004, Monthly Notices of the Royal Astronomical Society, 352, 589

- Baroch, D., Morales, J. C., Ribas, I., et al. 2020, A&A, 641, A69
- Bastian, N., & Lardo, C. 2015, MNRAS, 453, 357
- Bastian, N., & Lardo, C. 2018, Annual Review of Astronomy and Astrophysics, 56, 83
- Baumgardt, H., & Makino, J. 2003, MNRAS, 340, 227
- Bekki, K., & Chiba, M. 2002, The Astrophysical Journal, 566, 245. <https://dx.doi.org/10.1086/337984>
- Bernstein, R., Shectman, S. A., Gunnels, S. M., Mochnacki, S., & Athey, A. E. 2003, in Society of Photo-Optical Instrumentation Engineers (SPIE) Conference Series, Vol. 4841, Proc. SPIE, ed. M. Iye & A. F. M. Moorwood, 1694–1704
- Berta, Z. K., Irwin, J., Charbonneau, D., Burke, C. J., & Falco, E. E. 2012, AJ, 144, 145
- Bjork, S. R., & Chaboyer, B. 2006, ApJ, 641, 1102
- Boudreaux, E. M., Newton, E. R., Mondrik, N., Charbonneau, D., & Irwin, J. 2022, ApJ, 929, 80
- Boylan-Kolchin, M. 2018, MNRAS, 1423
- Brodie, J. P., & Strader, J. 2006, Annu. Rev. Astron. Astrophys., 44, 193
- Brown, J. H., Burkert, A., & Truran, J. W. 1991, ApJ, 376, 115  
—. 1995, ApJ, 440, 666
- Browning, M. K., Basri, G., Marcy, G. W., West, A. A., & Zhang, J. 2010, AJ, 139, 504
- Cameron, R. H., Dikpati, M., & Brandenburg, A. 2017, Space Science Reviews, 210, 367. <https://doi.org/10.1007/s11214-015-0230-3>
- Carretta, E. 2013, A&A, 557, A128

- Carretta, E., Bragaglia, A., Gratton, R. G., et al. 2010, *Astronomy & Astrophysics*, 516, A55
- Catalano, S., & Marilli, E. 1983, *A&A*, 121, 190
- Chaboyer, B., Fenton, W. H., Nelan, J. E., Patnaude, D. J., & Simon, F. E. 2001, *ApJ*, 562, 521
- Chabrier, G., & Baraffe, I. 1997, *A&A*, 327, 1039
- Charbonneau, P. 2014, *ARA&A*, 52, 251
- Choi, J., Dotter, A., Conroy, C., et al. 2016, *ApJ*, 823, 102
- Colgan, J., Kilcrease, D. P., Magee, N. H., et al. 2016, in *APS Meeting Abstracts*, Vol. 2016, APS Division of Atomic, Molecular and Optical Physics Meeting Abstracts, D1.008
- Cowling, T. G. 1966, *QJRAS*, 7, 121
- Creevey, O. L., Sordo, R., Pailler, F., et al. 2022, arXiv e-prints, arXiv:2206.05864
- de Mink, S. E., Pols, O. R., Langer, N., & Izzard, R. G. 2009, *A&A*, 507, L1
- Decressin, T., Meynet, G., Charbonnel, C., Prantzos, N., & Ekström, S. 2007, *A&A*, 464, 1029
- Delfosse, X., Forveille, T., Perrier, C., & Mayor, M. 1998, *A&A*, 331, 581
- Denissenkov, P. A., & Hartwick, F. D. A. 2014, *MNRAS*, 437, L21
- D'Ercole, A., D'Antona, F., Ventura, P., Vesperini, E., & McMillan, S. L. W. 2010, *MNRAS*, 407, 854
- D'Ercole, A., Vesperini, E., D'Antona, F., McMillan, S. L. W., & Recchi, S. 2008, *MNRAS*, 391, 825
- DIERCKX, P. 1981, *IMA Journal of Numerical Analysis*, 1, 267. <https://doi.org/10.1093/imanum/1.3.267>
- Dikpati, M., & Charbonneau, P. 1999, *ApJ*, 518, 508

- Dotter, A. 2016, ApJS, 222, 8
- Dotter, A., Chaboyer, B., Jevremović, D., et al. 2008, The Astrophysical Journal Supplement Series, 178, 89
- Dotter, A., Ferguson, J. W., Conroy, C., et al. 2015, MNRAS, 446, 1641
- Earl, N., Tollerud, E., Jones, C., et al. 2021, astropy/specutils: v1.3, vv1.3, Zenodo, doi:10.5281/zenodo.4987675. <https://doi.org/10.5281/zenodo.4987675>
- Emden, R. 1907, Gaskugeln
- Feiden, G. A., Skidmore, K., & Jao, W.-C. 2021, ApJ, 907, 53
- Feinstein, A., Montet, B., & Ansdell, M. 2020a, J. Open Source Softw., 5, 2347
- Feinstein, A. D., Montet, B. T., Ansdell, M., et al. 2020b, Astron. J., 160, 219
- Ferguson, J. W., Alexander, D. R., Allard, F., et al. 2005, ApJ, 623, 585
- Ferguson, T. S. 1973, The annals of statistics, 209
- Fontes, C. J., Zhang, H. L., Abdallah, J., J., et al. 2015, Journal of Physics B Atomic Molecular Physics, 48, 144014
- Gaia Collaboration, Smart, R. L., Sarro, L. M., et al. 2021, A&A, 649, A6
- García Soto, A., Newton, E. R., Douglas, S. T., Burrows, A., & Kesseli, A. Y. 2023, AJ, 165, 192
- Gastine, T., Yadav, R. K., Morin, J., Reiners, A., & Wicht, J. 2014, MNRAS, 438, L76
- Gratton, R., Sneden, C., & Carretta, E. 2004, ARA&A, 42, 385
- Gratton, R. G., Carretta, E., & Bragaglia, A. 2012, Astronomy and Astrophysics Reviews, 20, 50
- Grevesse, N., Asplund, M., & Sauval, A. J. 2007, SSRv, 130, 105
- Grevesse, N., & Sauval, A. J. 1998, SSRv, 85, 161

- Gustafsson, B., Edvardsson, B., Eriksson, K., et al. 2008, A&A, 486, 951
- Hakel, P., Sherrill, M. E., Mazevert, S., et al. 2006, JQSRT, 99, 265
- Hall, J. C., Lockwood, G. W., & Skiff, B. A. 2007, The Astronomical Journal, 133, 862. <https://doi.org/10.1086%2F510356>
- Hawley, S. L., Gizis, J. E., & Reid, I. N. 1996, AJ, 112, 2799
- Hawley, S. L., & Pettersen, B. R. 1991, ApJ, 378, 725
- Henyey, L. G., Forbes, J. E., & Gould, N. L. 1964, ApJ, 139, 306
- Houdebine, E. R., Mullan, D. J., Bercu, B., Paletou, F., & Gebran, M. 2017, ApJ, 837, 96
- Hudson, M. J., & Robison, B. 2018, Monthly Notices of the Royal Astronomical Society, 477, 3869
- Husser, T. O., Wende-von Berg, S., Dreizler, S., et al. 2013, A&A, 553, A6
- Iglesias, C. A., & Rogers, F. J. 1996, ApJ, 464, 943
- Irwin, J., Berta, Z. K., Burke, C. J., et al. 2011, ApJ, 727, 56
- Jao, W.-C., & Feiden, G. A. 2020, AJ, 160, 102
- . 2021, Research Notes of the American Astronomical Society, 5, 124
- Jao, W.-C., Henry, T. J., Gies, D. R., & Hambly, N. C. 2018, ApJL, 861, L11
- Jao, W.-C., Henry, T. J., White, R. J., et al. 2023, AJ, 166, 63
- Jermyn, A. S., Bauer, E. B., Schwab, J., et al. 2022, arXiv e-prints, arXiv:2208.03651
- Jordán, A., Côté, P., West, M. J., & Marzke, R. O. 2002, ApJL, 576, L113
- Joyce, M., & Chaboyer, B. 2018, ApJ, 864, 99
- Kelson, D. D. 2003, PASP, 115, 688
- Kelson, D. D., Illingworth, G. D., van Dokkum, P. G., & Franx, M. 2000, ApJ, 531, 159

- Kesseli, A. Y., Muirhead, P. S., Mann, A. W., & Mace, G. 2018, AJ, 155, 225
- Kostogryz, N., Shapiro, A. I., Witzke, V., et al. 2023, Research Notes of the AAS, 7, 39. <https://dx.doi.org/10.3847/2515-5172/acc180>
- Kovetz, A., Yaron, O., & Prialnik, D. 2009, MNRAS, 395, 1857
- Kravtsov, A. V., & Gnedin, O. Y. 2005, The Astrophysical Journal, 623, 650
- Kurucz, R.-L. 1993, Kurucz CD-Rom, 13
- Latour, M., Husser, T. O., Giesers, B., et al. 2019, A&A, 631, A14
- Lehtinen, J. J., Käpylä, M. J., Olspert, N., & Spada, F. 2020, arXiv e-prints, arXiv:2007.00040
- Lightkurve Collaboration, Cardoso, J. V. d. M., Hedges, C., et al. 2018, Astrophysics Source Code Library, ascl:1812.013
- Lovis, C., Ségransan, D., Mayor, M., et al. 2011, Astronomy & Astrophysics, 528, A112
- MacDonald, J., & Gizis, J. 2018, MNRAS, 480, 1711
- Magaudda, E., Stelzer, B., Covey, K. R., et al. 2020, A&A, 638, A20
- Magee, N. H., Abdallah, J., Colgan, J., et al. 2004, in American Institute of Physics Conference Series, Vol. 730, Atomic Processes in Plasmas: 14th APS Topical Conference on Atomic Processes in Plasmas, ed. J. S. Cohen, D. P. Kilcrease, & S. Mazzavent, 168–179
- Mamajek, E. E., & Hillenbrand, L. A. 2008, ApJ, 687, 1264
- Mann, A. W., Gaidos, E., Mace, G. N., et al. 2016, ApJ, 818, 46
- Mansfield, S., & Kroupa, P. 2021, A&A, 650, A184
- Marigo, P., & Aringer, B. 2009, A&A, 508, 1539
- Marigo, P., Aringer, B., Girardi, L., & Bressan, A. 2022, ApJ, 940, 129

- Marino, A. F., Milone, A. P., Karakas, A. I., et al. 2015, Monthly Notices of the Royal Astronomical Society, 450, 815. <https://doi.org/10.1093/mnras/stv420>
- Medina, A. A., Winters, J. G., Irwin, J. M., & Charbonneau, D. 2020, ApJ, 905, 107
- Middelkoop, F. 1982, A&A, 107, 31
- Milone, A. P., Piotto, G., Bedin, L. R., et al. 2012, ApJ, 744, 58
- Milone, A. P., Marino, A. F., Piotto, G., et al. 2015a, ApJ, 808, 51
- . 2015b, MNRAS, 447, 927
- Milone, A. P., Piotto, G., Renzini, A., et al. 2017, MNRAS, 464, 3636
- Milone, A. P., Marino, A. F., Renzini, A., et al. 2018, MNRAS, 481, 5098
- Newton, E. R., Irwin, J., Charbonneau, D., et al. 2017, The Astrophysical Journal, 834, 85
- Newton, E. R., Irwin, J., Charbonneau, D., et al. 2016, ApJ, 821, 93
- Newton, E. R., Mondrik, N., Irwin, J., Winters, J. G., & Charbonneau, D. 2018, AJ, 156, 217
- Noyes, R. W., Hartmann, L. W., Baliunas, S. L., Duncan, D. K., & Vaughan, A. H. 1984, ApJ, 279, 763
- Núñez, A., Agüeros, M. A., Covey, K. R., et al. 2015, ApJ, 809, 161
- Nutzman, P., & Charbonneau, D. 2008, PASP, 120, 317
- Owen, J. E., & Mohanty, S. 2016, MNRAS, 459, 4088
- Pallavicini, R., Golub, L., Rosner, R., et al. 1981, ApJ, 248, 279
- Parker, E. N. 1955, ApJ, 122, 293
- . 1975, ApJ, 198, 205
- Paxton, B., Bildsten, L., Dotter, A., et al. 2011, The Astrophysical Journal Supplement Series, 192, 3

- Pedregosa, F., Varoquaux, G., Gramfort, A., et al. 2011, Journal of Machine Learning Research, 12, 2825
- Peebles, P. J. E., & Dicke, R. H. 1968, ApJ, 154, 891
- Peng, E. W., Ferguson, H. C., Goudrooij, P., et al. 2011, The Astrophysical Journal, 730, 23
- Perdelwitz, V., Mittag, M., Tal-Or, L., et al. 2021, A&A, 652, A116
- Piotto, G., Bedin, L. R., Anderson, J., et al. 2007, The Astrophysical Journal Letters, 661, L53
- Piotto, G., Milone, A. P., Bedin, L. R., et al. 2015, AJ, 149, 91
- Pizzolato, N., Maggio, A., Micela, G., et al. 2000, in Astronomical Society of the Pacific Conference Series, Vol. 198, Stellar Clusters and Associations: Convection, Rotation, and Dynamos, ed. R. Pallavicini, G. Micela, & S. Sciortino, 71
- Plez, B. 2008, Physica Scripta Volume T, 133, 014003
- Prantzos, N., Charbonnel, C., & Iliadis, C. 2007, A&A, 470, 179
- Rauscher, E., & Marcy, G. W. 2006, PASP, 118, 617
- Reiners, A., Schüssler, M., & Passegger, V. M. 2014, ApJ, 794, 144
- Renzini, A. 2008, Monthly Notices of the Royal Astronomical Society, 391, 354.  
<https://doi.org/10.1111/j.1365-2966.2008.13892.x>
- Richer, H. B., Fahlman, G. G., Buonanno, R., et al. 1991, ApJ, 381, 147
- Robertson, P., Mahadevan, S., Endl, M., & Roy, A. 2014, Science, 345, 440
- Rodríguez-López, C. 2019, Frontiers in Astronomy and Space Sciences, 6, 76
- Rousseeuw, P. J. 1987, Journal of Computational and Applied Mathematics, 20, 53.  
<https://www.sciencedirect.com/science/article/pii/0377042787901257>
- Rutten, R. G. M. 1984, A&A, 130, 353

- Salaris, M., & Cassisi, S. 2005, Evolution of stars and stellar populations (John Wiley & Sons)
- Salvatier, J., Wiecki, T. V., & Fonnesbeck, C. 2016, PeerJ Computer Science, 2, e55.  
<https://doi.org/10.7717/peerj-cs.55>
- Sandage, A. R. 1953, AJ, 58, 61
- Sbordone, L., Salaris, M., Weiss, A., & Cassisi, S. 2011, Astronomy & Astrophysics, 534, A9
- Schmidt, S. J., Prieto, J. L., Stanek, K. Z., et al. 2014, ApJL, 781, L24
- Schrijver, C. J., & Rutten, R. G. M. 1987, A&A, 177, 143
- Schröder, C., Reiners, A., & Schmitt, J. H. M. M. 2009, A&A, 493, 1099
- Seaton, M. J., Yan, Y., Mihalas, D., & Pradhan, A. K. 1994, MNRAS, 266, 805
- Shields, A. L., Ballard, S., & Johnson, J. A. 2016, PhR, 663, 1
- Shulyak, D., Reiners, A., Nagel, E., et al. 2019, A&A, 626, A86
- Skrutskie, M. F., Cutri, R. M., Stiening, R., et al. 2006, AJ, 131, 1163
- Skumanich, A. 1972, ApJ, 171, 565
- Smith, G. H. 1987, Publications of the Astronomical Society of the Pacific, 99, 67.  
<https://dx.doi.org/10.1086/131958>
- Sneden, C., Kraft, R. P., Prosser, C. F., & Langer, G. 1992, The Astronomical Journal, 104, 2121
- Sollima, A. 2019, Monthly Notices of the Royal Astronomical Society, 489, 2377.  
<https://doi.org/10.1093/mnras/stz2093>
- Suárez Mascareño, A., Rebolo, R., & González Hernández, J. I. 2016, A&A, 595, A12
- Suárez Mascareño, A., Rebolo, R., González Hernández, J. I., & Esposito, M. 2015, MNRAS, 452, 2745

- Suntzeff, N. B., & Kraft, R. P. 1996, AJ, 111, 1913
- Thompson, M. J., Toomre, J., Anderson, E. R., et al. 1996, Science, 272, 1300
- Tomczyk, S., Schou, J., & Thompson, M. J. 1996, in American Astronomical Society Meeting Abstracts, Vol. 188, American Astronomical Society Meeting Abstracts #188, 69.03
- Torres, C. A. O., Quast, G. R., da Silva, L., et al. 2006, A&A, 460, 695
- Trampedach, R., Stein, R. F., Christensen-Dalsgaard, J., Nordlund, Å., & Asplund, M. 2014, MNRAS, 445, 4366
- Valle, G., Dell’Omodarme, M., & Tognelli, E. 2022, A&A, 658, A141
- van den Bergh, S. 2010, The Astronomical Journal, 140, 1043. <https://dx.doi.org/10.1088/0004-6256/140/4/1043>
- van Saders, J. L., & Pinsonneault, M. H. 2012, ApJ, 751, 98
- Vanderburg, A., Plavchan, P., Johnson, J. A., et al. 2016, Monthly Notices of the Royal Astronomical Society, 459, 3565
- Vaughan, A. H., Baliunas, S. L., Middelkoop, F., et al. 1981, ApJ, 250, 276
- Vaughan, A. H., & Preston, G. W. 1980, Publications of the Astronomical Society of the Pacific, 92, 385
- Ventura, P., & D’Antona, F. 2009, A&A, 499, 835
- Ventura, P., D’Antona, F., Mazzitelli, I., & Gratton, R. 2001, ApJL, 550, L65
- Vilhu, O. 1984, A&A, 133, 117
- West, A. A., Weisenburger, K. L., Irwin, J., et al. 2015, ApJ, 812, 3
- Wilson, O. C. 1963, ApJ, 138, 832
- . 1968, ApJ, 153, 221
- Winters, J. G., Henry, T. J., Jao, W.-C., et al. 2019, AJ, 157, 216

Wright, N. J., Drake, J. J., Mamajek, E. E., & Henry, G. W. 2011, *The Astrophysical Journal*, 743, 48. <https://doi.org/10.1088%2F0004-637x%2F743%2F1%2F48>

Wright, N. J., Newton, E. R., Williams, P. K. G., Drake, J. J., & Yadav, R. K. 2018, *MNRAS*, 479, 2351